

**DEVELOPMENT OF FLUORESCENCE BASED PROBES FOR
DISEASE IMAGING**

Phumlani Tetyana

(1026137)

**A Thesis submitted to the Faculty of Science, School of Chemistry at
University of the Witwatersrand, in fulfilment of the requirements for the
degree of Doctor of Philosophy**

Supervisors: Prof. Nosipho Moloto (Wits, School of Chemistry)
Dr. Amanda Skepu (Mintek, AMD)
Dr. Poslet Shumbula (Mintek, AMD)

Academic year: 2018

DECLARATION

I declare that this thesis is my own, unaided work. It has been carried out under the supervision of Professor Nosipho Moloto. It is being submitted for the degree of Doctoral of Philosophy in Science at the University of the Witwatersrand, Johannesburg. It has not been submitted before for any degree or examination in any other university.



PHUMLANI TETYANA

On this 13 day of June 2018.

ABSTRACT

Microscopy detection has once been the gold standard in the detection of infectious diseases such as tuberculosis and cancer, and therefore improvements in the detection procedure could further enhance sensitivity and restore its use. Fluorescent probes for microscopy detection have been synthesized using organic dyes which have numerous limitations, such as a narrow absorption spectra and a broad emission spectra to name but a few, that impact negatively on assay sensitivity. Use of semiconducting nanomaterials in the design of fluorescent probes for disease detection eliminates the aforementioned limitations and enhances the sensitivity of detection, and also allows for the detection of multiple disease analytes further improving the scope of detection which eliminates misdiagnosis. Moreover, commercially available nanomaterials are synthesized from toxic elements such as cadmium, lead and mercury; using an organometallic synthesis route which further yields nanomaterials not suitable for bio applications. This study is based on the aqueous synthesis of semiconducting nanomaterials for use as fluorophores in the development of fluorescent probes for imaging of cellular materials.

Copper and Cobalt sulfide nanomaterials were of interest in our study. They were synthesized via an aqueous synthesis method, using four different capping ligands, namely; glutathione, thioglycolic acid, 18-crown-6 and L-carnosine. Reactions were performed at either 50 and 95 °C, using deionized water as a solvent. The optical and structural properties of as-synthesized nanoparticles (NPs) were investigated using UV/Vis absorption spectroscopy (UV-Vis), Photoluminescence spectroscopy (PL), Transmission Electron Microscope (TEM), X-Ray Diffraction (XRD) spectroscopy and Fourier Transform Infrared Spectroscopy (FT-IR). The cytotoxic properties of as-synthesized NPs were investigated using the 3-[4,5-dimethylthiazol-2-yl]-2,5 diphenyl tetrazolium bromide tetrazolium assay (MTS). Fluorescent probes were constructed by conjugating hypoxia inducible factor-1 α (HIF-1 α) and the Phosphohistone H2A.X (Phospho H2A.X) monoclonal antibodies to as-synthesized NPs using carbodiimide chemistry. The fluorescent probes were used to target HIF-1 α and Phospho H2A.X proteins produced in mammalian cells (Human Embryonic Kidney (Hek-293) and HeLa cells) undergoing apoptosis, *in vitro*.

The optical properties of as-synthesized NPs depicted absorption spectra that are blue shifted from their bulk counterparts, signifying the formation of small nanoparticles. This is due to quantum size effects. Copper sulfide nanoparticles depicted emission peaks that are red shifted from their respective absorption spectra while cobalt sulfide nanoparticles revealed red shifted emission spectra. TEM images revealed the formation of various morphologies, including spheres, hexagons and rods, in response to the use of different capping ligands, synthesis temperatures and sulfur sources. The size of nanoparticles was greatly influenced by the reaction temperature, with small nanoparticles formed at 50 °C while bigger particles were formed at 95 °C. The XRD revealed the formation of mixed phases when the temperature of the reaction was set at 50 °C. At 95 °C, single phases were formed and the reactions were seen to be complete as no evidence of non-reacted material was observed. The interaction of the capping ligands with NPs was confirmed via FT-IR, with various capping ligands employing different functional groups to attach to the surface of NPs, which were not affected by reaction temperature or sulfur source employed.

The cytotoxicity of as-synthesized NPs was investigated using an MTS assay. Copper sulfide NPs were seen to be non-toxic at concentrations below 6µg/ml, with a dose dependant decrease in cell viability observed throughout. However, for CuS NPs synthesized at 50 °C using SDEDTC, a decline is observed when the concentration of nanoparticles exceeds 3.125 µg/ml. Co_xS_y NPs were found to be non-toxic to MT-4 cells, with cell viability maintained above 80% even at the highest concentration tested. Fluorescent probes were developed by conjugating antibodies to Cu_xS_y NPs for imaging purposes. A slight shift to higher wavelength was observed in the absorption spectra of Cu_xS_y NPs after the conjugation step, signifying the presence of the antibodies on the surface of nanoparticles. When tested *in vitro* using cells treated with CoCl₂ and doxorubicin, the fluorescent probes were internalised by the cells, but their fluorescence intensity was low when compared to cells treated with non-conjugated nanoparticles. These results demonstrate the feasibility of utilising these nanoparticles in the development of fluorescent probes for biological imaging applications *in vitro*, with further optimisation.

DEDICATION

For:

My Beloved Parents:

Oscar Qamata Tetyana and Lovelyn Yolisa Tetyana

My Fiance:

Zikhona “Ngwanya” Njengele

My Brothers and Sisters:

Nosipho, Thulani, Yanga, Akhona, Dumo, Thandi, Odwa and Aviwe

My Spiritual Parents:

Apostle Dr. A. N. Mabaso and Prophetess C. Mabaso

ACKNOWLEDGEMENTS

This journey could not have been possible without the assistance I have received from different well-wishers and associates. Hence; I would like to express my heartfelt gratitude to my supervisors, Prof. Nosipho Moloto (University of the Witwatersrand), Dr. Amanda Skepu and Dr Poslet Morgan Shumbula (Mintek), for allowing me to undertake this study under your supervision. Your guidance, amicable comments and insight has made this work possible.

To my parents, brothers and sisters and my fiancé, you have been a pillar of strength which sustained me through hard and trying times, thank you for the support you have shown me.

The University of the Witwatersrand for allowing me to utilize their facilities for further characterization of my samples. To Rudo Sithole, Lerato Machogo and Ndivhuwo Shumbula (University of the Witwatersrand), thank you for your patience and help with analysing my samples with FTIR, XRD and PL. You have played a significant role in this work. You had your own projects to focus on, but you also thought of me during my time of need.

The entire CATOMAT group; you have provided me with a family that shaped my work by scrutinizing my presentations without fear. It was never personal, but about bringing the best out of me, and finally that goal was achieved.

To my spiritual parents, Apostle Dr. Absalom. N. Mabaso and his wife, Prophetess Cindy Mabaso, you were a source of blessing and encouragement even when I thought I could not take it anymore. The role you played during the course of my studies kept me on my toes. I am proud to be your spiritual son. I have no shame to let you know that you are the best.

To Mintek and the DST/Mintek NIC, you have supported me financially to see to it that my life improves. I will forever cherish the support and encouragement you made available for me.

To Thapelo Prince Mofokeng and Bonginkosi Sibokoza (Vaal University of Technology), I will never undermine the assistance you provided me with. On a number of times, you frequently allowed me to visit your institution and helped me with Photoluminescence

spectroscopy for my samples analysis. I don't know where I would be without you. You are the best.

Above all, I would like to thank God Almighty for the strength, wisdom, and understanding he granted me during the course of this study, for it is He that gives us the ability to achieve great things.

PUBLICATIONS

P. Tetyana, P. M. Shumbula, N. G. Mphuthi, A. N. Jijana, N. Moloto, A. Skepu and L. S. Vilakazi. Aqueous Synthesis, Characterization and Electrochemical Properties of Copper Sulfide Nanoparticles – manuscript prepared

P. Tetyana, P. M. Shumbula, S. Abrahams, Z. Njengele, N. Moloto and A. Skepu. Toxicity studies of as-synthesized L-carnosine capped copper sulfide nanoparticles – manuscript prepared

PRESENTATIONS

Synthesis and Characterization of Copper Sulfide Quantum Dots. Oral presentation at the DST/Mintek NIC technical meeting, December 2014, Johannesburg, South Africa

Aqueous Synthesis and Characterization of Copper Sulfide Nanoparticles for Detection of Infectious Diseases *In-vitro*. Poster presentation at the 42nd SACI Convention, November 2015, Durban, South Africa

Aqueous Synthesis of Copper Sulfide Quantum Dots for Biological Applications. Oral presentation at the 7th World Nano Conference, June 2016, Cape Town, South Africa

Electrochemical Studies Of Water Soluble Copper Sulfide Nanoparticles. Oral presentation at the MSSA conference, December 2016, Port Elizabeth, South Africa

Copper Sulfide Nanoparticle Synthesis: Effect of Sulfur Source on Nanoparticle Formation. Oral presentation at DST/Mintek NIC technical meeting, July 2017, Johannesburg, South Africa

Synthesis, Characterization and Toxicity Studies of Copper and Cobalt Sulfide Nanoparticles for Use in Imaging Applications. Oral presentation at the CATOMMAT Group, November 2017, Johannesburg, South Africa

Water Soluble Copper Sulfide Nanoparticles for Biological Applications: Synthesis, Characterization and Cytotoxicity Studies. Poster presentation at the DST/Mintek NIC workshop, March 2018, Johannesburg, South Africa

TABLE OF CONTENTS

DECLARATION	i
ABSTRACT.....	ii
DEDICATION.....	iv
ACKNOWLEDGEMENTS.....	v
PUBLICATIONS.....	vii
PRESENTATIONS.....	vii
LIST OF FIGURES	xiv
LIST OF TABLES.....	xxi
LIST OF ABBREVIATIONS.....	xxii
Chapter 1: Introduction	1
1.1 Background and Rationale	1
1.2 Aims and Objectives	3
1.3 Thesis Outline	3
1.4 References	5
Chapter 2: Literature Review.....	7
2.1 Nanotechnology	7
2.2 Quantum dots or Semiconductor nanoparticles	8
2.2.1 Properties of Semiconductor Nanomaterials	10
2.2.2 Methods for Synthesizing Semiconductor Nanoparticles.....	14

2.2.3	Semiconductor Nanoparticle Formation Process.....	17
2.3	Metal Chalcogenides (Copper Sulfide and Cobalt Sulfide).....	21
2.3.1	Copper Sulfide	21
2.3.2	Cobalt Sulfide	22
2.4	Applications of Metal Chalcogenide Nanoparticles.....	23
2.4.1	Biological Assays.....	23
2.5	Solubility of Semiconductor Nanoparticles	25
2.6	Biofunctionalization	26
2.6.1	Covalent Attachment	27
2.6.2	Non-covalent Attachment	28
2.7	Nanoparticle Toxicity.....	29
2.8	Significance of Capping Ligands in Semiconductor Nanoparticle Synthesis.....	31
2.8.1	L-Glutathione.....	31
2.8.2	Thioglycolic Acid	32
2.8.3	18-Crown-6.....	32
2.8.4	L-Carnosine.....	33
2.9	References	35
Chapter 3: Experimental		51
3.1	Synthesis and Characterization of Metal Sulfide Nanoparticles.....	51
3.1.1	Chemicals and Reagents	51
3.1.2	Synthesis of Copper and Cobalt Sulfide Nanoparticles.....	51

3.1.3	Characterization Techniques.....	52
3.2	Cytotoxicity Studies of Copper and Cobalt Sulfide Nanoparticles.....	53
3.2.1	Chemicals and Reagents	53
3.2.2	Cell Maintenance	53
3.2.3	Trypan Blue Exclusion Assay.....	53
3.2.4	Cytotoxicity Assay.....	54
3.3	Nanoparticle Bio-functionalization and Imaging.....	54
3.3.1	Chemicals and Reagents	54
3.3.2	Bio-conjugation or Probe development	55
3.3.3	Cell Imaging using Probes	55
Chapter 4:	Results for Characterization of Copper Sulfide Nanoparticles	58
4.1	Introduction	58
4.2	Results and Discussions	59
4.2.1	Characterization of copper sulfide nanoparticles synthesized using SDEDTC as a sulfur source.....	59
4.2.2	Characterization of copper sulfide nanoparticles synthesized using TAA as a sulfur source.....	70
4.3	Conclusions	79
4.4	References	80
Chapter 5:	Results for Characterization of Cobalt Sulfide Nanoparticles	83
5.1	Introduction	83
5.2	Results and Discussion.....	84

5.2.1	Characterization of cobalt sulfide nanoparticles synthesized using SDEDTC as a sulfur source	84
5.2.2	Characterization of cobalt sulfide nanoparticles synthesized using TAA as a sulfur source.....	95
5.3	Conclusions	105
5.4	References	107
Chapter 6: Toxicity Assessment of as-synthesized Copper and Cobalt Sulfide Nanoparticles		109
6.1	Introduction	109
6.2	Results and Discussion.....	110
6.2.1	Toxicity studies of Copper sulfide nanoparticles.....	110
6.2.2	Toxicity Studies of Cobalt Sulfide Nanoparticles	114
6.3	Conclusion.....	118
6.4	References	120
Chapter 7: <i>In vitro</i> Imaging of cellular material using Copper Sulfide Nanoparticles		122
7.1	Introduction	122
7.2	Results and Discussion.....	123
7.2.1	Development of Fluorescent Probes	124
7.2.2	Treatment of Cells to Induce Apoptosis	125
7.2.3	Imaging of Hek-293 and HeLa cells using Fluorescent Probes.....	126
7.3	Conclusion.....	132
7.4	References	133
Chapter 8: General Conclusions and Recommendations.....		136

8.1	Conclusions	136
8.2	Recommendations and Future Work.....	138

LIST OF FIGURES

Figure 2.1: An illustration of the size scale depicted by object of various sizes [8]	8
Figure 2.2: Size dependent colour emission observed in quantum dot solutions of various sizes [17].	9
Figure 2.3: Comparison of the arrangement of energy states or bands between a bulk material and a quantum dot. Also shown is the effect of the quantum dot size on the band gap and light emitted [33].	11
Figure 2.4: Schematic diagram illustrating the path of an electron after being excited by a photon [38].	12
Figure 2.5: Schematic diagram depicting the density of states as system dimensionality is reduced. The density of states in different confinement configurations such as bulk, quantum well, quantum wire and quantum dot [53].	14
Figure 2.6: Graph depicting the various stages within LaMer's nucleation theory of particle formation and growth [104].	19
Figure 2.7: An illustration of the process by which bigger nanoparticles grow bigger in size as smaller nanoparticles disappear into solution in a process called Ostwald ripening [122].	20
Figure 2.8: Potential biological applications of semiconductor nanoparticles functionalized with various biomolecules [14].	23
Figure 2.9: Simultaneous imaging of tumour cells in a live mouse using multi-color semiconductor nanoparticles [158].	24
Figure 2.10: Comparison of the excitation (a) and emission (b) spectra for a fluorescent dye (Rhodamine 6G) and quantum dots (CdSe) [158].	25
Figure 2.11: Various mechanisms through which quantum dots are likely to induce cytotoxicity [221].	30
Figure 2.12: Chemical structures of GSH (A), TGA (B), 18C6 (C) and L-Carn (D) to be used as capping ligands.	34

Figure 4.1: Absorption spectra of copper sulfide nanoparticles capped with GSH, TGA, 18C6 and L-Carn synthesized at 50 (A) and 95 °C (B) using SDEDTC as a sulfur source.	60
Figure 4.2: Emission spectra of copper sulfide nanoparticles capped with GSH, TGA, 18C6 and L-Carn synthesized at 50 (A) and 95 °C (B) using SDEDTC as a sulfur source.	61
Figure 4.3: HR-TEM images of copper sulfide nanoparticles capped with GSH (A), TGA (B), 18C6 (C) and L-Carn (D) synthesized at 50 °C using SDEDTC as a sulfur source.	62
Figure 4.4: HR-TEM images of copper sulfide nanoparticles capped with GSH (A), TGA (B), 18C6 (C) and L-Carn (D) synthesized at 95 °C using SDEDTC as a sulfur source.	63
Figure 4.5: XRD patterns of copper sulfide nanoparticles capped with GSH (A), TGA (B), 18C6 (C) and L-Carn (D) synthesized at 50 °C using SDEDTC as a sulfur source.	64
Figure 4.6: XRD spectra of copper sulfide nanoparticles capped with GSH (A), TGA (B), 18C6 (C) and L-Carn (D) synthesized at 95 °C using SDEDTC as a sulfur source.	65
Figure 4.7: FT-IR spectra of pristine GSH (A) and GSH capped copper sulfide nanoparticles synthesized at 50 (B) and 95 °C (C) using SDEDTC as a sulfur source.	66
Figure 4.8: FT-IR spectra of pristine TGA (A) and TGA capped copper sulfide nanoparticles synthesized at 50 (B) and 95 °C (C) using SDEDTC as a sulfur source.	67
Figure 4.9: FT-IR spectra of pristine 18C6 (A) and 18C6 capped copper sulfide nanoparticles synthesized at 50 (A) and 95 °C (B) using SDEDTC as a sulfur source.	68
Figure 4.10: FT-IR spectra of pristine L-Carn (A) and L-Carn capped copper sulfide nanoparticles synthesized at 50 (B) and 95 °C (C) using SDEDTC as a sulfur source.	69
Figure 4.11: Absorption spectra of copper sulfide nanoparticles capped with GSH, TGA, 18-crown-6 and L-carnosine synthesized at 50 (A) and 95 °C (B) using TAA as a sulfur source.	70
Figure 4.12: Emission spectra of copper sulfide nanoparticles capped with GSH, TGA, 18C6 and L-Carn synthesized at 50 (A) and 95 °C (B) using TAA as a sulfur source.	71
Figure 4.13: HR-TEM images of copper sulfide nanoparticles capped with GSH (A), TGA (B), 18C6 (C) and L-Carn (D) synthesized at 50 °C using TAA as a sulfur source.	72

Figure 4.14: HR-TEM images of copper sulfide nanoparticles capped with GSH (A), TGA (B), 18C6 (C) and L-Carn (D) synthesized at 95 °C using TAA as a sulfur source.	73
Figure 4.15: XRD spectra of copper sulfide nanoparticles capped with GSH (A), TGA (B), 18C6 (C) and L-Carn (D) synthesized at 50 °C using TAA as a sulfur source.	74
Figure 4.16: XRD spectra of copper sulfide nanoparticles capped with GSH (A), TGA (B), 18C6 (C) and L-Carn (D) synthesized at 95 °C using TAA as a sulfur source.	75
Figure 4.17: FT-IR spectra of pristine GSH (A) and GSH capped copper sulfide nanoparticles synthesized at 50 (B) and 95 °C (C) using TAA as a sulfur source.	76
Figure 4.18: FT-IR spectra of pristine TGA (A) and TGA capped copper sulfide nanoparticles synthesized at 50 (B) and 95 °C (C) using TAA as a sulfur source.	77
Figure 4.19: FT-IR spectra of pristine 18C6 (A) and 18C6 capped copper sulfide nanoparticles synthesized at 50 (B) and 95 °C (C) using TAA as a sulfur source.	77
Figure 4.20: FT-IR spectra of pristine L-Carn (A) and L-Carn capped copper sulfide nanoparticles synthesized at 50 (B) and 95 °C (C) using TAA as a sulfur source.	78
Figure 5.1: Absorption spectra of cobalt sulfide nanoparticles capped with GSH, TGA, 18C6 and L-Carn synthesized at 50 °C (A) and 95 °C (B) using SDEDTC as a sulfur source.	85
Figure 5.2: Emission spectra of cobalt sulfide nanoparticles capped with GSH, TGA, 18C6 and L-Carn synthesized at 50 °C (A) and 95 °C (B) using SDEDTC as a sulfur source.	86
Figure 5.3: HR-TEM images of cobalt sulfide nanoparticles capped with GSH (A), TGA (B), 18C6 (C) and L-Carn (D) synthesized at 50 °C using SDEDTC as a sulfur source.	87
Figure 5.4: HR-TEM images of cobalt sulfide nanoparticles capped with GSH (A), TGA (B), 18C6 (C) and L-Carn (D) synthesized at 95 °C using SDEDTC as a sulfur source.	88
Figure 5.5: XRD spectra of cobalt sulfide nanoparticles capped with GSH (A), TGA (B), 18C6 (C) and L-Carn (D) synthesized at 50 °C using SDEDTC as a sulfur source.	89
Figure 5.6: XRD spectra of cobalt sulfide nanoparticles capped with GSH (A), TGA (B), 18C6 (C) and L-Carn (D) synthesized at 95 °C using SDEDTC as a sulfur source.	90

Figure 5.7: FT-IR spectra of pristine GSH (A) and GSH capped cobalt sulfide nanoparticles synthesized at 50 (B) and 95 °C (C) using SDEDTC as a sulfur source.	91
Figure 5.8: FT-IR spectra of pristine TGA (A) and TGA capped Co_xS_y nanoparticles synthesized at 50 (B) and 95 °C (C) using SDEDTC as a sulfur source.	92
Figure 5.9: FT-IR spectra of pristine 18C6 (A) and 18C6 capped Co_xS_y nanoparticles synthesized at 50 (A) and 95 °C (B).	93
Figure 5.10: FT-IR spectra of pristine L-Carn (A) and L-Carn capped Co_xS_y nanoparticles synthesized at 50 (B) and 95 °C (C) using SDEDTC as a sulfur source.	94
Figure 5.11: Absorption spectra of cobalt sulfide nanoparticles capped with GSH, TGA, 18C6 and L-Carn synthesized at 50 (A) and 95 °C (B) using TAA as a sulfur source.....	96
Figure 5.12: Photoluminescence spectra of cobalt sulfide nanoparticles capped with GSH, TGA, 18C6 and L-Carn synthesized at 50 (A) and 95 °C (B) using TAA as a sulfur source. 97	
Figure 5.13: HR-TEM images of cobalt sulfide nanoparticles capped with GSH (A), TGA (B), 18C6 (C) and L-Carn (D) synthesized at 50 °C using TAA as a sulfur source.....	98
Figure 5.14: HR-TEM images of cobalt sulfide nanoparticles capped with GSH (A), TGA (B), 18C6 (C) and L-Carn (D) synthesized at 95 °C using TAA as a sulfur source.....	99
Figure 5.15: XRD spectra of cobalt sulfide nanoparticles capped with GSH (A), TGA (B), 18C6 (C) and L-Carn (D) synthesized at 50 °C using TAA as a sulfur source.	100
Figure 5.16: XRD spectra of cobalt sulfide nanoparticles capped with GSH (A), TGA (B), 18C6 (C) and L-Carn (D) synthesized at 95 °C using TAA as a sulfur source.	100
Figure 5.17: FT-IR spectra of pristine GSH (A) and GSH capped Co_xS_y nanoparticles synthesized at 50 (B) and 95 °C (C) using TAA as a sulfur source.....	101
Figure 5.18: FT-IR spectra of pristine TGA (A) and TGA capped Co_xS_y nanoparticles synthesized at 50 (B) and 95 °C (C) using TAA as a sulfur source.....	102
Figure 5.19: FT-IR spectra of pristine 18C6 (A) and 18C6 capped Co_xS_y nanoparticles synthesized at 50 (B) and 95 °C (C) using TAA as a sulfur source.....	103

Figure 5.20: FT-IR spectra of pristine L-Carn (A) and L-Carn capped Co_xS_y nanoparticles synthesized at 50 (B) and 95 °C (C) using SDEDTC as a sulfur source. 104

Figure 6.1: The cytotoxicity profiles of copper sulfide nanoparticles capped with GSH, TGA, 18C6 and L-Carn synthesized at 50 °C using SDEDTC as a sulfur source. The values are represented as the mean \pm standard deviation, n = 3. Error bars indicate the standard deviation..... 111

Figure 6.2: The cytotoxicity profiles of copper sulfide nanoparticles capped with GSH, TGA, 18C6 and L-Carn synthesized at 95 °C using SDEDTC as a sulfur source. The values are represented as the mean \pm standard deviation, n = 3. Error bars indicate the standard deviation..... 112

Figure 6.3: The cytotoxicity profiles of copper sulfide nanoparticles capped with GSH, TGA, 18C6 and L-Carn synthesized at 50 °C using TAA as a sulfur source. The values are represented as the mean \pm standard deviation, n = 3. Error bars indicate the standard deviation..... 113

Figure 6.4: The cytotoxicity profiles of copper sulfide nanoparticles capped with GSH, TGA, 18C6 and L-Carn synthesized at 95 °C using TAA as a sulfur source. The values are represented as the mean \pm standard deviation, n = 3. Error bars indicate the standard deviation..... 114

Figure 6.5: The cytotoxicity profiles of cobalt sulfide nanoparticles capped with GSH, TGA, 18C6 and L-Carn synthesized at 50 °C using SDEDTC as a sulfur source. The values are represented as the mean \pm standard deviation, n = 3. Error bars indicate the standard deviation..... 115

Figure 6.6: The cytotoxicity profiles of cobalt sulfide nanoparticles capped with GSH, TGA, 18C6 and L-Carn synthesized at 95 °C using SDEDTC as a sulfur source. The values are represented as the mean \pm standard deviation, n = 3. Error bars indicate the standard deviation..... 116

Figure 6.7: The cytotoxicity profiles of cobalt sulfide nanoparticles capped with GSH, TGA, 18C6 and L-Carn synthesized at 50 °C using TAA as a sulfur source. The values are

represented as the mean \pm standard deviation, n = 3. Error bars indicate the standard deviation.....	117
Figure 6.8: The cytotoxicity profiles of cobalt sulfide nanoparticles capped with GSH, TGA, 18C6 and L-Carn synthesized at 95 °C using TAA as a sulfur source. The values are represented as the mean \pm standard deviation, n = 3. Error bars indicate the standard deviation.....	118
Figure 7.1: Absorption spectra of bare (A) and antibody conjugated (B) copper sulfide nanoparticles.	124
Figure 7.2: Morphology of Hek-293 cells before (A) and after treatment with CoCl ₂ (B) and Doxorubicin (C) to induce hypoxia.	125
Figure 7.3: Morphology of HeLa cells before (A) and after treatment with CoCl ₂ (B) and Doxorubicin (C) to induce hypoxia.	126
Figure 7.4: Fluorescence imaging of CoCl ₂ treated Hek-293 cells stained with the CuS-HIF-1 α probe. Images A and B shows control cells (without probe) viewed under white and green light respectively. Images C and D shows cells stained with bare nanoparticles viewed under white and green light respectively. E and F shows cells stained with the fluorescent probe viewed under white and green light respectively.....	127
Figure 7.5: Fluorescence imaging of doxorubicin treated Hek-293 cells stained with the CuS-H2A.X probe. Images A and B shows control cells (without probe) viewed under white and green light respectively. Images C and D shows cells stained with bare nanoparticles viewed under white and green light respectively. E and F shows cells stained with the fluorescent probe viewed under white and green light respectively.....	128
Figure 7.6: Fluorescence imaging of CoCl ₂ treated HeLa cells stained with the CuS-HIF-1 α probe. Images A and B shows control cells (without probe) viewed under white and green light respectively. Images C and D shows cells stained with bare nanoparticles viewed under white and green light respectively. E and F shows cells stained with the fluorescent probe viewed under white and green light respectively.....	130
Figure 7.7: Fluorescence imaging of doxorubicin treated HeLa cells stained with the CuS-H2A.X probe. Images A and B shows control cells (without probe) viewed under white and	

green light respectively. Images C and D shows cells stained with bare nanoparticles viewed under white and green light respectively. E and F shows cells stained with the fluorescent probe viewed under white and green light respectively..... 131

LIST OF TABLES

Table 5.1: FT-IR data of cobalt sulfide nanoparticles capped with GSH synthesized using SDEDTC as a sulfur source.	91
Table 5.2: FT-IR data of cobalt sulfide nanoparticles capped with TGA synthesized using SDEDTC as a sulfur source.	92
Table 5.3: FT-IR data of cobalt sulfide nanoparticles capped with 18C6 synthesized using SDEDTC as a sulfur source.	93
Table 5.4: FT-IR data of cobalt sulfide nanoparticles capped with L-Carn synthesized using SDEDTC as a sulfur source.	95
Table 5.5: FT-IR data of cobalt sulfide nanoparticles capped with GSH synthesized using TAA as a sulfur source.	102
Table 5.6: FT-IR data of cobalt sulfide nanoparticles capped with TGA synthesized using TAA as a sulfur source.	103
Table 5.7: FT-IR data of cobalt sulfide nanoparticles capped with 18C6 synthesized using TAA as a sulfur source.	104
Table 5.8: FT-IR data of cobalt sulfide nanoparticles capped with L-Carn synthesized using TAA as a sulfur source.	105

LIST OF ABBREVIATIONS

0D:	O-dimensional
18C6:	18-crown-6
1D:	1-dimensional
2D:	2-dimensional
3D:	3-dimensional
ATCC:	American Type Culture Collection
BSA:	Bovine serum albumin
CNT:	Classical Nucleation Theory
CoS:	Cobalt Sulfide
CuS:	Copper Sulfide
DMEM:	Dulbeco's Modified Eagles Medium
DNA:	Deoxyribonucleic acid
DOS:	Density of States
EDC:	1-Ethyl-3-(3-Dimethylaminopropyl) Carbodiimide
FT-IR:	Fourier Transform Infrared Spectroscopy
GSH:	Glutathione
Hek-293:	Human embryonic kidney cells 293
L-carn:	L-carnosine
LED:	Light Emitting Diode
MAb:	Monoclonal Antibody

MBE:	Molecular Beam Epitaxy
MPA:	Mercaptopropionic Acid
MSA:	Mercaptosuccinic Acid
NHS:	N-Hydroxysuccinimide
NIR:	Near Infrared
nm:	Nanometres
PBS:	Phosphate buffered saline
PL:	Photoluminescence
QD:	Quantum Dot
SDEDTC:	Sodium Diethyldithiocarbamate
TAA:	Thioacetamide
TEM:	Transmission Electron Microscope
TGA:	Thioglycolic Acid
Uv:	Ultraviolet
XRD:	X-ray Diffraction Spectroscope

Chapter 1: Introduction

1.1 Background and Rationale

The search for advanced diagnostic systems to improve disease detection and management has been the focus of most research work in various study fields. This has prompted interaction amongst various study areas within the science arena, with nanotechnology in the forefront [1]. Innovation in the field of nanotechnology has shown potential to unlock key advances in the detection, diagnosis, treatment and management of infectious diseases [2]. Nanotechnology has pioneered the miniaturization of structures and materials to a nanometre scale, forming nanostructures and nanomaterials that are suitable to explore biological processes. It has also advanced the formation of larger structures (still within the nanometre scale), with enhanced properties, from the assembly of smaller atoms and molecules [3].

Nanomaterials have unique physical and chemical properties that are different from those of bulk materials from which they are formed [4]. These include high electron density and strong optical absorption (e.g. metal particles such as gold colloids), high photoluminescence (e.g. quantum dots or semiconducting nanomaterials), high phosphorescence, and also possess magnetic properties (e.g. Iron Oxide) [5]. Such properties present excellent opportunities for the design of novel and innovative nanostructures that can be used in various applications such as electronics, optoelectronics, energy storage applications, and most importantly in biomedical applications for therapeutic and diagnostic purposes [6,7]. The design of novel nanomaterials will assist in the development of sensitive and reliable diagnostic systems for the early detection of infectious diseases, thereby improving limitations associated with current detection systems.

Disease detection has been the main focus of biological research recently. In most cases, disease biomarkers are present in biological samples at very low concentrations and therefore highly sensitive detection methods are required. Microscopy detection has once been the gold standard in the detection of infectious diseases such as tuberculosis and cancer, and therefore improvements in the detection procedure could further enhance sensitivity and restore its use. Fluorescent probes for microscopy detection have been synthesized using organic dyes which have numerous limitations, such as a narrow absorption spectra and a

broad emission spectra to name but a few, that impact negatively on assay sensitivity. Use of semiconducting nanomaterials in the design of fluorescent probes for disease detection eliminates the aforementioned limitations and enhances the sensitivity of detection, and also allows for the detection of multiple disease analytes further improving the scope of detection which eliminates misdiagnosis.

For use in biological applications such as disease detection, nanomaterials must be functionalized with biomolecules that are capable of recognizing target analytes in biological samples [8]. In most cases, nanomaterials are synthesized using organometallic route which yields high quality nanostructures that are insoluble in aqueous media, thereby limiting their use in biological assays. Therefore, nanomaterials synthesized this way require additional processing to render them biocompatible as biological reactions are hydrophilic in nature. The non-polar organic capping agents used during organometallic synthesis of nanomaterials can be replaced or modified with polar inorganic ligands using various processes including ligand exchange, hydrophobic interaction and encapsulation [9,10].

This then prompted the synthesis of these nanomaterials in polar solvents which produce stable, hydrophilic, and biocompatible QDs that can be used directly in biological assays without the need for ligand exchange [11-13]. This method utilizes water soluble thiols as stabilizing agents or capping ligands for the synthesized nanoparticles. In the aqueous synthesis route, it is much easier to control the reaction kinetics and also passivate surface dangling bonds [14]. Moreover, aqueous synthesis is cheaper, much simpler to perform, and highly environmentally friendly compared to the organometallic synthetic route [15]. This method also allows for the use of low reaction temperatures and also yields nanoparticles that are smaller in size as compared to those obtained after encapsulation of hydrophobic nanomaterials with hydrophilic ligands [16].

1.2 Aims and Objectives

The aim of this project is to synthesize biocompatible nanoparticles and use them in the development of fluorescent probes for disease imaging.

Objectives to fulfil the above aim include:

- Synthesis and characterization of water soluble/ biocompatible nanoparticles using an aqueous synthesis route. Copper Sulfide and Cobalt Sulfide were selected as nanomaterials to be used herein;
- Bio-conjugation of as-synthesized nanoparticles to biomolecules;
- Use or application of the bio-conjugated nanoparticles (fluorescent probes) to demonstrate proof of concept in the imaging of mammalian cells using fluorescence microscopy

1.3 Thesis Outline

This thesis is presented in eight (8) chapters. Chapter 1 introduces the main focus of this study, highlighting the problem statement, the motivation behind the study and the aims and objectives of the research conducted.

Chapter 2 outlines the properties of semiconducting nanomaterials that make them suitable candidates for use in biological assays, including the different methods used in their synthesis and also their cytotoxicity properties *in vitro*. Additionally, the use of these nanomaterials in various applications is mentioned as well as their performance as fluorescent probes in imaging applications.

Chapter 3 outlines the experimental conditions and instrumentation used in the synthesis and characterization of copper and cobalt sulfide nanomaterials. Moreover, the experimental conditions for cytotoxicity testing and imaging applications of as-synthesized nanoparticles are highlighted.

Chapters 4 and 5 report the results obtained in the synthesis and characterization of CuS and CoS nanoparticles using sodium diethyldithiocarbamate or thioacetamide as sulfur sources and four different capping agents, (i.e. glutathione, thioglycolic acid, 18-crown-6 and L-carnosine) and conducted at two different temperatures (50 and 95 °C).

Chapter 6 reports the cytotoxicity studies of as-synthesized CuS and CoS nanoparticles, using MT-4 cells. Chapter 7 focuses on the functionalization of CuS nanoparticles with monoclonal antibodies and their subsequent use in imaging on Hek-293 and HeLa cells. Chapter 8 gives the general conclusions on the overall study and recommendations for future work

1.4 References

- [1]. A. M. Smith, S. Dave, S. Nie, L. True and X. Gao. *Expert Rev. Mol. Diagn.*, **2006**, 6, 231 – 244.
- [2]. Y. Xing and J. Rao. *Cancer Biomarkers.*, **2008**, 4, 307 – 319.
- [3]. Z. Skeete, H. Cheng, E. Crew, I. L. Lin, W. Zhao, P. Joseph, S. Shan, H. Cronk, J. Luo, Y, Q. Zhang and C. J. Zhong. *ACS Appl Mater Interfaces.*, **2014**, 6, 21752 – 21768.
- [4]. A. J. Mieszawska, W. J. M. Mulder, Z. A. Fayad and D. P. Cormode. *Mol. Pharmaceutics.*, **2013**, 10, 831 – 847.
- [5]. H. Zhu, M. Z. Hu, L. Shao, K. Yu, R. Dabestani, M. B. Zaman and S. Liao. *J. Nanomater.*, **2014**, 1 – 14.
- [6]. K. Giribabu, R. Suresh, R. Manigandan, E. Thirumal, A. Stephen and V. Narayanan. *J. Mater. Sci: Mater Electron.*, **2013**, 24, 1888 – 1894
- [7]. P. Wu and X-P. Yan. *Chem. Soc. Rev.*, **2013**, 42, 5489 - 5521
- [8]. M. K. Wagner, F. Li, J. Li, X-F. Li and X. C. Le. *Anal Bioanal Chem.*, **2010**, 397, 3213 – 3224.
- [9]. W. W. Yu, E. Chang, R. Drezek and V. L. Colvin. *Biochem. Biophys. Res. Commun.*, **2006**, 348, 781 – 786.
- [10]. F. O. Silva, M. S. Carvalho, R. Mendonca, W. A.A. Macedo, K. Balzuweit, P. Reiss and M. A. Schiavon. *Nanoscale Res. Lett.*, **2012**, 7, 1 – 10.
- [11]. Y. He. *InTech.*, **2012**. ISBN 978-953-51-0483-4
- [12]. N. T. K. Thanh and L. A. W. Green. *Nano Today.*, **2010**, 5, 213 - 230.

[13]. A. Fontes, B. S. Santos, C. R. Chaves and R. C. B. Q. Figueiredo. *InTech*. ISBN: 978-953-51-0483-4

[14]. S. M. Farkhani and A. Valizadeh. *IET Nanobiotechnol.*, **2014**, 8, 59 – 76.

[15]. Y. Su, Y. He, H. Lu, L. Sai, Q. Li, W. Li, L. Wang, P. Shen, Q. Huang and C. Fan. *Biomaterials.*, **2009**, 30, 19 - 25

[16]. R. Schneider and L. Balan. *Intech.*, **2012**, 119 - 140.

Chapter 2: Literature Review

2.1 Nanotechnology

The emergence of the field of nanotechnology has unlocked numerous opportunities that seek to tackle challenges in the field of science, which in turn could be translated to solutions for the advancement of modern day society. Nanotechnology, as defined by the US National Nanotechnology Initiative (NNI), is the study and manipulation of matter at an atomic, molecular or macromolecular scale (dimensions ranging approximately between 1 and 100 nanometres), to unlock their unique properties that will enable innovative applications. It was observed that the self-ordering forces and properties of materials at nanoscale differ from those at the macro-scale [1-4].

For instance, the surface-to-volume ratio of a material increases as its dimensions are reduced to the nanoscale. Moreover, electronic energy states become discrete bringing forth unique electronic, optical, magnetic, and mechanical properties [5]. These unique properties (physical, chemical and optical properties) available when materials are reduced to nanoscale can be exploited for applications that alleviate societal challenges.

Therefore the primary aim of nanotechnology is to design, produce and characterize novel materials, devices and systems that have new and improved properties and functions when their size has been reduced to less than 100 nm [6]. A nanometre is one billionth (10^{-9}) of a meter, about 10 times the size of the smallest atom, for instance hydrogen, and 80 000 times less than the diameter of a strand of human hair [7]. Dimensions between approximately 1 and 100 nanometres are considered as the nanoscale, as illustrated in Figure 2.1.

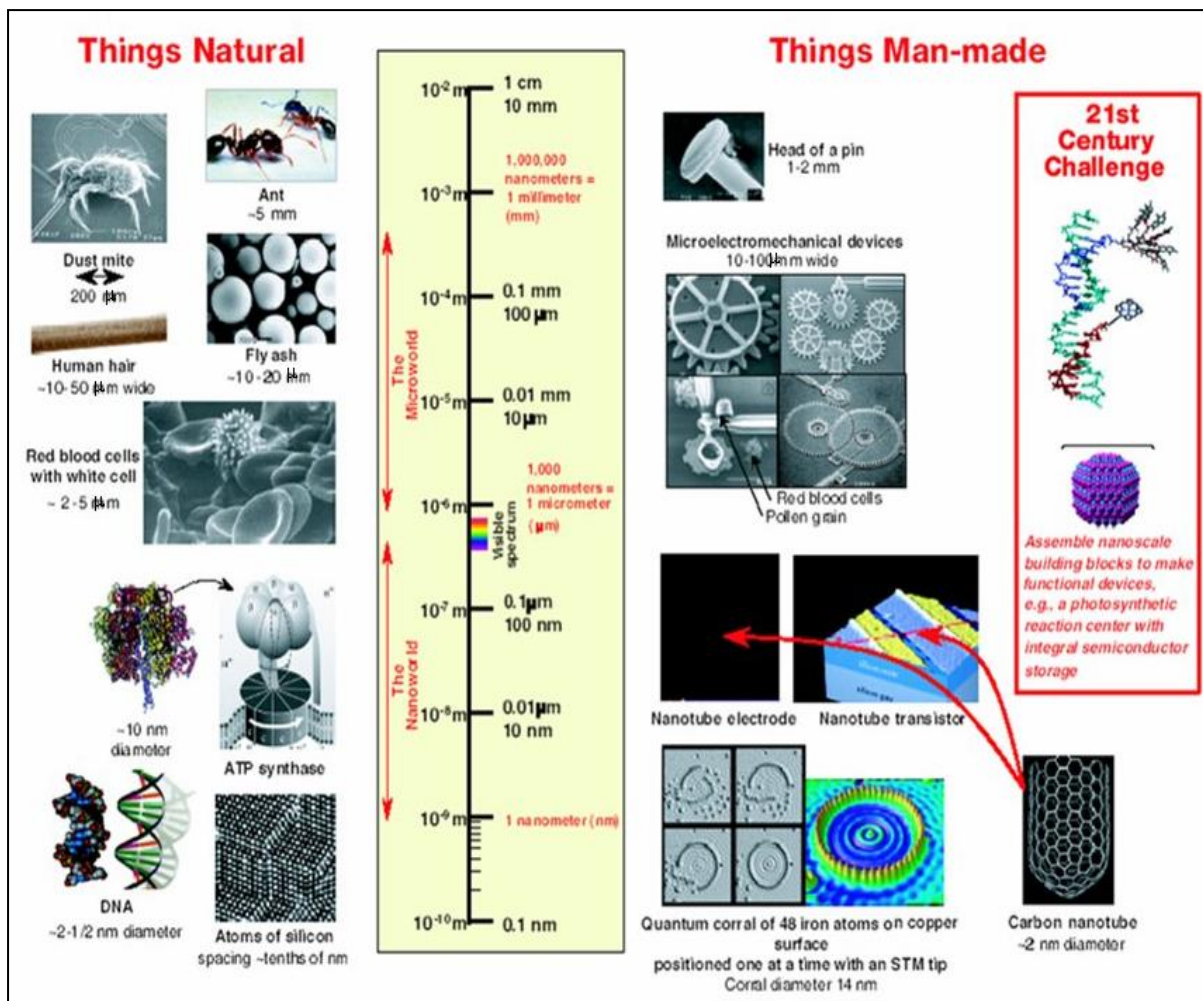


Figure 2.1: An illustration of the size scale depicted by object of various sizes [8]

Nanotechnology has continued to make a great impact in the field of science and technology, with more and more disciplines being actively involved. Its footprint spans across a vast range of disciplines including physics, chemistry, engineering, information technology, material sciences, as well as biology [9]. Thus nanotechnology has brought together all these scientific disciplines in creating new materials with superior properties.

2.2 Quantum dots or Semiconductor nanoparticles

Quantum dots are nanocrystals made of semiconductor materials of group II - IV, III - V or IV - VI elements [10]. These nanocrystals, often referred to as artificial atoms or zero-dimensional electron systems, are defined as particles that exhibit physical dimensions smaller than the exciton Bohr radius of the bulk material [11]. The Bohr radius is the distance

between an electron in the conduction band and its hole in the valence band, in an exciton. When a semiconductor is excited, an electron leaves the valence band and enters the conduction band creating an electron-hole pair that is transformed into an exciton by weak coulomb forces that exist between the electron and the hole [12].

According to literature, quantum dots or semiconducting nanomaterials range between 2 - 20 nm in diameter, and thus contain between hundred to a few thousand atoms. It has also been argued that the diameter of quantum dots should strictly be below 10 nm [13]. According to Drbohlavova *et al*, [14] the dimensions of a quantum dot are dependent on the material from which they are formed, and a system is considered to be a quantum dot when quantum confinement effects occur.

This size range allows nanomaterials to exhibit unique properties intermediate between those of their bulk materials and individual atoms or discrete molecules. This is usually motivated by the high surface to volume ratio of these nanomaterials which emanates from their reduced size [15]. Nanomaterials have been seen to contain an inherent ability to glow a particular colour when exposed to light of a particular wavelength, with the resulting colour dependent on their size, as shown in Figure 2.2 [16]. Smaller particles have a strong blue colour and particles have a strong red colour. This is due to the fact that small quantum dots have a larger band gap and therefore emit higher energy photons whereas larger quantum dots have a smaller band gap and emit low energy photons [17,18].

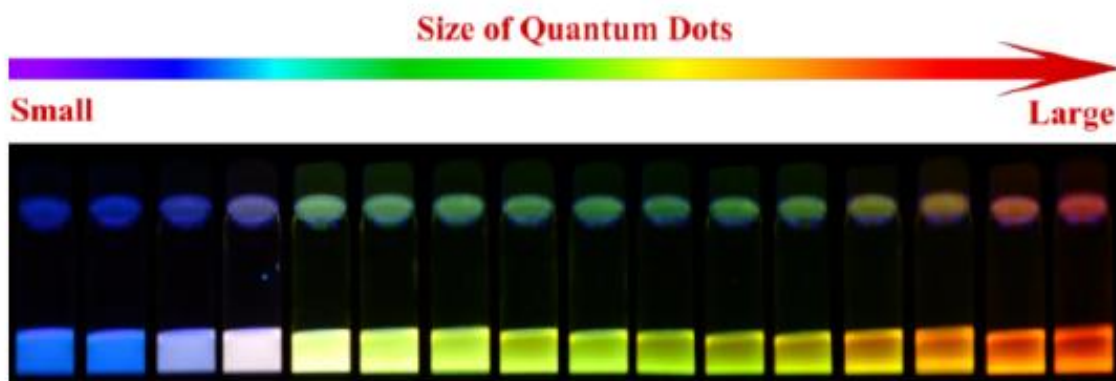


Figure 2.2: Size dependent colour emission observed in quantum dot solutions of various sizes [17].

The band gap therefore depends on the size of the nanomaterials, with the band gap increasing as the size of the quantum dot is decreased. This is one of the most interesting properties that have made nanomaterials superior over their bulk counterparts, and is known as the quantum confinement effect whereby size of the nanostructure determines its band gap, as the dimensions are decreased to levels below the Bohr exciton radius [19].

2.2.1 Properties of Semiconductor Nanomaterials

Semiconductor Nanomaterials have attracted much attention over other nanoparticle systems due to their amazing optical and electronic properties, not found in their counterparts. One of the most unique properties of these nanomaterials is the size dependant colour emission, which is mainly due to quantum confinement as previously highlighted [20]. This allows properties such as the band gap, emission colour, and absorption spectrum to be highly tunable, as the size distribution of semiconductor nanomaterials can be controlled during fabrication [21 - 25].

2.2.1.1 Optical Properties

As was indicated earlier, semiconductor nanomaterials exhibit size dependable optical properties that are attributed to the phenomena of quantum confinement. The quantum confinement effect is brought about by the entrapment or confinement of energy bands to discrete levels due to the increase in the band gap as a result of reduction of the nanomaterials size to nanoscale levels [26]. As such, it has become possible to manipulate optical properties of a particular nanomaterial such as the spectral width, position, and profile of the luminescence band through direct control of the size and the size distribution of the nanomaterial [27,28].

As the size of a bulk semiconductor is decreased to nanoscale, electrons within the semiconductor become confined into a small space, sometimes referred to a “quantum box” [29]. As the dimensions of the semiconductor are reduced further to below the exciton Bohr radius, the continuous energy bands collapse and become quantized according to Pauli’s exclusion principle, thereby forming discrete energy levels similar to those of atoms [30, 31].

The discrete structure of the newly formed energy states forms a discrete absorption spectrum that is different to the continuous absorption spectrum of the bulk semiconductor [32]. The energy levels in a bulk semiconductor are termed “continuous” because they are compact. Therefore there is a negligible energy difference between them. Figure 2.3 illustrates the difference in energy levels or bands between a bulk material and a quantum dot.

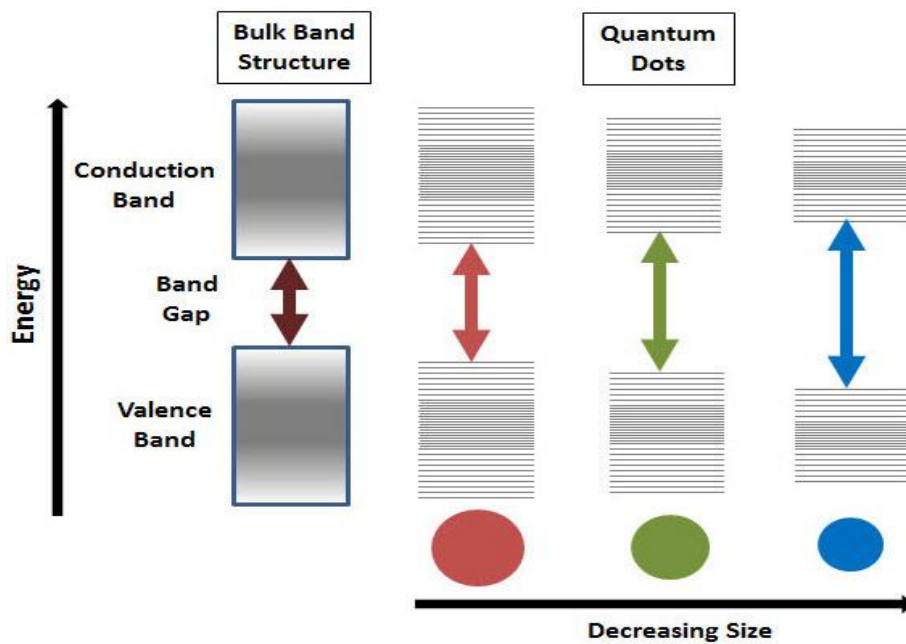


Figure 2.3: Comparison of the arrangement of energy states or bands between a bulk material and a quantum dot. Also shown is the effect of the quantum dot size on the band gap and light emitted [33].

A decrease in the dimensions of the semiconductor nanomaterial results in an increase in the energy difference (band gap) between the conductive and valence bands [34]. Consequently, there is an increase in the amount of energy ($h\nu$) required to excite an electron within the semiconductor nanomaterial from the conduction band to the valence band [35]. A photon with energy less than the band gap cannot be absorbed by the semiconductor. When excitation occurs, a semiconductor nanocrystal absorbs photons which causes the electrons within the nanocrystal to absorb energy and create excitons, i.e. an electron-hole (quasi

particle) pair. Upon relaxation, as the electron returns to the ground state, the electron and the hole recombine resulting in the release or emission of photons [36].

Light emission by semiconductor nanomaterials is known as fluorescence or luminescence. The colour of light emitted by semiconductor nanomaterials is dependent on the width of the energy band gap of the nanomaterial [37, 38]. Below (Figure 2.4) is a schematic diagram illustrating a semiconductor absorbing a photon causing the electron to be excited from the valence band to the conductive band, and its subsequent light emission as the electron returns to its original state.

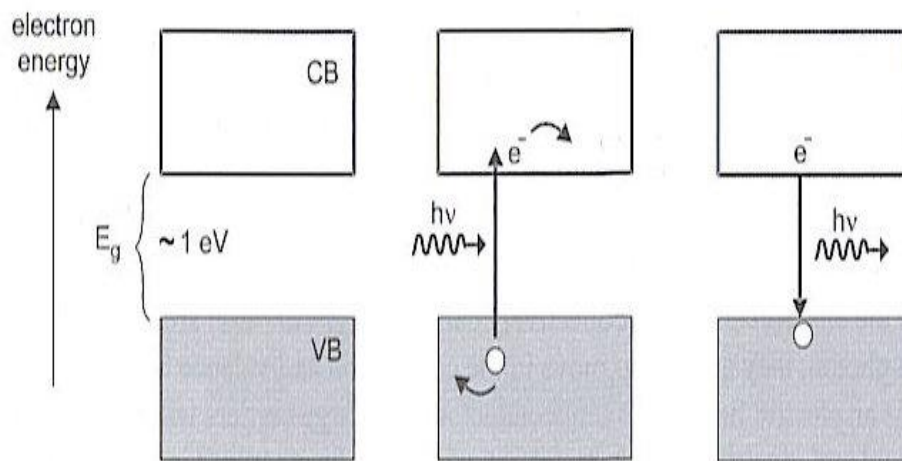


Figure 2.4: Schematic diagram illustrating the path of an electron after being excited by a photon [38].

2.2.1.2 Electronic Properties

Quantum confinement is induced by relatively few atoms within a semiconductor nanomaterial system, in which the excitons within the material are now trapped and subjected into a relatively smaller space that is comparable to the size of the materials Bohr radius [39]. This phenomenon occurs when dimensions of a material are small enough such that the electronic density of states of the material is affected or altered [40 - 43]. The dimensionality

of a material is of utmost importance as it determines the number of dimensions in which the carriers (electrons or holes) of the material act as free carriers. When the dimensionality of the region that constrains the electrons wave function is reduced to zero, the density of state changes dramatically and the material possess new enhanced properties [44, 45].

The electronic structure of a semiconductor material is depicted or measured by means of the density of states (DOS) [46]. This phenomenon refers to the number of quantum states per unit energy, i.e. how densely packed the quantum states are in a particular system [47]. As the dimensionality of a material or system is reduced, a change in the density of electron states occurs from a continuum of state to a much more discrete state, as seen in Figure 2.3 [48].

In a 3-dimensional system such as a bulk semiconductor, where density of states is proportional to the square root of the electron energy, the energy levels are reported to be continuous. In a 2-dimensional system, such as the quantum well system, the electrons are confined in one dimension and therefore the density of electron states assumes a step like pattern. In a 1-dimensional system, such as the quantum wire system, the electrons are confined in two dimensions and therefore the density of electron states forms a line-like pattern. Lastly, in a 0-dimensional system such as quantum dots, where the number of atoms in the lattice is very minimal and electron motion is confined in all dimensions, the density of electron states moves from the continuous ‘band’ like feature observed in the 3-dimensional model and assumes a more discrete pattern, since the energy levels are now separated by a considerable amount of energy [49, 50]. This density of electron states is similar to that of atoms since the charge carriers can occupy only a restricted set of energy levels [51, 52]. This transformation of the density of electron states as a result of change in dimensionality of material is depicted in Figure 2.5.

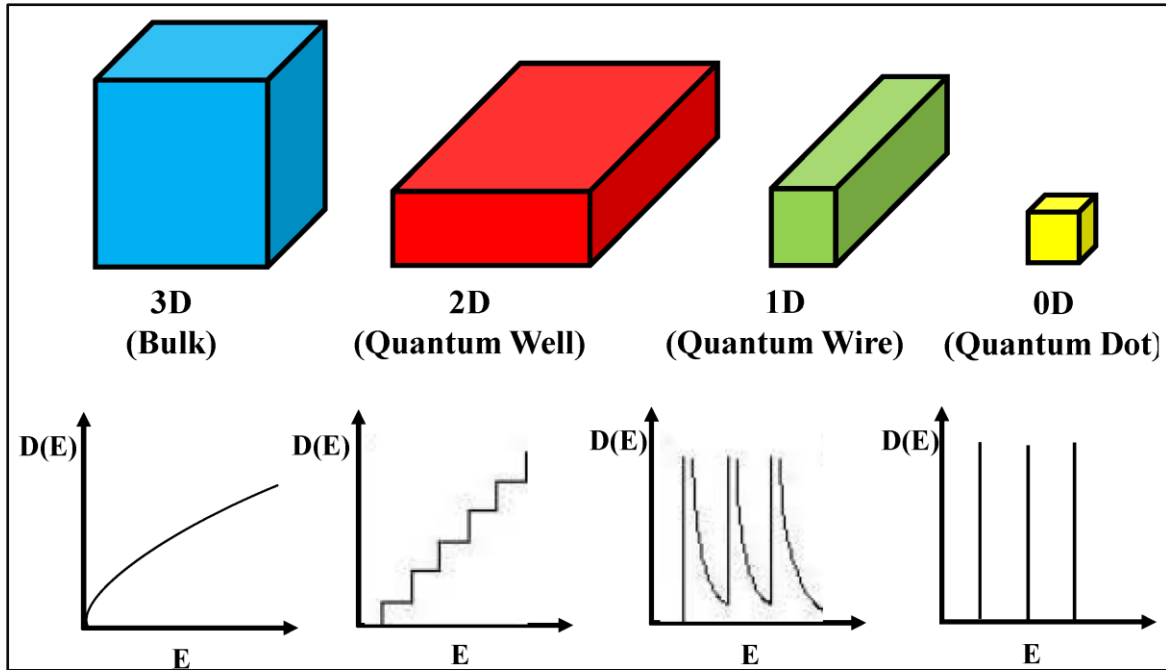


Figure 2.5: Schematic diagram depicting the density of states as system dimensionality is reduced. The density of states in different confinement configurations such as bulk, quantum well, quantum wire and quantum dot [53].

2.2.2 Methods for Synthesizing Semiconductor Nanoparticles

The synthesis of highly monodispersed, crystalline, shape controlled semiconductor nanoparticles with a narrow size distribution is of utmost importance in the applications in which these nanocrystals are to be used [54]. Since their discovery in the 1980s, semiconductor nanoparticles have been synthesized and used in a myriad of applications across the science arena [55]. In most cases, synthesis of semiconductor nanoparticles is directed or determined by the applications in which these nanocrystals are to be used in. In accordance with the laws of nanotechnology, synthesis of nanostructures can be attributed to two approaches, i.e. the top-down and the bottom-up approach. The top down approach yields quantum dots through the usage of synthesis techniques such as molecular beam epitaxy (MBE), ion implantation, e-beam lithography, and X-ray lithography, whereas the bottom up approach yields quantum dots by self-assembly following a chemical reduction process in solution [56-59]. Within the bottom-up approach, numerous synthetic techniques have been used to produce quantum dots but the most widely used techniques can be grouped

into two categories according to the nature of the solvent used, i.e. the organometallic and the aqueous synthesis routes, collectively known as colloidal synthesis [60, 61].

2.2.2.1 Organometallic Synthesis Route

This mode of synthesis was first reported by Bawendi *et al*, [62] and is considered to be amongst the simplest methods used for the production of high quality, nearly monodisperse semiconductor nanomaterials [63]. This method usually consists of three components, namely, precursors, a surfactant and an organic solvent, which in some cases serves as both the surfactant and a solvent [64, 65]. This technique usually involves the use of high temperature, non-polar solvents such as trioctylphosphine (TOP), trioctylphosphine oxide (TOPO) or hexadecyl amine (HDA) that have long alkyl chains.

Nanoparticles are produced by way of a pyrolysis reaction wherein organometallic reagents are injected into a hot hydrophobic organic solvent, wherein the solvent can serve as both the solvent and the capping agent to coordinate with unsaturated metal atoms on the surface of the synthesized semiconductor nanoparticles [66, 67]. The capping agent ensures that no bulk semiconductors are formed during this process and that the synthesized quantum dots are stable and will not form aggregates as they grow [68 - 70]. The coordinating solvents act as ligands by attaching to the surface of semiconductor nanoparticles through their terminal functional groups (phosphines, phosphine oxides, and amines); with their alkyl chains forming a monolayer that spans the nanoparticles. This mode of synthesis has been credited with producing highly monodisperse nanomaterials, with highly crystalline cores that exhibit narrow size distributions and symmetrical photoluminescence spectra or high photoluminescence quantum yield [71].

This method however has a number of drawbacks that have led to most researchers looking for an alternative synthesis route. Firstly, due to the use of organic coordinating solvents, the resulting nanoparticles are highly hydrophobic and therefore are only miscible in non-polar solvents such as toluene, chloroform, and hexane. This therefore restricts their use in a biological system *in vitro* [72]. To mitigate this problem various methods have been devised whereby the hydrophobic surface-capping monolayer created by the coordinating ligands is substituted with hydrophilic molecules such as thiol groups or amines which render the

nanomaterials hydrophilic, but this too compromises their photoluminescence yield [73, 74]. Other drawbacks associated with this method of synthesis include the use of pyrophoric, unstable, costly, and toxic organometallic raw materials. In some instances the reaction process lacks control and reproducibility [75 - 77].

2.2.2.2 Aqueous Synthesis Route

This mode of synthesis involves the production of semiconductor nanoparticles in aqueous media using less toxic and biocompatible solvents, i.e. water. It also involves the use of water soluble small organic molecules, functionalized short chain thiols, and thiol groups. These serve various roles including acting as stabilising agents for the synthesized nanoparticles, passivation of surface dangling bonds, and improving solubility and functionality of resulting nanoparticles [78, 79]. Moreover, use of thiol groups allows for easy control of reaction kinetics and help control the growth rate and size of semiconductor nanoparticles [80].

This method usually employs heavy metals such as acetates, nitrates, or chlorides that are easily soluble in water as precursors [81]. Some of the small organic molecules mostly reported in this method are thioglycolic acid (TGA), mercaptopropionic acid (MPA), mercaptosuccinic acid (MSA), glutathione (GSH), and L- Cysteine (Cys). These molecules contain both the sulfhydryl and carboxyl functional groups [82 - 84]. The sulfhydryl end of the capping molecule attach to the quantum dot surface while the carboxyl functional group remains available. The free carboxyl functional group create a hydrophilic layer that spans the quantum dots rendering them soluble in biological media. Furthermore, these free carboxyl functional groups provide a “functionalized” surface that can carry out further surface modification processes such as bioconjugation or PEGylation [85, 86].

Aqueous synthesis was found to produce semiconductor nanomaterials with lower quantum yields and large size distribution as compared to the organometallic synthesis route [87]. Nonetheless, efforts have been made to improve the quality of nanoparticles by changing parameters such as the type of capping agent, type of precursor, and molar ratio of reactants. As a result, aqueous synthesis has now been the preferred mode of synthesis as it yields less toxic and environmental friendly nanomaterials [88, 89].

2.2.3 Semiconductor Nanoparticle Formation Process

Understanding the growth mechanism in which nanoparticles are formed during a synthesis reaction is of utmost importance for the synthesis of high quality, monodisperse semiconductor nanoparticles. It has been reported on numerous occasions that nanoparticle formation occurs over two processes, namely nucleation and growth processes [90]. The nucleation process occurs in the early stages of the reaction, and creates a “seed” that eventually grows into nanoparticles as the reaction progresses further. It has been reported that the control and separation of these processes is crucial in synthesizing monodisperse nanoparticles [91 - 93].

2.2.3.1 Nucleation

Nucleation is the first step that precedes the formation of a new structure and this occurs through the self-assembly of reactants. By definition, nucleation is the process whereby free molecules or atoms of a reactant phase self-assemble to form a nucleus or thermodynamically stable cluster that serves as a template from which nanoparticles grow [94 - 96]. The phase of the cluster therefore resembles that of the envisaged product or nanoparticles, and the cluster should be large enough to be able to grow irreversibly into bigger particles of the desired size. This happens when the nuclei or newly formed cluster exceed a specific size known as the critical size that is determined by the competition between the aggregate curvature and the free energy, thereby facilitating the emergence of a new phase [97, 98].

Nucleation can either occur homogeneously or heterogeneously, and is controlled by the presence or absence of impurities within the reaction. Heterogeneous nucleation is reported to occur at the surface of particles in solution, where it provides nucleation sites for seed mediated growth. Homogenous nucleation occurs spontaneously when a supercritical state known as supersaturation has been achieved [99, 100]. Supersaturation is defined as the difference in chemical potential between a molecule in solution and that in the bulk of the crystal phase, and is denoted as follows:

$$\Delta\mu = \mu_s - \mu_c$$

Where μ_s is the chemical potential of a molecule in solution and μ_c is the chemical potential of the molecule in the bulk crystal. Supersaturation is very important phenomenon which is considered the driving force for nucleation and growth to occur. The rate at which nucleation occurs can be expressed as follows:

$$Rate = v \exp(-\Delta F^*/kT)$$

where v is an attempt frequency of the order of the spin-flip frequency (v also depends on supersaturation), ΔF^* is the height of the free-energy barrier that must be surmounted, k is the Boltzmann constant, and T is the absolute temperature [101, 102]. According to literature, the process of nucleation is better understood through LaMer's nucleation theory [103]. This is based on the classical nucleation theory (CNT) developed by Becker and Döring many years ago. Together with its modifications, the LaMer model is regarded as the only commonly accepted model that illustrates the general mechanism through which nanoparticles are formed [104].

In this process, often referred to as the “burst nucleation process”, precursors decompose instantaneously to form multiple nuclei and simultaneously through homogenous nucleation and then continue to grow without further nuclei formation. LaMer's theory proposes that synthesis should be tailored in such a way that monomer concentration rises rapidly and exceeds the saturation concentration (C_s) for an extended period of time. This will then promote the occurrence of a short burst of nucleation resulting in the instantaneous formation of a large number of nuclei, which can further grow swiftly to form nanoparticles. In unison, the monomer concentration decreases and therefore no additional nuclei are formed, leading to the next process known as growth [105 - 108].

According to Thanh *et al*, [97] LaMer's nucleation theory plays out in three different stages, as shown in Figure 2.6. The first stage sees a rapid increase in the concentration of monomers to reach a supersaturation level which favours homogeneous nucleation. In stage II, the monomer concentration continues to rise and saturation increases such that the monomers undergo burst nucleation. Initially (stage I, pre-nucleation stage), monomer concentration increases to reach the supersaturation level depicted as C_s . At this point, nucleation that can

happen is referred to as “effectively infinite”. In the second stage (stage II), saturation increases further to reach a self-nucleation level (C_{\min}) where nucleation activation energy is exceeded resulting in burst nucleation. In stage III, monomer concentration decreases and drops supersaturation levels to below self-nucleation level thereby bringing nucleation to a halt, and making way for the growth phase [109 - 111].

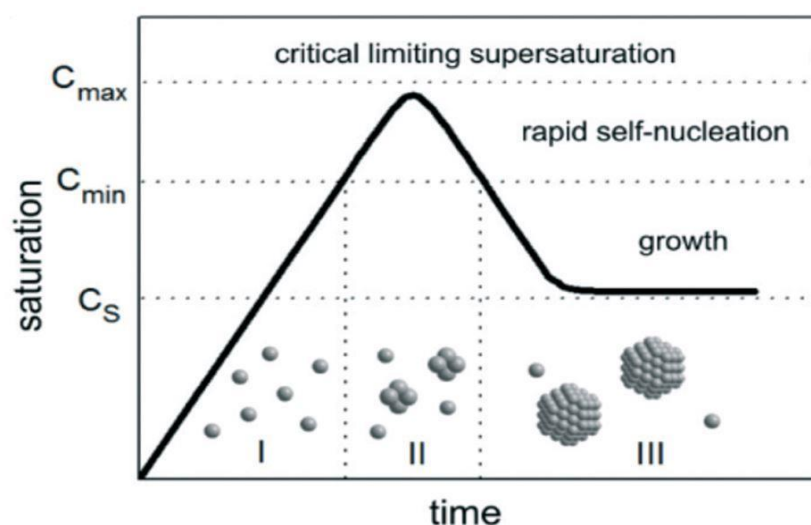


Figure 2.6: Graph depicting the various stages within LaMer’s nucleation theory of particle formation and growth [104].

2.2.3.2 Growth

Following the formation of numerous nuclei from the nucleation step, particle growth is initiated. Nuclei begin to grow from their surface resulting in the depletion of the monomer supply. This reduces monomer concentration to below the critical supersaturation level, thereby initiating a stop to the process of nucleation [112]. Nanoparticles are therefore formed as a result of growth from the nuclei formed during the nucleation process. Growth occurs via a series of carefully coordinated steps, which basically facilitate the incorporation of atoms or molecules into crystal surfaces resulting in an increase in crystal size. The steps include the transport or diffusion of atoms or monomers through solution towards the crystal

surface, attachment of atoms to the surface of the crystal, movement of atoms on the surface of the crystal and lastly the attachment of atoms to edges on the crystal surface [113, 114].

Nanoparticle growth has been attributed to various mechanisms such as Ostwald ripening, digestive ripening, Finke-Watzky mechanism, coalescence and orientated attachment, and the intraparticle growth mechanism. Ostwald ripening (diffusion limited) is the most predominant growth mechanism and is explained further in the subsequent section. These processes play out successively, and therefore the slowest process will control the overall crystal growth, hence growth is usually diffusion (step 1 is rate limiting) or surface (steps 2-4 are limiting) controlled [115, 116].

2.2.3.3 Ostwald Ripening

This particle growth mechanism is described as the process whereby larger particles grow from smaller particles by means of small clusters of molecules dissolving and transferring their mass to bigger clusters, as observed in Figure 2.7. Ostwald ripening was first reported by Ostwald in the 1900s, and is known to occur in situations whereby larger particles are more energetically stable than smaller particles [117 - 119]. In smaller-sized particles, atoms are loosely packed on the surface whereas in larger particles atoms are well ordered and packed in the interior. Therefore, as the overall energy of the system is lowered, molecules on the surface of the smaller-sized particles will detach and diffuse through the solution and finally attach to the surface of the larger particles [120, 121].

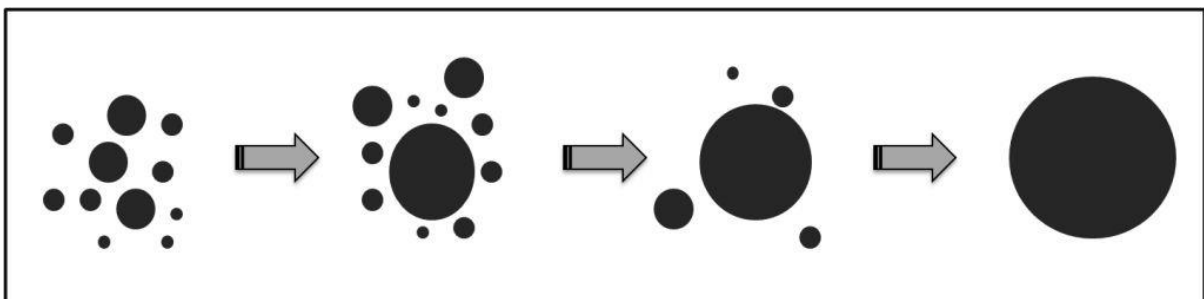


Figure 2.7: An illustration of the process by which bigger nanoparticles grow bigger in size as smaller nanoparticles disappear into solution in a process called Ostwald ripening [122].

The most studied form of Ostwald ripening was mathematically modelled and derived by Lifshitz, Slyozov and Wagner [123]. Their derivative was based on diffusion limited Ostwald ripening or in cases whereby the diffusion of material is the slowest process. They formulated a scenario that defines the margin between small shrinking particles and large growing particles. They introduced a concept of the critical radius (r_b) and compared it with the mean radius (r) of the particles in solution. This concept is therefore used to separate small particles that are shrinking (when $r < r_b$) from larger particles that are growing (when $r > r_b$). When the mean radius is the same as the critical radius ($r = r_b$), the growth is regarded as zero [124 - 127].

2.3 Metal Chalcogenides (Copper Sulfide and Cobalt Sulfide)

Metal chalcogenides have been the most preferred nanomaterials due to a number of reasons. These include, amongst others, their distinct physical and chemical properties which allow them to be used in a range of applications that exploit their electronic, optical and electrochemical features. Until recently, metal chalcogenides have been used mainly in the fabrication of energy devices such as fuel cells, light-emitting diodes, solar cells, lithium-ion batteries and supercapacitors [128 - 130]. Due to their amazing intrinsic properties, metal chalcogenides are now being used extensively in biological applications for the sensitive detection of target analytes. Biological applications in which metal chalcogenides have been used include cell imaging and tracking, sensing, molecular imaging, photothermal therapy, and drug delivery [131].

2.3.1 Copper Sulfide

Copper sulfide is a p-type semiconducting nanomaterial composed of group I and VI elements. These semiconductors are grouped amongst the least toxic nanomaterials and have thus been sought for use in biological applications. They are known to exist in two phases, namely the amorphous brown chalcocite and the green crystalline covellite. These nanomaterials are known to exist in various stoichiometric ratios which include covellite (CuS), anilite ($\text{Cu}_{1.75}\text{S}$), digenite ($\text{Cu}_{1.8}\text{S}$), djurlite ($\text{Cu}_{1.95}\text{S}$), and the copper rich chalcocite (Cu_2S) phases. Copper sulfide nanomaterials are known to have unique optical and electronic

properties. They are known to exhibit a stoichiometry dependent band gap that can be tuned from 1.2 – 1.5eV [132 - 136].

These properties can be tailored through the modification of their structure, morphology, stoichiometric composition and valence state. Copper sulfide nanomaterials have gained advantage over other metal chalcogenides as they are non-toxic, less expensive and stable under ambient conditions. As such, copper sulfide nanomaterials have been used extensively in the last few decades for various applications including photovoltaics, catalysis, memory devices and thermoelectric cooling materials. The most important feature of this semiconductor is based on the fact that its properties can be altered or tuned through the adjustment of its structure, morphology, stoichiometric composition and valence state. These semiconductors have been synthesized to a variety of shapes including nanoparticles, nanocubes, nanowires, nanorods, nanoplates, ball- flower, hollow cages and hollow spheres. Synthesis has been carried out using various methods including microwave irradiation, sonochemistry, solid state reaction and hydrothermal/solvothermal synthesis [137 - 142].

2.3.2 Cobalt Sulfide

Cobalt sulfide is a semiconductor composed of elements from group II – VI. It has been found to contain unique catalytic, electric, electrochemical, optical and magnetic properties. It is for this reason that this nanomaterial has been used across a myriad of applications within the energy sector [143, 144]. Owing to their high solar absorption which results from their strong intrinsic absorption together with surface morphology effects, these metal chalcogenides have been used extensively solar cell technology. It is recognised as one of the most complicated metal chalcogenides since it comes in various phases, chemical compositions and stoichiometric ratios that differ from each other. Stoichiometries include Co_4S_3 , Co_9S_8 , CoS , Co_{1-x}S , Co_3S_4 , Co_2S_3 and CoS_2 , which pose a challenge on shape-controlled synthesis [145 - 147]. It has been reported that the properties of cobalt sulfide are strongly dependent upon their size, shape, distribution and surface. Moreover, properties, morphology and stoichiometric composition of cobalt sulfide are greatly influenced by the mechanism used during synthesis [148].

2.4 Applications of Metal Chalcogenide Nanoparticles

Since their discovery and further fabrication in the early 80's, semiconductor nanomaterials have been the subject of interest in various fields. As such, they have been used in a myriad of applications which exploit their optical and electronic properties [149, 150]. The unlocking of various properties inherent to these nanomaterials has led researchers spreading semiconductor nanoparticle applications across a vast range of disciplines, both academically and industrially. Due to their ability to emit light upon excitation, with the colour of emitted light varying with the size of the semiconductor nanomaterial, they have also been successfully used in bio-sensing applications [151]. The use of semiconductor nanomaterials in various disciplines is explained in detail in subsequent sections.

2.4.1 Biological Assays

Semiconductor nanoparticles are amongst the first nanotechnology products to be applied in biological applications, and have now been seen in a number of commercial consumer and clinical products [152, 153]. Their effectiveness has been tested in a magnitude of biological and clinical assays that include immune-histochemical detection, drug delivery and therapeutics, bio-sensing, small animal imaging, and single-quantum dot tracking of extra- and intracellular targets [154]. Figure 2.8 illustrates various biological applications in which semiconductor nanoparticles have been used.

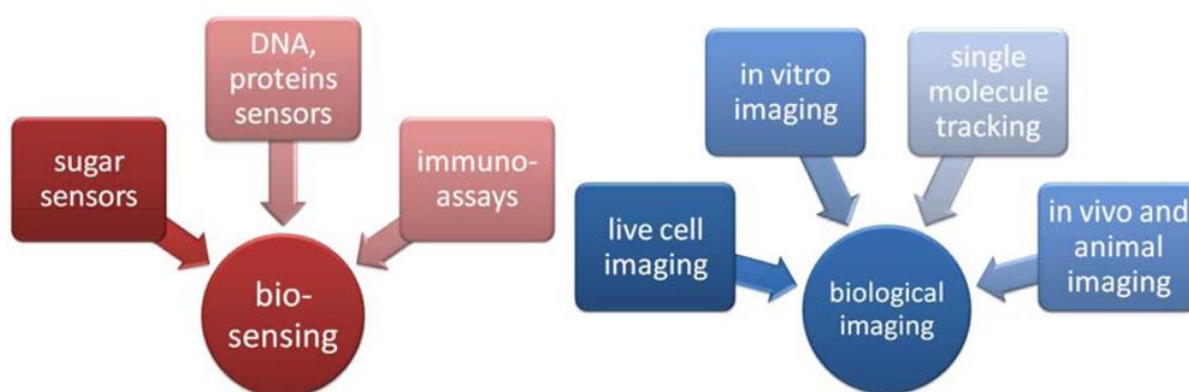


Figure 2.8: Potential biological applications of semiconductor nanoparticles functionalized with various biomolecules [14]

For decades, organic dye fluorophores have been at the forefront of biological analysis. With the advancement of times, technology evolving and new discoveries reported, flexibility is also expected from these fluorophores to help keep up with such changes. However, this is not the case, as these fluorophores continue to pose limitations on their use, therefore prompting for the search of more advanced agents [155].

Organic dyes that are currently in use are known to have narrow excitation spectra, and therefore can only be excited by light of a single wavelength, which gives challenges since this differs among specific dyes. However, semiconductor nanoparticles have been reported to circumvent this limitation since they have broad absorption spectra which allow excitation over a wide range of wavelengths [156]. As such, different coloured nanoparticles can be excited simultaneously using a single wavelength, as illustrated in Figure 2.9 [157].

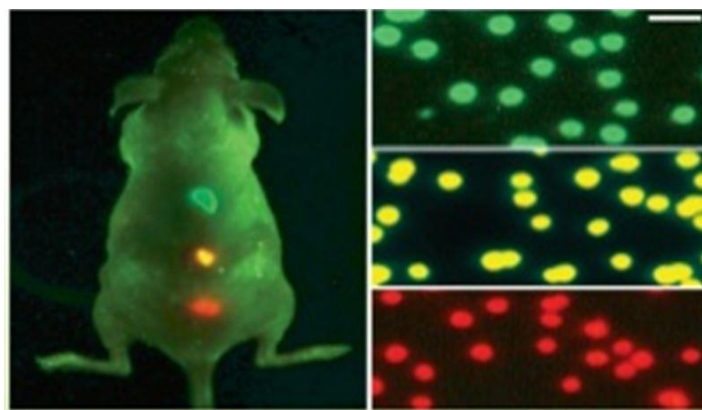


Figure 2.9: Simultaneous imaging of tumour cells in a live mouse using multi-color semiconductor nanoparticles [158].

Secondly, due to the broad emission spectra of most conventional dyes, it is not possible to use various fluorescent probes to tag different biological molecules due to a possible overlap between spectra of different dyes, making it difficult to simultaneously resolve their spectra [159]. However, this is not the case with quantum dots. As was indicated earlier, semiconductor nanoparticles have narrower and symmetric emission spectra compared to fluorescent dyes, which allows multiple quantum dots to be excited by the same light source and easily separate their spectra. This is a very useful property during biological imaging.

Figure 2.10 illustrates the differences between the absorption and emission spectra of organic dyes and that of semiconductor nanoparticles.

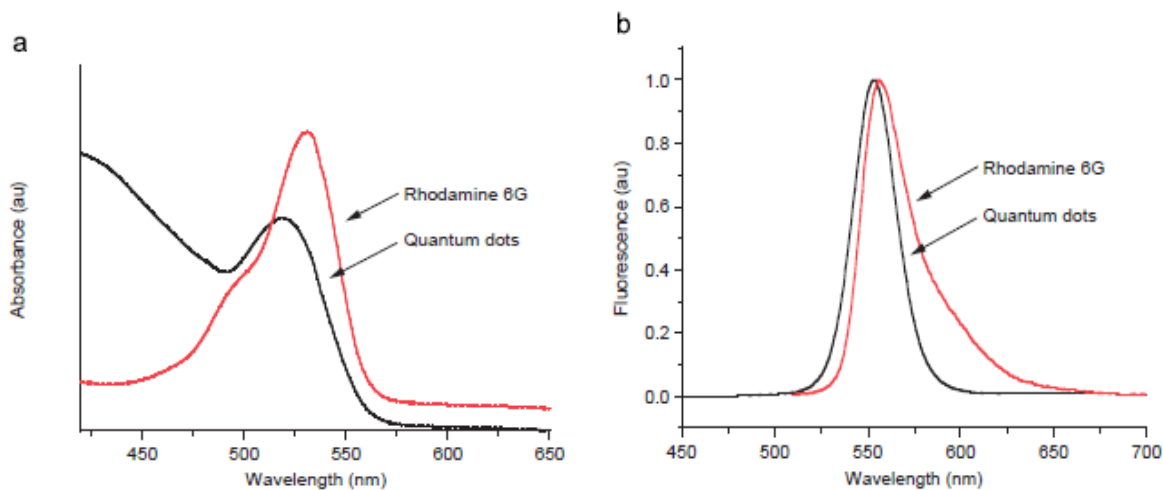


Figure 2.10: Comparison of the excitation (a) and emission (b) spectra for a fluorescent dye (Rhodamine 6G) and quantum dots (CdSe) [158].

Moreover, semiconductor nanoparticles have been reported to be 20 times brighter and 100 times more stable than organic dyes. This is prompted by their high extinction coefficients and their ability to resist or withstand photo-bleaching. Conventional dyes are known to bleach when exposed to light for a few minutes, whereas quantum dots are able to undergo repeated cycles of excitation and fluorescence for long hours. This feature has made it possible to perform real time tracking of molecules or cells over an extended period of time [160 – 162].

2.5 Solubility of Semiconductor Nanoparticles

As mentioned earlier, semiconductor nanoparticles have attracted attention from various study fields, each requiring quantum dots at a specific form. To date, a myriad of applications in which these nanomaterials are being used as enhancing or replacement agents are in the field of biology. Such applications require high quality nanomaterials, but most importantly they must be soluble in aqueous media and must be active in bio-conjugate reactions [163 -

165]. In most cases, semiconductor nanoparticles are synthesized using the organometallic route which yields high quality, monodisperse nanostructures which are protected with hydrophobic coordinating ligands. These ligands are insoluble in aqueous media and therefore impart such characteristics over to resultant quantum dots, as they create a layer around these nanomaterials [166].

This restricts the use of these nanomaterials in biological assays, and are therefore required to undergo further processing to render them soluble in aqueous media, and more biocompatible. The methods used to solubilize nanoparticles can be grouped into two main categories, i.e. complete ligand exchange and native surface modification [167]. Complete ligand exchange involves the displacement of native hydrophobic ligands from the surface of nanoparticles, and replacing them with hydrophilic moieties such as thiols. The surface modification methods retain the native hydrophobic ligands, but now an amphiphilic molecule is introduced, which binds strongly to the hydrophobic alkyl chains with one end and exposes a hydrophilic end to the aqueous solvent [168 – 172].

2.6 Biofunctionalization

For use in biological applications such as imaging, detection and drug delivery, nanomaterials need to be tagged with or attached to biological molecules such as proteins, peptides, antibodies and nucleic acids that are capable of recognizing target analytes in biological samples. This process is called bio-functionalization or bio-conjugation, and should be conducted under mild conditions without disrupting the properties or functionality of these biological molecules [173 - 176].

The mechanism employed when attaching biomolecules to nanoparticles depends on the properties of the biomolecule and the intended use of the functionalized nanoparticle. Initially, processing is required before bio-conjugation can take place so as to introduce functional moieties on the surface of the nanoparticles which will aid attachment of the biomolecules. This is due to the fact that the synthesis methods used to produce these nanoparticles often does not make them capable of attachment to biomolecules. Several mechanisms have been used to attach biomolecules on quantum dot surfaces, and can be

grouped into two main categories i.e. covalent and non-covalent attachment, and are explained further in subsequent sections [177 – 179].

2.6.1 Covalent Attachment

This is one of the simplest and effective methods for attaching biomolecules to nanoparticle surfaces. This method is a combination of various mechanisms that exploit the presence of activated functional moieties at the surface of nanoparticles. It involves the use of small molecule cross-linkers to attach biomolecules to nanoparticles surfaces [180]. These cross-linkers act as anchors between the nanoparticles surface and the biomolecule, where they attach to the functional groups present on the surfaces of both the nanoparticle and the biomolecule [181].

Cross-linkers are molecules that have reactive terminal ends capable of binding to specific functional groups on proteins or any other molecule to be tagged. Terminal ends found on most cross-linkers include -OH, -COOH, and -NH₂ [182]. Two different types of cross-linkers have been used, namely homo- and hetero-bifunctional cross-linkers. Homo-bifunctional cross-linkers are those that contain one or two identical reactive groups on their terminal ends, and are mostly used to cross-link proteins to other proteins, or to different molecules, or to stabilize quaternary structures, using a one-step process. Hetero-bifunctional cross-linkers contain two or more different reactive groups. These cross-linkers are mostly used in sequential bio-functionalization reactions [183].

Covalent binding mostly involves the use of the carbodiimide chemistry method, amine- and sulfhydryl reactive chemistry, aniline catalysed hydrazone reactions, and the reversible reactions between phenyl boronic acid and diols [184, 185]. Carbodiimide chemistry, the most frequently used method, employs cross-linkers such as 1-ethyl-3-(3-dimethylaminopropyl) carbodiimide (EDC), dicyclohexylcarbodiimide (DCC), and some functional carbodiimide derivatives [186].

Also known as EDC coupling, this method activates or transfers carboxylic acid groups onto the nanoparticle surface which readily bind amine groups on the biomolecules [187]. In this reaction, N-ethyl-N-[dimethylaminopropyl] carbodiimide (EDC) converts the carboxylic acid

into a reactive intermediate which is susceptible to attack by amines. Therefore no modification of the biomolecule or protein is required since amine groups are readily available on the surface of most proteins [188 - 190].

This method has been used extensively to conjugate quantum dots to biomaterials. Ag *et al* [191] successfully conjugated anti-HER2 antibodies to thioglycolic acid (TGA) capped CdTe/CdS quantum dots using the EDC/NHS coupling reactions. Initially, NHS was used to activate carboxyl groups on the quantum dot surface, which were then used to actively bind amines on the anti-HER2 antibody, thereby forming amide linkages. Similarly, Kloepfer *et al* [192] successfully attached an amino acid, adenine, to cadmium selenide (CdSe) quantum dots using an EDC/NHS coupling reaction. These adenine conjugated CdSe quantum dots were subsequently used to label gram positive bacteria [193].

2.6.2 Non-covalent Attachment

This process is loosely described as the spontaneous absorption of biomolecules onto the surface of nanoparticles. It is composed of methods or mechanisms that exploit inherent charges on the surface of quantum dots to facilitate bio-functionalization with biomolecules that are oppositely charged. Non-covalent attachment is based on electrostatic interactions or binding, Van Der Waals forces, π effects and the hydrophobic effects [194, 195]. Of these, electrostatic interactions have been the preferred and most widely used method for attaching biomolecules onto nanoparticles surfaces using the non-covalent approach. Electrostatic binding is in turn based on ionic and hydrophobic interactions between the nanoparticle surface and the biomolecule of interest [196, 197].

Ionic interactions have been used extensively and they are based on the reactivity or binding of materials with opposite charges. Usually, semiconductor nanoparticles are synthesized to contain a negative net charge for stability purposes. Proteins on the other hand have an abundance of positively charged groups due to the presence of positively charged amino acids and also their N-terminal. Therefore, ionic interactions occur between the positively charged groups on the protein and the negatively charged nanoparticle surface thereby forming a non-covalent bond between the nanoparticle and the protein [198 - 200].

This mode of attachment is hailed as an easy and quick method for bio-functionalization; however it has been seen to have major limitations. These include the inability to control the orientation of the biomolecule on the nanoparticle surface, possibility of the biomolecule being replaced by other unwanted biomolecules in biological samples as the bond between the nanoparticle surface and the attached biomolecule is not strong enough [201, 202]. Also, as the bond between the quantum dot surface and the biomolecule is facilitated by ionic strength and pH, subtle changes in these parameters might result in the detachment or loss of the biomolecule from the nanoparticle surface [203, 204].

2.7 Nanoparticle Toxicity

Nanomaterials have been shown to have unique properties and capabilities that can be useful in unlocking important biological insights, and also improve or enhance key processes in clinical diagnostics and therapeutic applications. However, their use has been restricted by their potential toxic effects which have become a major concern recently [205]. Biocompatibility of nanomaterials determines their suitability for use in such biological assays, as they can be detrimental to biological form [206]. This involves both the solubility of these nanomaterials in aqueous or biological media and their toxicity at cellular level (cytotoxicity). Since the emergence of these nanomaterials as highly efficient tools for biological analysis, nanoparticle toxicity has been a topic of interest sparked with numerous debates that have led to the establishment of a new platform termed “Nanotoxicology” [207, 208].

Toxicity of nanoparticles is dependant entirely on the physicochemical properties of these nanomaterials together with environmental factors; and as each individual type of nanomaterial contains its own unique properties, biocompatibility or toxicity is expected to vary amongst different types of nanoparticles [209]. These include the size, charge, concentration, outer coating bioactivity, and oxidative, photolytic, and mechanical stability [210 - 213]. The toxicity of nanomaterials has been investigated in numerous *in vitro* and *in vivo* assays which monitor cell growth, cell viability and DNA damage in response to treatment with nanoparticles. Due to the use of various methods or assays for the assessment of nanoparticle cytotoxicity, coupled with the use of different experimental conditions, there

are conflicting reports and discrepancies on the cytotoxic behaviour, bio-distribution and clearance of these nanomaterials. This makes it difficult to fully comprehend the fundamental mechanism by which nanoparticles induce toxicity both in vitro and in vivo [214 - 217].

It has been reported that nanoparticles induce cytotoxicity by compromising the integrity of the plasma membrane, mitochondrion and the nucleus. This therefore initiates the process of apoptosis which further results in cell death [218 - 220]. Figure 2.11 gives a detailed illustration of the proposed mechanisms by which nanomaterials induce cell death.

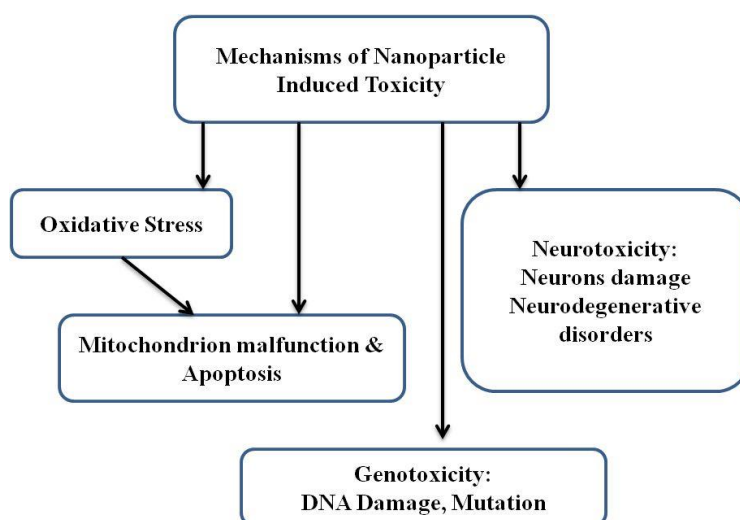


Figure 2.11: Various mechanisms through which quantum dots are likely to induce cytotoxicity [221].

Literature reports toxicity on the most commonly used nanomaterials, which are based on cadmium, selenium and zinc based nanoparticles [222]. These materials are known to be highly toxic and carcinogenic in their bulk form, and are therefore expected to be toxic in their nanoparticle state. The level at which nanoparticles are cytotoxic is reliant upon the size, type of capping ligand, and the exposure concentration [223]. It has been argued that most nanomaterials show toxicity through the release of free ions. For example, in the case of cadmium based nanoparticles, cytotoxicity is correlated with the release of free Cd^{2+} ions due to the weakening of the nanoparticle lattice or upon degradation, due to photosensitization [224].

This results in the disturbance of the oxidative balance of the cell, which further leads to the production of reactive oxygen species (ROS) such as superoxide (O_2^-), hydroxyl radicals (HO^\cdot), peroxide radicals (ROO^\cdot) and hydrogen peroxide (H_2O_2) [225 – 227]. Therefore, it has been reported that toxicity can be circumvented through the use of an appropriate coating ligand, which will bind strongly to the nanoparticle for an extended period of time and will not disintegrate. The capping ligand will thus form a protective layer around the nanoparticle which will limit the access of light and oxygen to the core surface and hence prevent oxidation [228 - 230].

2.8 Significance of Capping Ligands in Semiconductor Nanoparticle Synthesis

As mentioned previously, the synthesis method for semiconductor nanomaterials usually involves three components, i.e.; precursors, a capping ligand or surfactant and a solvent. In some cases, the solvent can also serve as a capping ligand. Capping ligands are known to play various roles during nanoparticle synthesis which include the control of nanoparticle growth, coating of dangling bonds at the surface of resulting nanoparticles, prevention of nanoparticle aggregation and determination of nanoparticle solubility [231]. Capped nanoparticles differ from their uncapped counterparts by their optical (absorption and emission spectra) and morphological properties. For example, uncapped or poorly capped nanoparticles are likely to contain electron and/or hole traps which will negatively affect its luminescence properties. In this study, four capping ligands were employed to improve solubility and toxicity of as-synthesized nanoparticles. These include L-glutathione (GSH), thioglycolic acid (TGA), crown ether (18-crown-6) and L-carnosine (L-Carn).

2.8.1 L-Glutathione

Glutathione is a tripeptide that is composed of three amino acids, i.e.; Glutamic acid, cysteine and glycine. It is a ubiquitous antioxidant that occurs abundantly in human and plant cells, where it prevents damage to important cellular components caused by reactive oxygen species such as free radicals and peroxides. As such, GSH is used as a supplement for patients suffering from cancer, sepsis and trauma where it regulates nitrogen balance which improves their survival rate [232, 233]. Also, this tripeptide is known to adsorb easily onto

surfaces of metal nanoparticles, hence it has been used extensively as a capping ligand in the synthesis of metal nanoparticles. This is because GSH contains a thiol, amine and carboxylate functionalities that enable coupling of the as-synthesized nanoparticles to other molecules for biological or sensing applications [234, 235]. The structure of GSH is presented in Figure 2.12A. Baruwati *et al.* [236] reported the effectiveness of GSH in the control of the size and shape of silver nanoparticles when used as capping ligand during synthesis.

2.8.2 Thioglycolic Acid

Thioglycolic acid is a small, water soluble, carboxylic acid that is chained to a sulfur group. Owing to its unique reducing capabilities, this ligand has been used as a chemical intermediate in various chemical reactions that involve addition, elimination and cyclization. TGA contains two functional groups, i.e.; thiol and carboxylic groups; the thiol group is known to be reactive in the presence of bases, acids, ketone groups and organic halogen compounds whereas the carboxylate group reacts in the presence of alcohols or amines, nonetheless preferentially. The chemical structure of TGA is represented in Figure 2.12B. TGA has been used extensively in the cosmetic industry as an active ingredient in hair treatment products and also in acrylic polymers as a water soluble chain transfer agent. TGA has found widespread use in nanoparticle synthesis where it has been employed as a capping ligand in the synthesis of various nanomaterials to improve nanoparticle toxicity. For example, Yang *et al.* [237] used TGA as a non-toxic template for the synthesis of metal sulfides via a mild hydrothermal route. During this process, TGA was reported to act as an oriented growth reactant [238].

2.8.3 18-Crown-6

18-crown-6 belongs to a family of compounds known as crown ethers. It is a microcyclic polyether with a structure that contains hydrogen, carbon and oxygen atoms as shown in Figure 2.12C. Each of the oxygen atoms is trapped between two carbon atoms thereby forming a confirmation with a hole or an open cavity. This compound contains donor atoms within their ring structure which can donate electrons to metal ions thereby encapsulating them. 18-crown-6 has the ability to form stable complexes with metal ions that have similar diameters with the open cavity of these ethers. This occurs through the ion dipole interaction

between positively charged metal ions and the negatively charged oxygen atoms which form the crown ether ring. It has been reported that macrocyclic ligands have the ability to form more stable complexes with metal ions compared to non-cyclic polydentate ligands. As such, crown ethers have been used extensively in the fabrication of sensors and separation systems [239 - 241]. Recently, 18-crown-6 has been used in the synthesis of nanomaterials due to their complexing abilities. This ligand has been found to act as both the reducing and the stabilizing agent during nanoparticle synthesis. Pal and colleagues successfully synthesized stable silver nanoparticles using 18-crown-6 as a reducing and stabilizing agent [242].

2.8.4 L-Carnosine

Carnosine, also known as beta-alanyl-L-histidine, is a naturally occurring dipeptide composed of two amino acids, namely β -alanine and L-histidine, bound together via a peptide linkage. It is found in various body organs including the stomach, kidney, skeletal and cardiac muscles and also the brain. Carnosine has been linked to numerous biological roles such as being a physiological buffer, promotion of wound healing, regulation of enzyme activity, ion chelating agent, inhibition of oxidative reactions and acting as an anti-glycating agent. Owing to its ability to form stable complexes with metal ions, L-carnosine has been reported to be an effective chelator of transition metals such as copper, iron, calcium and zinc, thereby preventing metal induced damage. L-carnosine contains several functional groups that act as binding sites for metal cations. These include the carboxylic group, amine group, amide group and the imidazole moiety of histidine, as shown in Figure 2.12D [243 - 245]. Owing to these aforementioned properties, this dipeptide has been used as a capping ligand during the synthesis of biocompatible nanoparticles. Malkar *et al.* [246] synthesized silver (Ag) nano-chains capped with carnosine using ionizing radiation. They reported that carnosine plays an important role in the stabilization and morphology of as-synthesized nanoparticles.

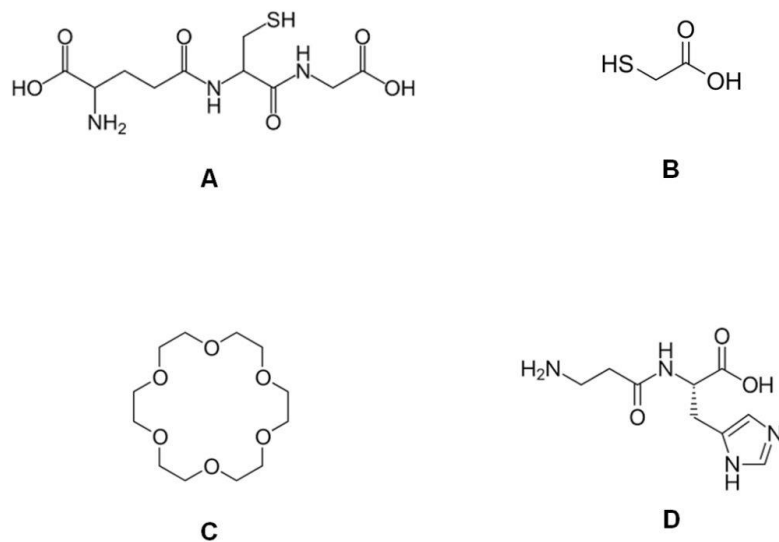


Figure 2.12: Chemical structures of GSH (A), TGA (B), 18C6 (C) and L-Carn (D) to be used as capping ligands [247, 248].

2.9 References

- [1]. S. K. Singh, P. P. Kulkarni, D. Dash. *Blackwell Publishing Ltd.*, **2013**
- [2]. M. C. Roco, R. S. Williams, P. Alivisatos. *Kluwer Academic Publishers.*, **2000**.
- [3]. S. K. Sahoo, S. Parveen, J. J. Panda. *Nanomedicine*, **2007**, 3, 120 – 31.
- [4]. O. M. Koo, I. Rubinstein, H. Onyuksel. *Nanomedicine*, **2005**, 1, 193 – 212.
- [5]. V. Biju, T. Itoh. A. Anas, A. Sujith and M. Ishikawa. *Anal Bioanal Chem.*, **2008**, 391, 2469 – 2495.
- [6]. S. Logothetidis. *J. Nanosci. Nanotechnol.*, **2012**, 1 – 22.
- [7]. E. L. Wolf. *Wiley-VCH Verlag GmbH*, **2006**, 10.1002/9783527618972.ch1
- [8]. C. Kumar. *Journal of Geoethical Nanotechnology*. **2008**, 3,
- [9]. A. L. Porter, J. Youtie. *J Nanopart Res.*, **2009**, 11, 1023 – 1041.
- [10]. C. Wang, X. Gao and X. Su. *Anal Bioanal Chem.*, **2010**, 397, 1397 – 1415.
- [11]. A. Valizadeh, H. Mikaeili, M. Samiei, S. M. Farkhani, N. Zarghami, M. Kouhi, A. Akbarzadeh and S. Davaran. *Nanoscale Res. Lett.*, **2012**, 7, 1 – 14.
- [12]. D. Vasudevan, R. R. Gaddam, A. Trinchi and I. Cole. *J. Alloys Compd.*, **2015**, 636, 395 - 404.
- [13]. O. E. Semonin, J. M. Luther, M. C. Beard. *Mater. Today.*, **2012**, 11, 508 – 515.
- [14]. J. Drbohlavova, V. Adam, R. Kizek, J. Hubalek. *Int. J. Mol. Sci.*, **2009**, 10, 656 – 673.
- [15]. S. Mahajan, M. Rani, R. B. Dubey, J. Mahajan. *IJLRST.*, **2013**, 2, 518 – 521.
- [16]. C. P. Collier, T. Vossmeier, J. R. Heath. *Annu. Rev. Phys. Chem.*, **1998**, 49, 371.
- [17]. D. Bera, L. Qian, T-K. Tseng, P. H. Holloway. *Materials*, **2010**, 3, 2260 – 345.
- [18]. S. Brkić. *EIJST*, **2016**, 5, 98 – 107.

- [19]. P. M. Fauchet. *Mater. Today*, **2005**, 8, 26 – 33.
- [20]. S. J. Lim, M. U. Zahid, P. Le, L. Ma, D. Entenberg, A. S. Harney, J. Condeelis, A. M. Smith. *Nat. Commun.*, **2015**, 1 – 10.
- [21]. O. I. Micic, H. M. Cheong, H. Fu, A. Zunger, J. R. Sprague, A. Mascarenhas, A. J. Nozik. *J. Phys. Chem. B.*, **1997**, 101, 4904 – 4912.
- [22]. A. M. Smith, S. Nie. *AccChem Res.*, **2010**, 43, 190 – 200.
- [23]. L. E. Brus. *J. Chem. Phys.*, **1984**, 4403 – 4409.
- [24]. M. G. Bawendi, M. L. Steigerwald, L. E. Brus. *Annu. Rev. Phys. Chem.*, **1990**, 41, 477–496.
- [25]. A. P. Alivisatos. *J. Phys. Chem.*, **1996**, 100, 13226 – 13239.
- [26]. A. P. Alivisatos, A.P. *Science.*, **1996**, 271, 933 – 937.
- [27]. P. Mishra, G. Vyas, M. S. Harsoliya, J. K. Pathan, D. Raghuvanshi, P. Sharma and A. Agrawal. *Int J Pharm Sci Rev Res.*, **2011**, 1, 42 – 46.
- [28]. F. Pinaud, X. Michalet, L. A. Bentolila, J. M. Tsay, S. Doose, J. J. Li, G. Iyer and S. Weiss. *Biomaterials.*, **2006**, 27, 1679 – 1687.
- [29]. A. I. L. Efros, A. L. Efros. *Sov.Phys. Semicond.*, **1982**, 16, 772.
- [30]. S. M. Reimann, M. Manninen. *Rev. Mod.Phys.*, **2002**, 74, 1283.
- [31]. N. Revaprasadu, S. N. Mlondo, *Pure Appl. Chem.*, **2006**, 78, 1691 – 1702.
- [32]. V. I. Klimov. *Los Alamos Science.*, **2003**, 28, 214 – 220.
- [33]. [http://www.sigmaaldrich.com/materials-science/nanomaterials/quantum dots](http://www.sigmaaldrich.com/materials-science/nanomaterials/quantum%20dots)
- [34]. T. J. Deerinck. *ToxicolPathol.*, **2008**, 36, 112 – 116.
- [35]. V. Biju, T. Itoh, A. Anas, A. Sujith&M. Ishikawa. *Anal Bioanal Chem.*, **2008**, 2469 – 2495.

- [36]. Y. H. Su, S-L. Tu, S-W.Tseng, Y-C.Chang, S-H.Chang, W-M.Zhang. *Nanoscale.*, **2010**, 2, 2639 – 2646.
- [37]. M. A. Hegazy, A. M. A. El-Hameed. *NRIAG-JAG.*, **2014**, 3, 82 – 87.
- [38]. B. Yu, C. Zhu, F. Gan. *J. Appl. Phys.*, **1997**, 82, 4532.
- [39]. K. E. Jasim. *Intech.*, **2015**, 303 – 331.
- [40]. A. J. Nozik, M. C. Beard, J. M. Luther, M. Law, R. J. Ellingson, J. C. Johnson. *Chem. Rev.*, **2010**, 110, 6873 – 6890.
- [41]. Y. Sun, S. E. Thompson, T. Nishida. *J. Appl. Phys.*, 2007, **101**, 104503 – 104525.
- [42]. F. W. Wise. *Acc. Chem. Res.*, **2000**, 33, 773 – 780.
- [43]. R. Rossetti, L. Brus. *J. Phys. Chem.*, **1982**, 86, 4470 – 4472.
- [44]. D. Bimberg, M. Grundmann, N. Ledentsov. *John Wiley, New York.* **1998**
- [45]. S. Suresh. *J. Nanosci.Nanotechnol.*,**2013**, 3, 62 – 74.
- [46]. A. I. L. Efros, M. Rosen. *Annu. Rev. Mater. Sci.*, **2000**, 475 – 521.
- [47]. R. D. Levine. *Cambridge University Press*, **2005**, 208.
- [48]. M. C. Bawendi, M. L. Steigerwald, L. E. Brus. *Annu. Rev. Phys. Chem.*, **1990**, 41, 477.
- [49]. Z. Yu,L. Tetard,L. Zhai, J. Thomas.*Energy Environ. Sci.*, **2015**,8, 702 – 730.
- [50]. M. J. Fernee, A. Watt, J. Warner, S. Cooper, N. Heckenberg, H. Rubinsztein-Dunlop. *Nanotechnology*, **2003**, 14.
- [51]. E. U. Rafailov, M. A. Cataluna, E. A. Avrutin. *WILEY-VCH Verlag GmbH & Co.* **2011**,
- [52]. P. Matagne, J-P. Leburton.*American Scientific Publishers*, **2003**, 2 – 66.
- [53]. S. K. Kailasa, K. H. Cheng and H. F. Wu *Materials*, **2013**, 6(12), 5763 – 5795.
- [54]. C. A. M. Bonilla, V. V. Kouznetsov. *InTech.***2016**
- [55]. A.I. Ekimov, A. A. Onushchenko. *JETPLett.*,**1981**, 34, 345 – 349.

- [56]. A. Valizadeh, H. Mikaeili, M. Samiei, S. M. Farkhani, N. Zarghami, M. Kouhi, A. Akbarzadeh, S. Davaran. *Nanoscale Res Lett.*, **2012**; 7, 480.
- [57]. R. F. Pease, S. Y. Chou. *Proceedings of the IEEE*, **2008**, 96, 248.
- [58]. X. Zhang, C. Sun, N. Fang. *J. Nanopart. Res.*, **2004**, 6, 125 – 130.
- [59]. J. Behari. *Indian J Exp Biol.*, **2010**, 48, 1008 – 1019.
- [60]. D. Hynek, K. Tmejova, V. Milosavljevic, A. Moulick, P. Kopel, V. Adam, R. Kizek. *Int. J. Electrochem. Sci.*, **2015**, 10, 1117 - 1127
- [61]. T. Pellegrino, L. Manna, S. Kudera, T. Liedl, D. Koktysh, A. L. Rogach, S. Keller, J. Radler, G. Natile and W. J. Parak, *Nano Lett.*, **2004**, 4, 703.
- [62]. L. Shao, Y. Gao, F. Yan. *Sensors (Basel)*, **2011**, 11, 11736 – 11751.
- [63]. B. O. Dabbousi, C. B. Murray, M. F. Rubner, M. G. Bawendi. *Chem. Mater.*, **1994**, 6, 216 – 219.
- [64]. S. Modani, M. Kharwade, M. Nijhawan. *Int J Curr Pharm Res.*, **2013**, 5, 55 – 59.
- [65]. M. L. Steigerwald, L. E. Brus. *Acc. Chem. Res.*, **1990**, 23, 183 – 188.
- [66]. S. M. Farkhani, A. Valizadeh. *IET Nanobiotechnol.*, **2014**, 8, 59 – 76.
- [67]. S. J. Rosenthal, J. McBride, S. J. Pennycook, L. C. Feldman. *Surf Sci Rep.*, **2007**, 62, 111–157.
- [68]. C. B. Murray, D. J. Norris, M. G. Bawendi. *J. Am. Chem. Soc.*, **1993**, 115, 8706.
- [69]. D. V. Talapin, J.S. Lee, M. V. Kovalenko, E. V. Shevchenko. *Chem. Rev.*, **2010**, 110, 389 – 458.
- [70]. J. Chomoucka, J. Drbohlavova, P. Businova, M. Ryvolova, V. Adam, R. Kizek, J. Hubalek. *32nd International Spring Seminar on Electronics Technology. New York: Ieee*, **2009**, 653 - 657.
- [71]. M. Green. *RSC Nanoscience & Nanotechnology*, **2014**, 33.

- [72]. M. McDowell, A. E. Wright, N. I. Hammer. *Materials*, **2010**, 3, 614 – 637.
- [73]. N. Gaponik, D. V. Talapin, A. L. Rogach, K. Hoppe, E. V. Shevchenko, A. Kornowski, A. Eychmuller, H. Weller. *J. Phys. Chem. B*, **2002**, 106, 7177 – 7185.
- [74]. W. C. Chan, S. M. Nie. *Science*, **1998**, 281, 2016.
- [75]. X. Peng. *Chem. Eur. J.*, **2002**, 8, 334 – 339.
- [76]. J. A. Dahl, B. L. S. Maddux, J. E. Hutchison. *Chem. Rev.*, **2007**, 107, 2228 – 2269.
- [77]. H. Zhang, D. Wang, B. Yang, B. H. Möhwald. *J. Am. Chem. Soc.*, **2006**, 128, 10171 – 10180.
- [78]. A. L. Rogach, T. Franzl, T. A. Klar, J. Feldmann, N. Gaponik, V. Lesnyak, A. Shavel, A. Eychmuller, Y. P. Rakovich, J. F. Donegan. *J. Phys. Chem. C.*, **2007**, 111, 14628 – 14637.
- [79]. Y. Zhang, A. Clapp. *Sensors*, **2011**, 11, 11036 – 11055.
- [80]. M. Green. *J. Mater. Chem.*, **2010**, 20, 5797 – 5809.
- [81]. J. Chomouck, J. Drbohlavova, M. Ryvolova, P. Sobrova, Libor Janu, V. Adam, J. Hubalek, R. Kizek. *Nova Science Publishers, Inc.* **2008**, 1 – 28.
- [82]. L. Liu, Q. Peng, Y. Li. *Inorg Chem.*, **2008**, 47, 5022 – 5028.
- [83]. Y. S. Park, A. Dmytruk, I. Dmitruk, A. Kasuya, M. Takeda, N. Ohuchi, Y. Okamoto, N. Kaji, M. Tokeshi, Y. Baba. *ACS Nano*, **2010**, 4, 121 – 128.
- [84]. J. Li, X. Hong, D. Li, K. Zhao, L. Wang, H. Wang, Z. Du, J. Li, Y. Bai, T. Li. *Chem. Commun.*, **2004**, 1740 – 1741.
- [85]. H. Zhu, M. Z. Hu, L. Shao, K. Yu, R. Dabestani, M. B. Zaman, S. Liao. *J. Nanomater.*, **2014**, 2014, 1 – 14.
- [86]. V. V. Breus, C. D. Heyes, G. U. Nienhaus. *J. Phys. Chem. C.*, **2007**, 111, 18589 – 18594.
- [87]. M. Z. Hu, T. Zhu. *Nanoscale Res Lett.*, **2015**, 10, 1 – 15.

- [88]. W. Schumacher, A. Nagy, W. J. Waldman, P. K. Dutta. *J. Phys. Chem. C.*, **2009**, 113, 12132 – 12139.
- [89]. S. Jin, Y. Hu, Z. Gu, L. Liu, H. Wu. *J Nanomater.*, **2011**, 2011, 1 – 13.
- [90]. S. Mahajan, M. Rani, R. B. Dubey, J. Mahajan. *IJLRST*, **2013**, 2, 518 – 521.
- [91]. A. Shrestha, N. A. Spooner, S. Z. Qiao, S. Dai. *Phys. Chem. Chem. Phys.*, **2016**, 18, 14055 – 14062.
- [92]. J. Baumgartner, A. Dey, P. H. H. Bomans, C. Le Coadou, P. Fratzl, N. A. J. M. Sommerdijk, D. Faivre. *Nat. Mater.*, **2013**, 12, 310 – 314.
- [93]. C. de Mello Donega', P. Liljeroth, D. Vanmaekelbergh. *Small*, **2005**, 1, 1152 – 1162.
- [94]. Y. Kousaka, T. Nomura, M. Alonso. *Advanced Powder Technol.*, **2001**, 12, 291 – 309.
- [95]. N. T. K. Thanh, N. Maclean, S. Mahiddine. *Chem. Rev.*, **2014**, 114, 7610 – 7630.
- [96]. P. G. Vekilov. *Nanoscale*, **2010**, 2, 2346 – 2357.
- [97]. F. Barroso, M. de Dios, C. Tojo, M. C. Blanco, M. A. López-Quintela. *Colloids Surf A Physicochem Eng Asp.*, **2005**, 270, 78 – 82.
- [98]. C. Tojo, F. Barroso, M. de Dios. *J. Colloid Interface Sci.*, **2006**, 296, 591 – 598.
- [99]. R. P. Sear. *J. Phys. Chem. B.*, **2006**, 110, 4985 – 4989.
- [100]. V. Uskoković. *Rev. J. Chem.*, **2013**, 1; 3, 271 – 303.
- [101]. P. G. Koutsoukos, A. N. Kofina, D. G. Kanellopoulou. *Pure Appl. Chem.*, **2007**, 79, 825 – 850.
- [102]. P. Cubillas, M. W. Anderson. *Wiley-VCH Verlag GmbH & Co.*, **2010**, 1, 1 – 55.
- [103]. J. Polte. *Cryst. Eng. Comm.*, **2015**, 17, 6809 – 6830.
- [104]. D. W. Oxtoby. *J. Phys. Condens. Matter.*, **1992**, 4, 7627.
- [105]. V. K. LaMer, R. H. Dinegar, *J. Am. Chem. Soc.*, **1950**, 72, 4847.

- [106]. V. K. LaMer, M. D. Barnes. *J. Colloid. Sci.*, **1946**, 1, 71 – 77.
- [107]. X. Peng, J. Wickham, A. P. Alivisatos, *J. Am. Chem. Soc.*, **1998**, 120, 5343.
- [108]. J. Park, J. Joo, S. G. Kwon, Y. Jang, T. Hyeon. *Angew. Chem. Int. Ed.*, **2007**, 46, 4630 – 4660.
- [109]. T. D. Nguyen, T. O. Do. *InTech.*, **2011**, 55 – 85.
- [110]. S. Arshadi, J. Moghaddam, M. Eskandarian. *Korean J. Chem. Eng.*, **2014**, 31, 2020 – 2026.
- [111]. S. Jana. *Dalton Trans.*, **2015**, 44, 18692 – 18717.
- [112]. R. Viswanatha, D. D. Sarma. *Nanomaterials Chemistry*, **2007**, 139 – 170.
- [113]. D. Elwell, H. J. Scheel. *Academic Press.*, **1975**.
- [114]. A. C. Lasaga. *Princeton University Press*, **1998**, 811.
- [115]. I. M. Lifshitz, V. V. Slyozov. *J. Phys. Chem. Solids.*, **1961**, 19, 35 – 50.
- [116]. C. Wagner. *J. Z. Elektrochem.*, **1961**, 65, 581 - 591.
- [117]. W. Z. Ostwald. *Phys. Chem.*, **1900**, 34, 495.
- [118]. G. Oskam, Z. S. Hu, R. L. Penn, N. Pesika, P. C. Searson. *Phys. Rev. E: Stat. Nonlinear. Soft Matter Phys.* **2002**, 66.
- [119]. M. de Dios, F. Barroso, C. Tojo, M.A. López-Quintela. *J. Colloid Interface Sci.*, **2009**, 333, 741 – 748.
- [120]. S. Vedantam, V. V. Ranade. *Sadhana.*, **2013**, 38, 1287 – 1337.
- [121]. Q. Zhang, S. J. Liu, S. H. Yu. *J. Mater. Chem.*, **2009**, 19, 191 – 207.
- [122]. B. Bian, W. Xia, J. Du, J. Zhang, J. P. Liu, Z. Guo and A. Yana. *Nanoscale*, **2013**, 5, 2454
- [123]. W. Qin-bo, R. Finsy, X. Hai-bo, L. Xi. *J Zhejiang Univ SCI.*, **2005**, 6, 705 – 707.

- [124]. A. Baldan.*J.Mater. Sci.*, **2002**, 37, 2171 – 2202.
- [125]. I. M. Lifshitz, V. V. Slyozov.*J. Phys. Chem. Solids.*, **1961**, 19, 35 – 50.
- [126]. C. Wagner.*J. Z. Elektrochem.*, **1961**, 65, 581 - 591.
- [127]. Y. Liu, K. Kathan, W. Saad, R. K. Prud'homme.*Phys. Rev. Lett.*, **2007**, 98, 1 – 4.
- [128]. H. Pang, C. Wei, X. Li, G. Li, Y. Ma, S. Li, J. Chen, J. Zhang. *Sci Rep.*, **2014**, 4, 3577 – 3585.
- [129]. C. H. Lai, M. Y. Lu, L. J. Chen.*J.Mater. Chem.*, **2012**, 22, 19 – 30.
- [130]. M-R.Gao, Y-F.Xu, J. Jiang, S-H.Yu.*Chem. Soc. Rev.*, **2013**, 42, 2986 – 3017.
- [131]. F. Chen, H. Hong, S. Goel, S. A. Graves, H. Orbay, E. B. Ehlerding, S. Shi, C. P. Theuer, R. J. Nickles and W. Cai. *ACS Nano.*, **2015**, 9, 3926 – 3934.
- [132]. Y. Xie, A. Riedinger, M. Prato, A. Casu, A. Genovese, P. Guardia, S. Sottini, C. Sangregorio, K. Miszta, S. Ghosh, T. Pellegrino, L. Manna. *J. Am. Chem. Soc.*, **2013**, 135, 17630 – 17637.
- [133].H. Y. Wang, X. W. Hua, F. G. Wu, B. Li, P. Liu, N. Gu, Z. Wang and Z. Chen. *Appl Mater Interfaces.*,**2015**, 7, 7082 – 7092.
- [134]. M. Kruszynska, H. Borchert, A. Bachmatiuk, M. H. Rummeli, B. Buchner, J. Parisi and J. Kolny-Olesiak. *ACS Nano*, **2012**, 6, 5889 – 5896.
- [135]. W. Han, L. Yi, N. Zhao, A. Tang, M. Gao and Z. Tang. *J. Am. Chem. Soc.*, **2008**, 130, 13152 – 13161.
- [136]. P. V. Quintana-Ramirez, M. C. Arenas-Arrocena, J. Santos-Cruz, M. Vega-González, O. Martínez-Alvarez, V. M. Castaño-Meneses, L. S. Acosta-Torres and J. de la Fuente-Hernández. *Beilstein J Nanotechnol.*, **2014**, 5, 1542 – 1552.
- [137]. H. Zhang, Y. Zhang, J. Yu, and D. Yang.*J. Phys. Chem. C.*, **2008**, 112, 13390 – 13394.
- [138]. X. Rui, H. Tan and Q. Yan.*Nanoscale*, **2014**, 6, 9889 – 9924.

- [139]. W. P. Lim, C. T. Wong, S. L. Ang, H. Y. Low and W. S. Chin.*Chem.Mater.*,**2006**, 18, 6170 – 6177.
- [140]. W. Lou, M. Chen, X. Wang and W Liu.*J. Phys. Chem. C.*, **2007**, 111, 9658 – 9663.
- [141]. Y. Zhu, J. Peng, L. Jiang and J. Zhu.*Analyst*, **2014**, 139, 649 – 655.
- [142]. J. Kundu, D. Pradhan.*Appl.Mater. Interfaces*, **2014**, 6, 1823 – 1834.
- [143]. H. Bi, X. Jiang, C. Yang.*Mater.Lett. J. Electrochem. Society*, **2002**, 149, 1212 – 1217.
- [144]. I. Chakraborty, P. K. Malik, S. P. Moulik.*J. Nanopart. Res.*, **2006**, 8, 889 – 897.
- [145]. K. Krishnamoorthy, G. K. Veerasubramani, S. J. Kim.*Mater. Sci. Semicond. Process*, **2015**, 40, 781 – 786.
- [146]. K. Ramasamy, W. Maneerprakorn, M. A. Malik, P. O'brien.*Phil. Trans. R. Soc. A*, **2010**, 368, 4249 – 4260.
- [147]. S-J.Bao, Y. Li, C. Ming Li, Q. Bao, Q. Lu, J. Guo. *Crystal Growth & Design.*, **2008**, 8, 3745 – 3749.
- [148]. S. Aripnammal, T. Srinivasan.*Res. J. Recent. Sci.*, **2013**, 2, 102 - 105.
- [149]. A. M. Ibarra-Ruiz, D. C. R. Burbano, J. A. Capobianco.*Adv. Phys.*, **2016**, 1, 194 – 225.
- [150]. G. D. Chen, D. Stefano, R. Nechache, R. Rosei, F. Rosei, D. L. Ma.*Chem.Commun.*, **2001**, 6308 – 6310.
- [151]. J. Duan, H. Zhang, Q. Tang, B.He, L. Yu.*J.Mater. Chem. A.*, **2015**, 3, 17497 – 17510.
- [152]. S. J. Rosenthal, J. C. Chang, O. Kovtun, J. R. McBride, I. D. Tomlinson. *Chem Biol.*, **2011**, 18, 10 - 24.
- [153]. L. Zhang, F. X. Gu, J. M. Chan, A. Z. Wang, R. S. Langer, O. C. Farokhzad. *ClinPharmacolTher.*,**2007**, 83, 761 – 769.
- [154]. I. L. Medintz,H. Mattoussi,A. R. Clapp.*Int J Nanomedicine.*, **2008**, 3, 151 - 167.
- [155]. E. C. Jensen.*Wiley Periodicals Inc*, **2012**, 2031 – 2036.

- [156]. F. Wang, W. B. Tan, Y. Zhang, X. P. Fan, M. Q. Wang. *Nanotechnology*, **2006**, 17, 1 – 13.
- [157]. M. Y. Han, X. H. Gao, J. Z. Su, S. Nie. *Nat Biotechnol.*, **2001**, 19, 631 – 635.
- [158]. M. A. Walling, J. A. Novak and J. R. E. Shepard. *Int. J. Mol. Sci.* **2009**, 10(2), 441-491
- [159]. X. H. Gao, S. M. Nie. *Anal Chem.*, **2004**, 76, 2406 – 2410.
- [160]. U. Resch-Genger, M. Grabolle, S. Cavaliere-Jaricot, R. Nitschke, T. Nann. *Nat Methods.*, **2008**, 5, 763 – 775.
- [161]. T. Jamieson, R. Bakhshi, D. Petrova, R. Pocock, M. Imani, A. M. Seifalian. *Biomaterials*, **2007**, 28, 4717 – 4732.
- [162]. X. Wu, H. Liu, J. Liu, K. N. Haley, J. A. Treadway, J. P. Larson, N. Ge, F. Peale, M. P. Bruchez. *Nat. Biotechnol.*, **2002**, 21, 41 - 46.
- [163]. H. Kobayashi, M. R. Longmire, P. L. Choyke. *Adv Drug Deliv Rev.*, **2013**, 65, 1112 – 1119.
- [164]. S. Mazumder, R. Dey, M. K. Mitra, S. Mukherjee, G. C. Das. *J Nanomater.*, **2009**, 2009, 1 – 17.
- [165]. J. R. Lakowicz. *Kluwer Academic/Plenum Publishers*, 2nd Ed, **1999**,
- [166]. R. A. Brooks, F. Moyny, P. Gillis. *Magn. Reson. Med.*, **2001**, 45, 1014 – 1020.
- [167]. A. M. Smith, S. Dave, S. Nie, L. True, X. Gao. *Expert Rev. Mol. Diagn.*, **2006**, 6, 231 – 244.
- [168]. S. K. Shukla. *Adv. Mater. Rev.*, **2014**, 1, 2 – 12.
- [169]. H. T. Uyeda, I. L. Medintz, J. K. Jaiswal, S. M. Simon, H. Mattoussi. *J Am Chem Soc.*, **2005**, 127, 3870 - 3878.
- [170]. B. Dubertret, P. Skourides, D. J. Norris, V. Noireaux, A. H. Brivanlou, A. Libchaber. *Science*, **2002**, 298, 1759 - 1762.

- [171]. T. Pellegrino, L. Manna, S. Kudera, T. Liedl, D. Koktysh, A. L. Rogach, S. Keller, J. Radler, G. Natile, W. J. Parak. *Nano Lett.*, **2004**, 4, 703 – 707.
- [172]. C. J. Lin, R. A. Sperling, J. K. Li, T. Yang, P. Li, M. Zanella, W. H. Chang, W. J. Parak. *Small*, **2008**, 4, 334 – 341.
- [173]. A. S. Karakoti, R. Shukla, R. Shanker, S. Singh. *Adv. Colloid Interface Sci.*, **2015**, 215, 28 – 45.
- [174]. Y. Xing, J. Rao. *Cancer Biomark.*, **2008**, 4, 307 – 319.
- [175]. F. M. Veronese, Morpurgo, *Farmaco.*, **1999**, 54, 497 – 516.
- [176]. W. C. W. Chan, D. J. Maxwell, X. Gao, R. E. Bailey, M. Han, S. Nie. *Curr. Opin. Biotechnol.*, **2002**, 13, 40 – 46.
- [177]. C. M. Niemeyer. *Angew. Chem. Int. Ed.*, **2001**, 40, 4128.
- [178]. M. C. Daniel, D. Astruc. *Chem. Rev.*, **2004**, 104, 293 – 346.
- [179]. E. Katz, I. Willner. *Chem. Int. Ed.*, **2004**, 43, 6042.
- [180]. X. Wu, H. Liu, J. Liu, K. N. Haley, J. A. Treadway, J. P. Larson, N. Ge, F. Peale, M. P. Bruchez. *Nat. Biotech.*, **2003**, 21, 41 – 46.
- [181]. M. A. Walling, J. A. Novak, J. R. E. Shepard. *Int. J. Mol. Sci.*, **2009**, 10, 441 – 491.
- [182]. W. J. Parak, D. Gerion, T. Pellegrino, D. Zanchet, C. Micheel, S. C. Williams, R. Boudreau, M. A. Le Gros, C. A. Larabel, A. P. Alivisatos. *Nanotechnology.*, **2003**, 14, 15 – 27.
- [183]. I. Tessmer, P. Kaur, J. Lin, H. Wang. *JNanobiotechnology.*, **2013**, 11, 1 – 17.
- [184]. Y. Xing, Q. Chaudry, C. Shen, K. Y. Kong, H. E. Zhau, L. W. Chung, J. A. Petros, R. M. O'Regan, M. V. Yezhelyev, J. W. Simons, M. D. Wang, S. Nie. *Nat. Protoc.*, **2007**, 2, 1152 - 1165.
- [185]. M. Di Marco, S. Shamsuddin, K. A. Razak, A. A. Aziz, C. Devaux, E. Borghi, L. Levy, C. Sadun. *Int. J. Nanomedicine*, **2010**, 5, 37 – 49.

- [186]. H. M. E. Azzazy, M. M. H. Mansour, S. C. Kazmierczak. *Clin. Biochem.*, **2007**, 40, 917 – 927.
- [187]. C. A. G. N. Montalbetti, V. Falque. *Tetrahedron*, **2005**, 61, 10827 – 10852.
- [188]. Lin Z, Su X, Mu Y, Jin Q. *J. Nanosci. Nanotechnol.*, **2004**, 4, 641 - 645.
- [189]. R. Bilan, F. Fleury, I. Nabiev, A. Sukhanova. *Bioconjugate Chem.*, **2015**, 26, 609 – 624.
- [190]. X. Shi-Ge, X. Qi-Rong, Z. Qiang, Z. Yue, B. Su-Min, J. Yong, C. Xiao-Gang. *Chin J Anal Chem.*, **2013**, 41, 949 – 955.
- [191]. D. Ag, R. Bongartz, L. E. Dogan, M. Seleci, J-G. Walter, D. O. Demirkol. F. Stahl, S. Ozcelik, S. Timur, T. Scheper. *Colloids Surf., B.*, **2014**, 114, 96 – 103.
- [192]. J. A. Kloepfer, R. E. Mielke, J. L. Nadeau. *Appl. Environ. Microbiol.*, **2005**, 71, 2548 – 2557.
- [193]. M. H. Jazayeri, H. Amani, A. A. Pourfatollah, H. Pazoki-Toroudi, B. Sedighimoghaddam. *Sens Biosensing Res.*, **2016**, 9, 17 – 22.
- [194]. M. J. Bruchez, M. Moronne, P. Gin, S. Weiss, A. P. Alivisatos. *Science*, **1998**, 281, 2013 – 2016.
- [195]. R. G. Rayavarapu, W. Petersen, C. Ungureanu, J. N. Post, T. G. van Leeuwen, S. Manohar. *Int J Biomed Imaging.*, **2007**, 2007, 1 – 10.
- [196]. P. Zrazhevskiy, M. Sena, X. Gao. *Chem Soc Rev.*, **2010**, 39, 4326 – 4354.
- [197]. N. T. K. Thanh, L. A. W. Green. *Nano Today*, **2010**, 5, 213 – 230.
- [198]. J. Zhou, Y. Yang, C. Zhang. *Chem. Rev.*, **2015**, 115, 11669 – 11717.
- [199]. A. R. Clapp, I. L. Medintz, H. Mattoussi. *Chem Phys Chem.*, **2006**, 7, 47 - 57.
- [200]. S. B. Rizvi, S. Ghaderi, M. Keshtgar, A. M. Seifalian. *Nano Reviews*, **2010**, 1, 1 – 10.
- [201]. S. Kumar, J. Aaron, K. Sokolov. *Nat. Protoc.*, **2008**, 3, 2008, 314 – 320.
- [202]. A. P. Alivisatos, W. Gu, C. Larabell. *Annu Rev Biomed Eng.*, **2005**, 7, 55 – 76.

- [203]. A. Foubert, N. V. Beloglazova, A. Rajkovic, B. Sas, A. Madder, I. Y. Goryacheva, S. De Saeger. *Trends Anal. Chem.*, **2016**, 83, 31 – 48.
- [204]. D. A. Rothenfluh, H. Bermudez, C. P. O’Neil, J. A. Hubbell. *Nat Mater.*, **2008**, 7, 248 – 254.
- [205]. N. Chen, Y. He, Y. Su, X. Li, Q. Huang, H. Wang, X. Zhang, R. Tai, C. Fan. *Biomaterials*, **2012**, 33, 1238 – 1244.
- [206]. M. Bottrill, M. Green. *Chem. Commun.*, **2011**, 47, 7039 – 7050.
- [207]. O. Gladkovskaya, P. Greaney, Y. K. Gun’ko, G. M. O’Connor, M. Meere, Y. Rochev. *Toxicol. Res.*, **2015**, 4, 1409 – 1415.
- [208]. P. C. Ray, H. Yu, P. P. Fu. *J. Environ. Sci. Health C. Environ. Carcinog. Ecotoxicol. Rev.*, **2009**, 27, 1 – 35.
- [209]. R. Hardman. *Environ. Health Perspect.*, **2006**, 114, 165 – 172.
- [210]. K. M. Tsoi, Q. Dai, B. A. Alman, W. C. W. Chan. *Acc. Chem. Res.*, **2013**, 46, 672 – 680.
- [211]. F. Ahmad, A. K. Pandey, A. B. Herzog, J. B. Rose, C. P. Gerba, S. A. Hashsham. *J Nanopart Res.*, **2012**, 14, 1038 – 1063.
- [212]. Y. Wang, R. Hu, G. Lin, I. Roy, K-T. Yong. *ACS Appl. Mater. Interfaces.*, **2013**, 5, 2786 – 2799.
- [213]. J. Lovric, H. S. Bazzi, Y. Cuie, G. R. Fortin, F. M. Winnik, D. Maysinger. *J Mol Med (Berl)*, **2005**, 83, 377 - 385.
- [214]. I. Pujalté, I. Passagne, B. Brouillaud, M. Treguer, E. Durand, C. Ohayon-Courtes. *Part Fibre Toxicol.*, **2011**, 8.
- [215]. D. De Stefano, R. Carnuccio, M. C. Maiuri. *J. Drug. Deliv.*, **2012**, 2012, 1 – 14.
- [216]. A. Manke, L. Wang, Y. Rojanasakul. *BioMed Res. Int.*, **2013**, 2013, 1 – 15.
- [217]. Y. Ju-Nam, J. R. Lead. *Sci. Total Environ.*, **2008**, 400, 396 - 414.

- [218]. V. V. Breus, A. Pietuch, M. Tarantola, T. Basché, A. Janshoff. *Beilstein J. Nanotechnol.*, **2015**, 6, 281 – 292.
- [219]. E. Fröhlich. *Int J Nanomedicine*, **2012**, 7, 5577 – 5591.
- [220]. G. Lin, Q. Ouyang, R. Hu, Z. Ding, J. Tian, F. Yin, G. Xu, Q. Chen, X. Wang, K-T. Yong. *Nanomed. Nanotech. Biol. Med.*, **2015**, 11, 341 – 350.
- [221]. K-T. Yong, W-C. Law, R. Hu, L. Ye, L. Liu, M. T. Swihart, P. N. Prasad. *Chem. Soc. Rev.*, **2013**, 42, 1236 – 1250.
- [222]. N. Lewinski, V. Colvin, R. Drezek. *Small*, **2008**, 4, 26 – 49.
- [223]. E. Przybytkowski, M. Behrendt, D. Dubois, D. Maysinger. *FEBS J.*, **2009**, 276, 6204 – 6217.
- [224]. K. G. Li, J. T. Chen, S. S. Bai, X. Wen, S. Y. Song, Q. Yu, J. Li, Y. Q. Wang. *Toxicol. In Vitro*, **2009**, 23, 1007 – 1013.
- [225]. Y. Xing, J. Rao. *Cancer Biomark.*, **2008**, 4, 307 – 319.
- [226]. A. M. Derfus, W. C. W. Chan, S. N. Bhatia. *Nano Lett.*, **2004**, 4, 11 – 18.
- [227]. B. O. Dabbousi, J. Rodriguezviejo, F. V. Mikulec, J. R. Heine, H. Mattoussi, R. Ober, K. F. Jensen, M. G. Bawendi. *J. Phys. Chem. B.*, **1997**, 101, 9463 – 9475.
- [228]. S. W. Kim, J. P. Zimmer, S. Ohnishi, J. B. Tracy, J. V. Frangioni, M. G. Bawendi. *J. Am. Chem. Soc.*, **2005**, 127, 10526 – 10532.
- [229]. Q. H. Tran, V. Q. Nguyen, A. Le. *Adv. Nat. Sci.: Nanosci. Nanotechnol.*, **2013**, 4, 1 – 20.
- [230]. I. Kanelidis, T. Kraus. *Beilstein J. Nanotechnol.*, **2017**, 8, 2625 – 2639.
- [231]. M. Pongsuchart, C. Danladkaew, T. Khomvarn, A. Sereemasapun. *IPCBE*, **2012**, 27, 98 – 102.
- [232]. X. Ji, W. Wang, X. Li, Y. Chen, C. Ding. *Talanta*, **2016**, 150, 666 – 670.

- [233]. M. Murariu, I. Stoica, R. Gradinaru, G. Drochioiu, I. Mangalagiu. *Rev. Roum. Chim.*, **2014**, 59, 867 – 874.
- [234]. S. K. Balavandy, K. Shameli, D. R. B. A. Biak, Z. Z. Abidin. *Chemistry Central Journal.*, **2014**, 8, 1 – 10.
- [235]. B. Baruwati, V. Polshettiwar, R. S. Varma. *Green. Chem.*, **2009**, 11, 926 - 930.
- [236]. H. Zhang, X. Ma, Y. Ji, J. Xu, D. Yang, *Chem. Phys. Lett.*, 2003, 377, 654 – 657.
- [237]. M. Salavati-Niasari, M. R. Loghman-Estarki, F. Davar. *Chemical Engineering Journal* 2008, 145, 346 – 350.
- [238]. H. Kuanga, W. Chena, W. Yana, L. Xua, Y. Zhua, L. Liua, H. Chua, C. Penga, L. Wanga, N. A. Kotov, C. Xua. *Biosensors and Bioelectronics*, **2011**, 26, 2032 – 2037.
- [239]. R. M. Kakhki, M. Rakhshanipour. *Arabian Journal of Chemistry*, **2015**.
- [240]. M. Nogami, T. Haratani, Y. Tachibana, T. Kaneshiki, M. Nomura, T. Suzuki. *J. Radioanal. Nucl. Ch.*, **2015**, 303, 1549 – 1553.
- [241]. J. Pal, M. K. Deb, D. K. Deshmukh. *Appl. Nanosci.*, **2014**, 4, 507 – 510.
- [242]. E. M. Moustafa, M. Korany, N. A. Mohamed, T. Shoeib. *Inorganica Chimica Acta*, **2014**, 421, 123 – 135.
- [243]. F. Bellia, V. Oliveri, E. Rizzarelli, G. Vecchio. *European Journal of Medicinal Chemistry*, **2013**, 70, 225 – 232.
- [244]. Z. Durmus, H. Kavas, A. Baykal, H. Sozeri, L. Alpsoy, S. U. Celik, M. S. Toprak. *Journal of Alloys and Compounds*, **2011**, 509, 2555 – 2561.
- [245]. V. V. Malkar, T. Mukherjee, S. Kapoor. *Radiation Physics and Chemistry*, **2015**, 107, 54 – 58.
- [246]. F. O. Silva, M. S. Carvalho, R. Mendonça, W. A. A Macedo, K. Balzuweit, P. Reiss and M. A. Schiavon. *Nanoscale Res. Lett.* **2012**, 7(1), 536.

[247]. R. R. Hendrixson, M. P. Mack, R. A. Palmer, A. O. Ottolenghi and R. G. Ghirardelli. *Toxicol. Appl. Pharmacol.* **1978**, 44, 263 – 268.

[248]. V. V. Malkar, T. Mukherjee and S. Kapoor. *Radiat. Phys. Chem.*, **2015**, 107, 54 – 58.

Chapter 3: Experimental

3.1 Synthesis and Characterization of Metal Sulfide Nanoparticles

3.1.1 Chemicals and Reagents

Copper chloride dihydrate ($\text{CuCl}_2 \cdot 2\text{H}_2\text{O}$), cobaltous chloride hexahydrate ($\text{CoCl}_2 \cdot 6\text{H}_2\text{O}$), sodium diethyldithiocarbamate (SDEDTC), thioacetamide (TAA), glutathione (GSH), thioglycolic acid (TGA), 18-crown-6 (18C6), L-carnosine (L-Carn) and sodium hydroxide (NaOH) pellets were all obtained from Sigma Aldrich, and used without further purification.

3.1.2 Synthesis of Copper and Cobalt Sulfide Nanoparticles

Copper sulfide (Cu_xS_y) and cobalt sulfide (Co_xS_y) nanoparticles were synthesized using metal chlorides ($\text{CuCl}_2 \cdot 2\text{H}_2\text{O}$ or $\text{CoCl}_2 \cdot 6\text{H}_2\text{O}$) as metal sources, with SDEDTC and TAA employed as sulfur sources. GSH, TGA, 18C6 and L-Carn were used as capping agents. In a typical synthesis method, 2.36 mmol of the capping agent was prepared in 30 mL of deionized water (dH_2O) in a three-necked flask and stirred. A solution of the metal source (0.59 mmol) was then introduced into the flask, followed by a drop-wise addition of the sulfur source (1.8 mmol), with continuous stirring. The pH of the solution was adjusted to 9.0 by a drop-wise addition of 1 M NaOH then refluxed at a specified temperature (50 and 95 °C) for 60 minutes under nitrogen. Upon reaction completion, nanoparticles were collected via centrifugation and precipitates were washed thrice with dH_2O . Finally, some amount was dispersed in dH_2O for characterization purposes. The two temperatures, 50 and 95 °C, were chosen in order to investigate the growth of nanoparticles at both low and high temperatures.

3.1.3 Characterization Techniques

3.1.3.1 Optical Characterization

Optical absorption measurements were carried out using a Thermo Scientific Multi-Skan Go UV-visible spectrophotometer. Samples were placed in plastic cuvettes (1cm path length), using water as a reference solvent. Emission spectra measurements were recorded on a Perkin Elmer LS 45 photoluminescence (PL) spectrometer with a xenon lamp at room temperature. The samples were placed in glass cuvettes (1cm path length) using water as a reference solvent.

3.1.3.2 Electron Microscopy

Transmission Electron Microscopy (TEM) is a vital tool for viewing samples at higher resolutions. Since TEM uses electron beams to illuminate the sample instead of light, samples can be analysed at micrometre, nanometre, and even sub-nanometre scales. The technique (JEOL-JEM 2100F HR-TEM operated at 200 kV) was used to investigate the morphology (shapes and sizes) of as-synthesized nanoparticles. The samples were prepared by dropping a dilute dispersion of as-synthesised nanoparticles on carbon coated copper or nickel grids and allowed to dry at room temperature.

3.1.3.3 X-ray Diffraction

X-ray diffraction (XRD) analysis was performed on powdered samples using a Bruker XRD machine (D8 Advance, Copper X-ray source, Lynx-eye XE detector), carried out in the two theta (2θ) on a D8 diffractometer. Samples were placed in a glass holder and measurements were taken using a glancing angle of incidence detector at an angle of 2° , for 2θ values over $20^\circ - 60^\circ$ in steps of 0.05° with a scan speed of $0.01^\circ 2\theta. s^{-1}$.

3.1.3.4 Fourier Transform Infrared Spectroscopy

Infrared spectroscopy is a relevant technique in determining the binding mode of the ligand to the metal. More studies on infrared absorption spectra were reported for some metal sulfide nanoparticles. Infrared spectra were recorded on a Bruker Optics Tensor 27 Fourier Transform Infrared Spectroscopy. Spectra were collected over the range from 400 to 4000 cm^{-1} .

3.2 Cytotoxicity Studies of Copper and Cobalt Sulfide Nanoparticles

3.2.1 Chemicals and Reagents

Roswell Park Memorial Institute (RPMI) medium, Foetal calf serum (FCS), trypsin-EDTA, trypan blue, dimethyl sulfoxide (DMSO) were purchased from Sigma, South Africa. Cell Titer 96® AQueous One Solution Cell Proliferation Assay (MTS) kit and Cell Titer-Glo Luminescent Cell Viability Assay (ATP) kit were purchased from Promega Corporation (Madison, WI). MT-4 cells were purchased from ATCC (USA).

3.2.2 Cell Maintenance

Cells were maintained in 25 cm^2 tissue culture flasks in a humidified atmosphere containing 5% CO_2 at a temperature of 37°C. The cells were cultured in RPMI supplemented with 10% FCS and 0.2% Gentamycin-Streptomycin. Medium was changed every second day.

3.2.3 Trypan Blue Exclusion Assay

Cells were detached from flasks by use of trypsin-EDTA solution, centrifuged at 200 x g for 10 min, and then re-suspended in culture medium. An aliquot (10 μl) of the cell suspension was mixed with trypan blue (10 μl) in a small tube. An aliquot (10 μl) of the trypan blue-cell mixture was then applied onto a disposable cell counting chamber slide, which was then inserted in a countess automated cell counter (Invitrogen, SA) to count the number of viable cells.

3.2.4 Cytotoxicity Assay

Cytotoxicity of nanoparticles was studied by measuring the viability of MT-4 cells using the 3-[4,5-dimethylthiazol-2-yl]-2,5 diphenyl tetrazolium bromide (MTS) tetrazolium assay. MT-4 cells were grown in RPMI using standard cell culture conditions until 90% confluency. The cells were harvested *via* centrifugation at 400 x g for 5 minutes and the resulting pellet was re-suspended in DMEM. The cells were then seeded in 96 microwell plates at 2.5×10^5 cells/ml per well and incubated at standard cell culture conditions for 1 hour. Nanoparticle solutions (1mg/ml) were prepared and diluted in growth media to yield a concentration gradient. Nanoparticle dilutions (0.78125, 1.5625, 3.125, 6.25, 12.5, 25 and 50 $\mu\text{g/ml}$) were then added to the cells and incubated for 96 hours using standard cell culture conditions. The viability of treated cells was tested using the Cell Titer 96 Aqueous One Solution Cell Proliferation Assay kit. Briefly, 10 μl of an MTS solution was added to the treated cells and incubated for 2 hrs in standard cell culture conditions. The colorimetric change of the cells was quantified by reading its absorbance at 480 nm using an absorbance spectrophotometer. Experiments were repeated in order to validate the results.

3.3 Nanoparticle Bio-functionalization and Imaging

3.3.1 Chemicals and Reagents

Dulbecco's Modified Eagle Medium (DMEM), Foetal calf serum, trypsin/EDTA, PBS, doxorubicin, bovine serum albumin (BSA), Triton X-100, paraformaldehyde, *N*-(3-Dimethylaminopropyl)-*N'*-ethylcarbodiimide (EDC) and *N*-Hydroxysuccinimide (NHS) were purchased from Sigma, South Africa. Hypoxia inducible factor 1 α monoclonal antibody (HIF-1 α), Anti-phospho-Histone H2A.X monoclonal antibody (H2A.X), Goat anti-Rabbit IgG secondary antibody conjugated to Alexa Fluor 488 (IgG-Phospho) and mitotracker red dye were purchased from Thermo Fisher Scientific, South Africa. Human embryonic kidney cells (Hek-293) and HeLa cells were obtained from the American Type Culture Collection (ATCC).

3.3.2 Bio-conjugation or Probe development

Bioconjugation of antibodies to as-synthesized nanoparticles was carried out using carbodiimide chemistry which involves the activation of reactive terminal ends by EDC and NHS. Initially, nanoparticles were treated with EDC and NHS solutions to activate carboxylic groups on the surface of the nanoparticles before conjugation happened. Briefly, nanoparticles in solution were centrifuged, and the supernatant was decanted. The pellet was then suspended in a solution of EDC (100 ml; 20 mg/ml), followed by the addition of an NHS solution (100 ml; 10 mg/ml). The mixture was centrifuged at 10 000 rpm, for 10 minutes. The supernatant was then discarded and the resulting pellet was re-suspended in a solution containing 0.1 mg/ml monoclonal antibody. After shaking overnight at 4 °C, the solution was centrifuged and washed three times with PBS (10 mM, pH 7.4). After washing, the conjugates were re-suspended in PBS, and stored at 4 °C till use. The conjugates were characterized using UV-Vis spectroscopy.

3.3.3 Cell Imaging using Probes

Hek-293 and HeLa cells were cultured in T50 flasks using standard cell culturing techniques till 75 % confluency was achieved. The cells were then harvested, and seeded onto 6 well plates, and allowed to grow and reach 75 % confluency. Cells were then washed three times (3x) with PBS, stained with mitotracker red dye, and incubated at 37 °C for 30 minutes. After incubation, the cells were washed 3x with PBS, fixed with 4 % formaldehyde and incubated at 37 °C for 15 minutes. After washing, the cells were made permeable by treating with PBS containing 0.2 % Triton X-100 at 37 °C for 10 minutes. Following washing, the plates were blocked using PBS containing 1 % BSA, at room temperature for 30 minutes. The cells were then treated with the probes (antibody conjugates), and allowed to incubate at room temperature (RT) for 60 minutes. Control wells were treated with non-conjugated primary antibodies (anti-HIF-1 α and H2A.X). After washing, control cells were treated with secondary antibody (IgG-Phospho) and allowed to incubate at room temperature for 60 minutes. Cells were washed, and stored in PBS till viewing in a FLOID fluorescence microscope, using green and white light

Chapter 4: Results for Characterization of Copper Sulfide Nanoparticles

4.1 Introduction

Copper sulfide (Cu_xS_y) is a p-type semiconductor that exists in various crystalline phases such as covellite (CuS), anilite ($\text{Cu}_{1.75}\text{S}$), digenite ($\text{Cu}_{1.8}\text{S}$), djurlite ($\text{Cu}_{1.95}\text{S}$), and the copper rich chalcocite (Cu_2S). It is known to exhibit a stoichiometry-dependent band gap that can be tuned from 1.2 – 1.5 eV [1 - 3]. The most important feature of these semiconductors is based on the fact that their properties can be tuned or tailored by altering their structure, morphology, stoichiometric composition and valance state [4].

Copper based nanomaterials have recently gained popularity over other widely used metal based nanomaterials such as gold, silver and cadmium due to their abundance, low cost and also their inherent optical and electrical properties compared to their aforementioned counterparts [5, 6]. As such, copper sulfide nanomaterials have featured in a myriad of applications which utilize their photocatalytic, photovoltaic, thermoelectric, sensing, ion-storage, plasmonic, supercapacitor, and superionic abilities [7, 8].

Cu_xS_y nanomaterials have been widely used in energy based applications, and it is until recently that these nanomaterials are gaining popularity in biological applications. These have become the nanomaterials of choice in biomedical assays due to their excellent near-infrared (NIR) optical absorption which emanates from the d-d energy band transition of Cu^{2+} ions, high molecular co-efficient, and efficient heat generation capabilities [9, 10]. Recently, Cu_xS_y nanomaterials have gained popularity in biological assays such as sensing, molecular imaging, photothermal therapy, drug delivery. Moreover, these nanomaterials have now been applied as multifunctional agents that can assume both the imaging and therapeutic functional roles simultaneously [11].

In most cases, nanomaterials are synthesized using organometallic route which yields high quality nanostructures that are insoluble in aqueous media, thereby limiting their use in biological assays. Usually, nanomaterials synthesized via this route would undergo additional processing in the form of ligand exchange or encapsulation whereby the non-polar organic

capping agents used during organometallic synthesis are replaced or modified with polar inorganic ligands.

Following ligand exchange, the photoluminescence of these nanomaterials drops significantly [12, 13]. This then prompted the need to synthesize nanomaterials in polar solvents to yield stable, hydrophilic, and biocompatible QDs that can be used directly in biological assays without the need for ligand exchange. This method utilizes water soluble thiols as stabilizing agents or capping ligands for the synthesized nanoparticles [14 - 17]. In this chapter, the characterization of copper sulfide nanoparticles is reported. The as-synthesized water soluble nanoparticles can further be used directly in biological applications with no need of rendering them biocompatible.

4.2 Results and Discussions

Copper sulfide nanoparticles were synthesized using copper chloride as a copper source and sodium diethyldithiocarbamate (SDEDTC) or thioacetamide (TAA) as sulfur sources. To control the morphology of the particles and prevent particles from aggregation, four different capping agents, i.e.; glutathione (GSH), thioglycolic acid (TGA), 18-crown-6 (18C6) and L-carnosine (L-Carn) were used. Reactions were conducted at 50 and 95 °C, with water acting as a solvent.

4.2.1 Characterization of copper sulfide nanoparticles synthesized using SDEDTC as a sulfur source

4.2.1.1 Optical properties

Temperature and pH are some of the crucial parameters that influence the morphology of nanoparticles. An increase in temperature or pH will have an effect on the size and shape of nanoparticles, which extremely influences the absorption spectra of a particular nanomaterial. For instance, high temperatures favour the formation of larger nanoparticles, due to Ostwald ripening and oriented attachment effects [18, 19].

Figure 4.1 shows the absorption spectra of Cu_xS_y nanoparticles dispersed in water. The particles were synthesized at 50 (A) and 95 °C (B), with a reaction time of 1 hour (hr). All absorption spectra of Cu_xS_y nanoparticles synthesized at 50 °C depicted sharp maximum excitonic peaks in the visible region, appearing at 449, 452, 457 and 469 nm for GSH, TGA, 18C6 and L-Carn capped nanoparticles, with band edges recorded around 510 nm (2.43 eV), 512 nm (2.42 eV), 588 nm (2.11 eV) and 562 nm (2.21 eV) respectively. An emergence of broad bands in the near infrared region (NIR) was also observed around 700 nm for all spectra. All spectra are blue shifted when compared to that of bulk CuS material which has a band edge of 1022 nm. The shift to lower wavelength is attributed to quantum confinement of charge carriers in the nanoparticles [20]. The presence of two different peaks in each spectrum signifies the presence of both the chalcocite (Cu_2S) and covellite (CuS) phases. Cu_2S is known to exhibit an excitonic peak in the visible region (around 450 nm) while CuS is known to have an absorption band edge in the NIR region (around 700 nm) [21].

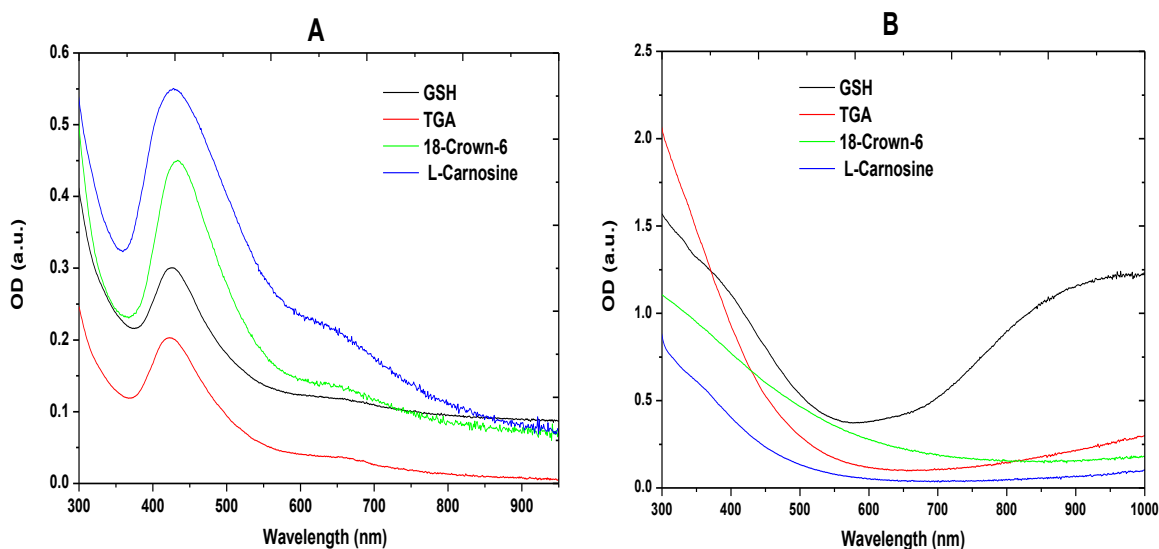


Figure 4.1: Absorption spectra of copper sulfide nanoparticles capped with GSH, TGA, 18C6 and L-Carn synthesized at 50 (A) and 95 °C (B) using SDEDTC as a sulfur source.

A change in the absorption spectra of Cu_xS_y nanoparticles was observed when synthesis is conducted at 95 °C (Figure 4.1B). The sharp peaks appearing between 400 and 550 nm in Cu_xS_y synthesized at 50 °C were not observed at 95 °C. GSH capped nanoparticles depicted an absorption spectrum typical of covellite CuS , with a sharp decrease from 300 to 550 nm

and a sharp increase from 600 to 900 nm. However, in the case of Cu_xS_y capped with TGA, 18C6 and L-Carn the above was not observed signifying that Cu_xS_y was not fully converted to covellite.

The emission properties of as-synthesized Cu_xS_y nanoparticles were investigated using photoluminescence spectroscopy (PL). The emission properties of semiconductor nanoparticles are mainly dependent upon their surface states, size distributions and surface passivation by the capping agent [22]. Figure 4.2 shows the PL spectra of Cu_xS_y nanoparticles capped with either GSH, TGA, 18-crown-6 or L-carnosine, synthesized at 50 (Figure 4.2A) or 95 °C (Figure 4.2B), using SDEDTC as a sulfur source. All PL spectra of nanoparticles synthesized both at 50 and 95 °C are red-shifted from their corresponding absorption spectra. This shift has been reported previously in literature for Cu_xS_y nanoparticles [23]. A slight shift to higher wavelength was observed in the PL spectra of nanoparticles synthesized at 95 °C as compared to those synthesized at 50 °C, i.e.; 590 to 593 nm, 588 to 591 nm, 588 to 596 nm and 590 to 594 nm for GSH, TGA, 18C6 and L-Carn capped Cu_xS_y nanoparticles respectively. All emission spectra have a single smooth peak which signifies that the surfaces of as-synthesized nanoparticles are well passivated by their respective capping ligands [24].

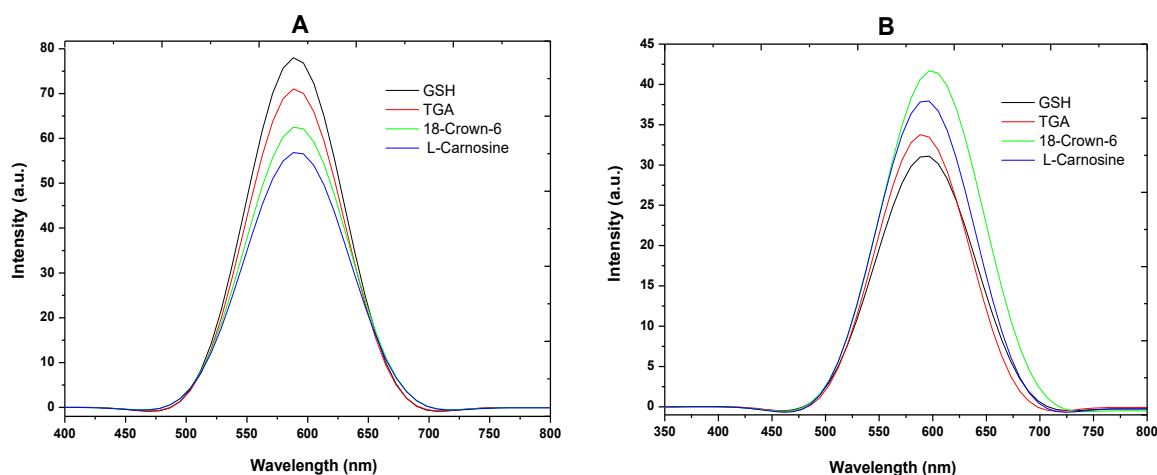


Figure 4.2: Emission spectra of copper sulfide nanoparticles capped with GSH, TGA, 18C6 and L-Carn synthesized at 50 (A) and 95 °C (B) using SDEDTC as a sulfur source.

4.2.1.2 Structural Properties

The structural properties of as-synthesized nanoparticles were investigated using Transmission Electron Microscopy (TEM) and X-ray Diffraction Spectroscopy (XRD). Figures 4.3 and 4.4 show TEM images of Cu_xS_y nanoparticles synthesized at 50 and 95 °C respectively. At 50 °C, spherical nanoparticles with average diameters of 2.1 nm, 3.5 nm and 12.5 nm were formed when GSH, TGA and 18-crown-6 were used as capping ligands, while clusters of near-spherical nanoparticles with an average diameter of 16.8 nm were formed when L-Carn was used.

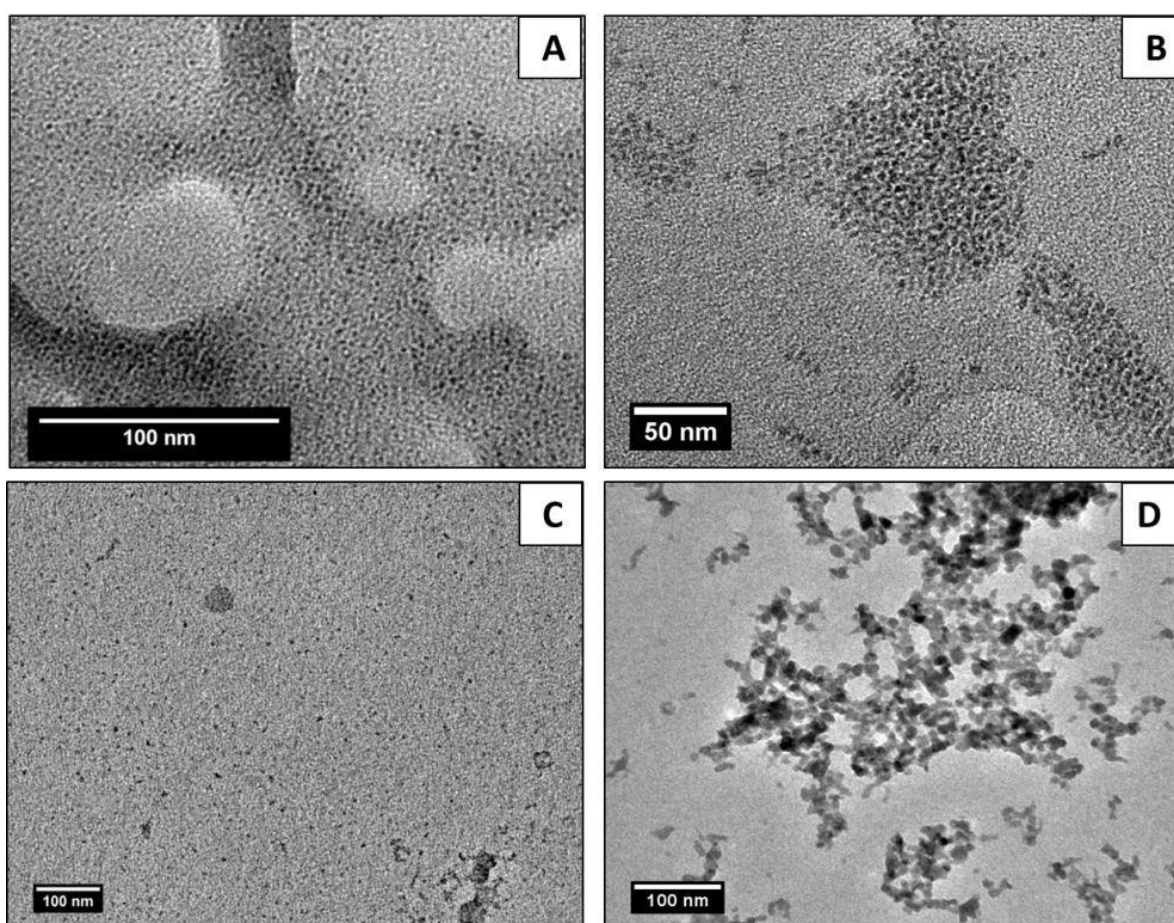


Figure 4.3: HR-TEM images of copper sulfide nanoparticles capped with GSH (A), TGA (B), 18C6 (C) and L-Carn (D) synthesized at 50 °C using SDEDTC as a sulfur source.

Upon increasing the temperature to 95 °C, a significant change in the morphology of Cu_xS_y nanoparticles was observed. An increase in size to 16.7 nm was observed when Cu_xS_y nanoparticles were capped with GSH (Figure 4.4A), and also evolved into hexagonal plates. TGA and L-carnosine capped nanoparticles grew bigger in sizes to 8.3 nm and 34.6 nm respectively, but their shapes were not affected. 18-crown-6 capped Cu_xS_y nanoparticles formed a mixture of near spherical, hexagonal and triangular plates with an average diameter of 18.7 nm. The effect of temperature on the formation of nanoparticles was reported previously by Cheng *et al.* [25] who observed a change in the morphological features of CuS nanoparticles capped with polyvinylpyrrolidone (PVP) when the reaction temperature was increased. The increase in the size of nanoparticles at higher synthesis temperatures is attributed to Ostwald ripening.

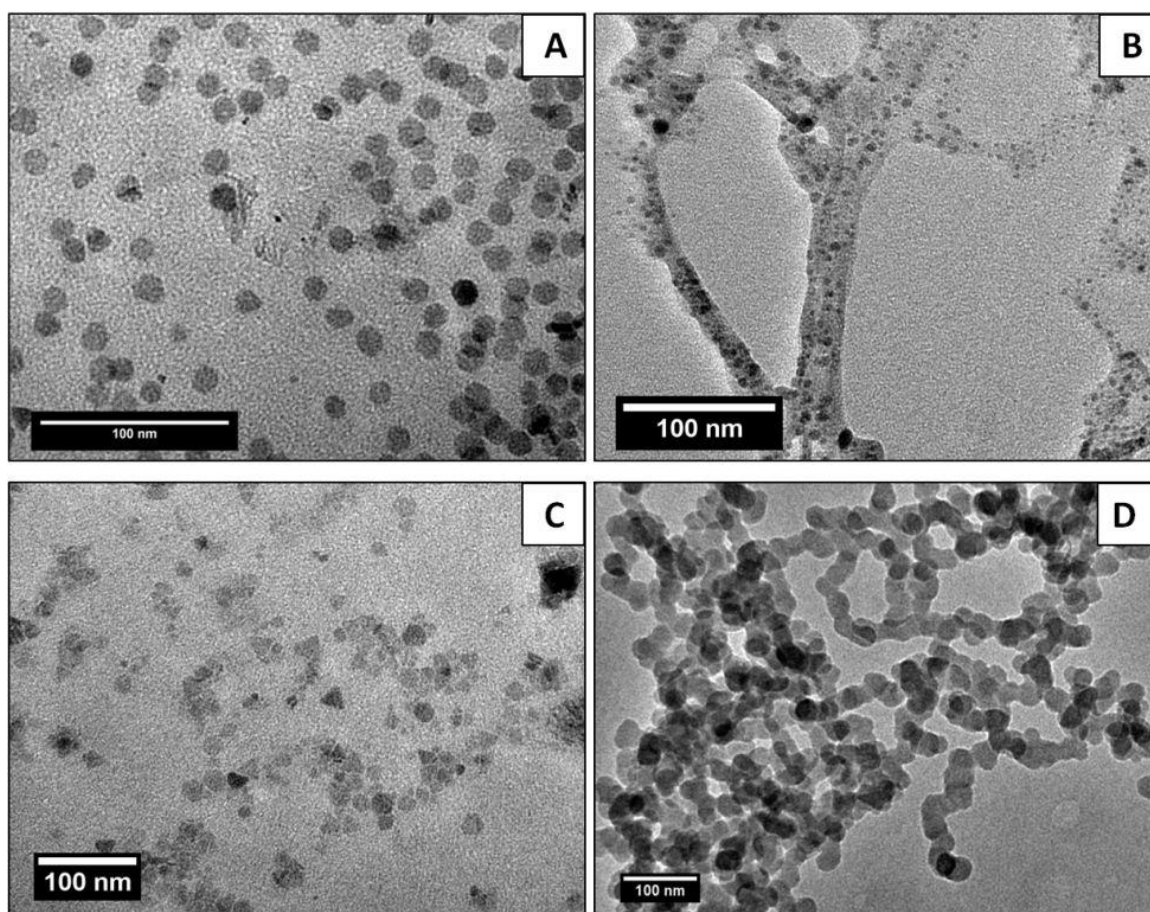


Figure 4.4: HR-TEM images of copper sulfide nanoparticles capped with GSH (A), TGA (B), 18C6 (C) and L-Carn (D) synthesized at 95 °C using SDEDTC as a sulfur source.

The crystallinity and phase structure of as-synthesized Cu_xS_y nanoparticles were examined by the X-ray diffraction technique. Figure 4.5 shows XRD patterns of Cu_xS_y nanoparticles synthesized at 50 °C. The as-synthesized Cu_xS_y nanoparticles formed two phases, namely covellite (CuS) and chalcocite (Cu_2S) phases. For the Cu_2S phase, diffraction peaks at 2θ values of 37.1° and 38.5° correspond to miller indices of (110) and (103) respectively (JCPDS, card number 4-784). For the CuS phase, the diffraction peaks at 2θ values of 32.2°, 34.5°, 39.9° and 45.5° correspond to miller indices (101), (102), (104) and (105) respectively CuS (JCPDS, card number 4-784). Signs of unmatched peaks were observed in all diffraction patterns of Cu_xS_y synthesized at 50 °C irrespective of the capping agent used.

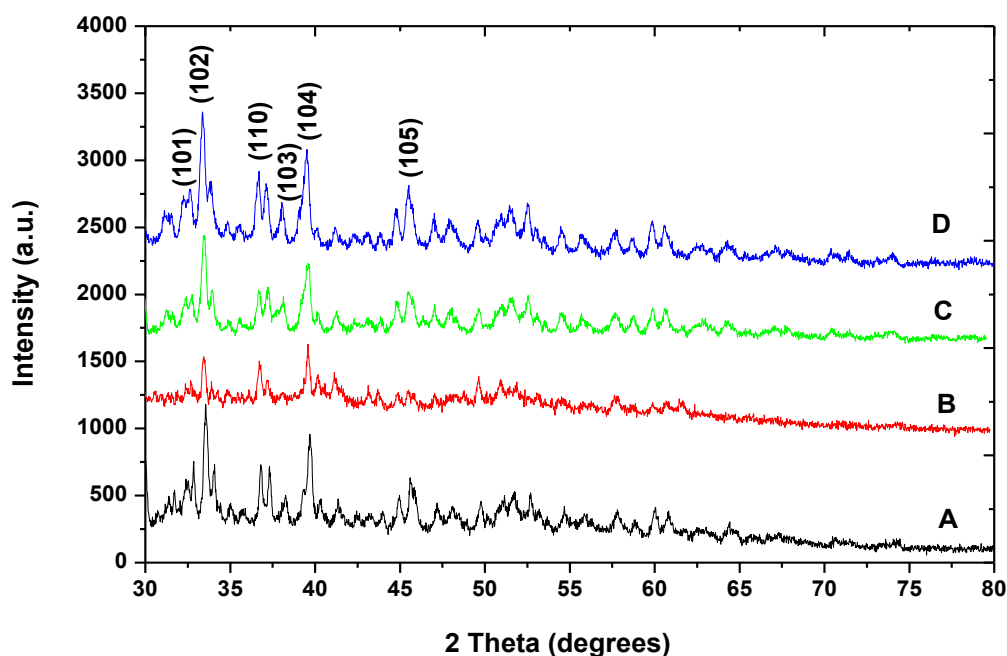


Figure 4.5: XRD patterns of copper sulfide nanoparticles capped with GSH (A), TGA (B), 18C6 (C) and L-Carn (D) synthesized at 50 °C using SDEDTC as a sulfur source.

No changes were observed in the diffraction patterns of Cu_xS_y nanoparticles capped with TGA (Figure 4.6B), 18C6 (Figure 4.6C) and L-Carn (Figure 4.6D) as compared to those synthesized at 50 °C. However, only one phase was observed in the case of Cu_xS_y capped with GSH at 95 °C (Figure 4.6A). This strongly indicates that the formation of Cu_2S in either 50 or 95 °C was independent of the capping agent employed during the synthesis reaction.

The diffraction peaks appearing at 2θ values of 34.4° , 37.5° , 38.6° , 45.7° , 56.3° , 56.7° and 58.4° correspond to miller indices of (102), (006), (103), (105), (107), (110) and (112) of covellite CuS (JCPDS, card number 4-784) [26 - 29]. No diffraction peaks due to impurities (CuO) were observed. This indicates that pure covellite CuS was formed.

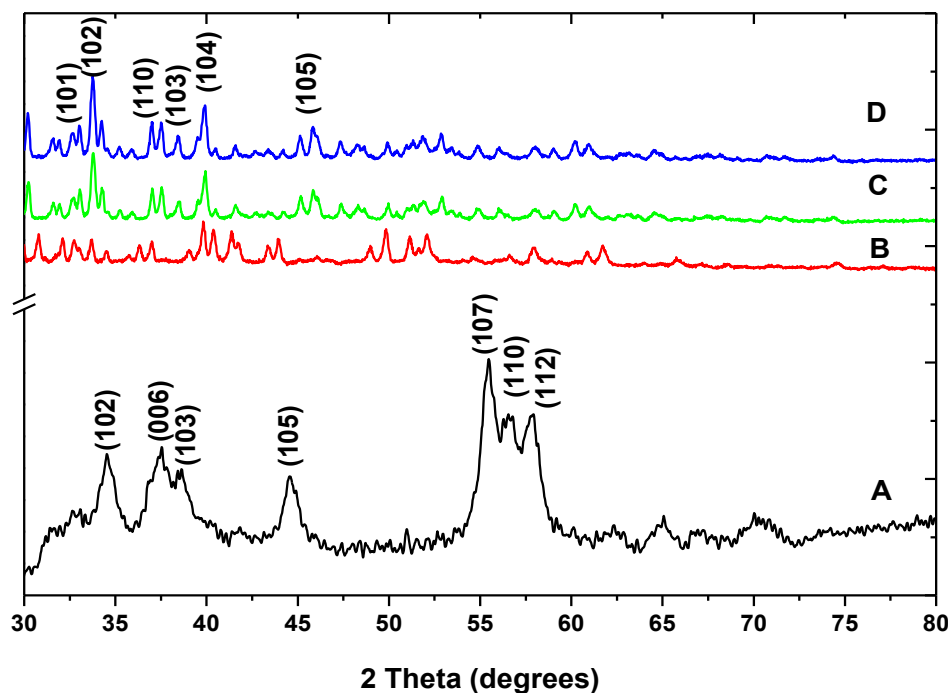


Figure 4.6: XRD spectra of copper sulfide nanoparticles capped with GSH (A), TGA (B), 18C6 (C) and L-Carn (D) synthesized at 95°C using SDEDTC as a sulfur source.

4.2.1.3 Infrared Spectra

The interaction between as-synthesized Cu_xS_y nanoparticles and their respective capping ligands was investigated using Fourier Transform Infrared (FT-IR) spectroscopy. Figure 4.7 shows the FT-IR spectra of pristine GSH (A) and GSH capped Cu_xS_y nanoparticles synthesized at 50°C (B) and 95°C (C). The spectrum of pristine GSH displays absorption bands at positions 3331 cm^{-1} and 3395 cm^{-1} , 2510 cm^{-1} and 1705 cm^{-1} which correspond to N-H, S-H and C=O stretching bands respectively. Additional absorption bands appearing at positions 1392 cm^{-1} and 1275 cm^{-1} correspond to the asymmetric COO^- stretching vibrations and the O-H rotational vibrations respectively. These, together with the C=O band, confirm the presence

of the carboxylic group of GSH. Furthermore, the appearance of C-N stretching vibrations at 1072 cm^{-1} proves the presence of peptide linkages and amine groups in the amino acid residues of GSH.

The FT-IR spectra of GSH capped Cu_xS_y nanoparticles show some of the characteristic absorption bands seen in the spectrum of pristine GSH, with the C=O peak now shifted to a lower wavenumber. However, the N-H and S-H absorption bands around 3331 cm^{-1} and 3234 cm^{-1} , and 2510 cm^{-1} have disappeared, indicating that GSH interacts with the surface of Cu_xS_y nanoparticles *via* the N-H and S-H functional groups from its cysteine residue. This is in agreement with the work reported by Li *et al.* [30] and Balavandy *et al.* [31] who synthesized GSH capped silver nanoparticles using a green method.

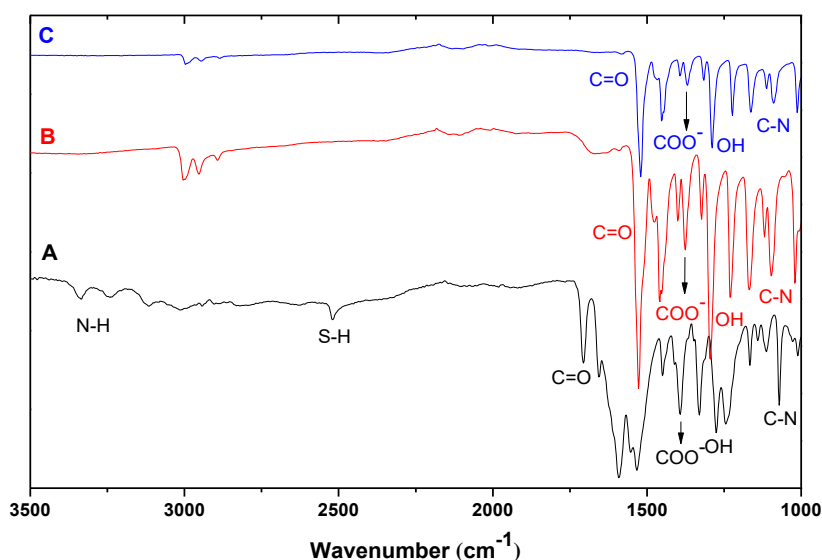


Figure 4.7: FT-IR spectra of pristine GSH (A) and GSH capped copper sulfide nanoparticles synthesized at 50 (B) and 95 °C (C) using SDEDTC as a sulfur source.

The FT-IR spectra of free TGA (A) and TGA capped Cu_xS_y nanoparticles synthesized at 50 (B) and 95 °C (C) are depicted in Figure 4.8. The FT-IR spectra of free TGA (Figure 4.8A) displays FT-IR absorption bands at positions 2590 cm^{-1} , 1700 cm^{-1} and 1400 cm^{-1} which represent the S-H, C=O and C-H stretching vibrations respectively. These are characteristic absorption bands for TGA. Similar absorption bands appear in the spectra of TGA capped Cu_xS_y nanoparticles; however these have shifted to lower wavenumbers. This is due to the

attraction by the field of solid surfaces. The S-H peak was not observed in the spectra of TGA capped Cu_xS_y nanoparticles. The absence of the S-H stretching mode around 2590 cm^{-1} signifies that the thiol group of TGA is bound to the surface atoms of Cu_xS_y nanoparticles through the Cu-S bond [32].

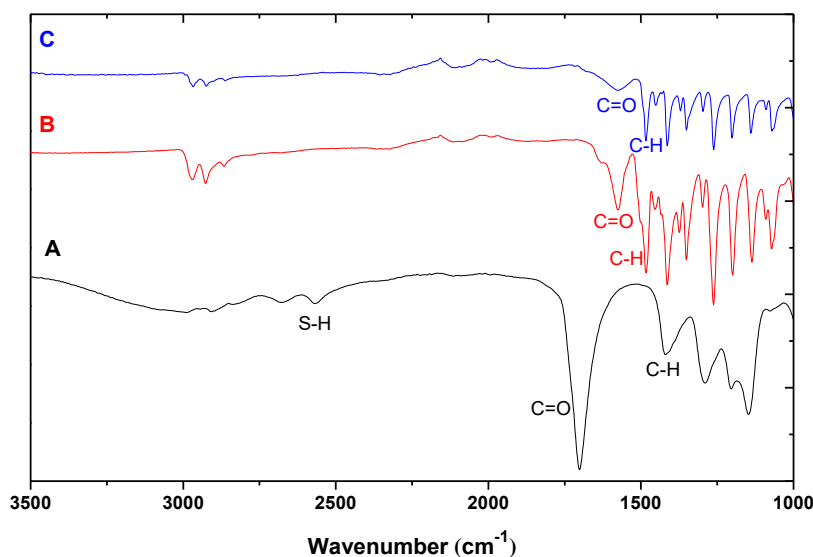


Figure 4.8: FT-IR spectra of pristine TGA (A) and TGA capped copper sulfide nanoparticles synthesized at 50 (B) and 95 °C (C) using SDEDTC as a sulfur source.

Figure 4.9 shows the FT-IR spectra of pristine 18C6 (A) and 18C6 capped Cu_xS_y nanoparticles synthesized at 50 (B) and 95 °C (C). The spectrum of pristine 18C6 shows absorption bands at positions 1467 cm^{-1} and 1353 cm^{-1} and 1140 cm^{-1} which signify the presence of the C-H bending vibrations and the C-O stretching vibrations of 18C6 respectively. The spectrum of 18-crown-6 capped Cu_xS_y nanoparticles show the C-H bending vibrations appearing at positions 1398 cm^{-1} and 1320 cm^{-1} , which are shifted to a lower wavenumber compared to those of pristine 18C6. However, the C-O stretch has disappeared signifying that 18C6 interacts with the surface of Cu_xS_y nanoparticles through the lone pairs of its C-O group. These findings agree well with work done by Al-amery *et al.* [33] who synthesized complexes of lanthanide picrates with crown ethers, i.e.; 18-crown-6 and 15-crown-5.

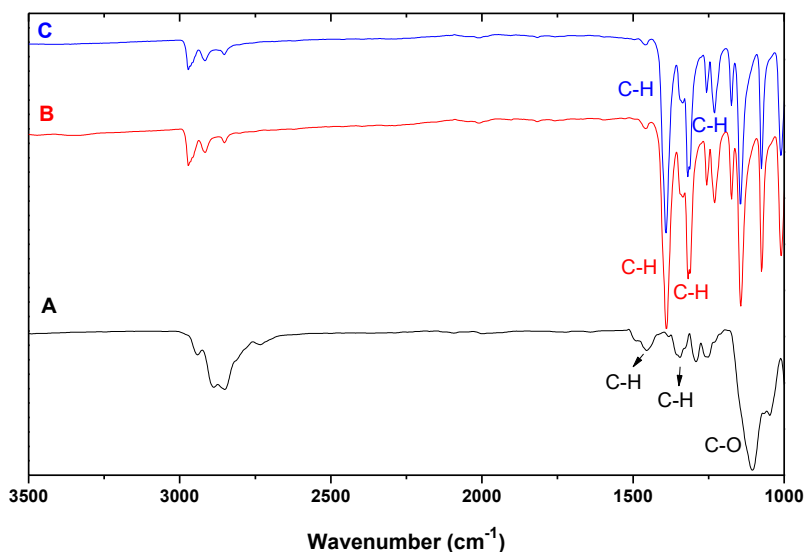


Figure 4.9: FT-IR spectra of pristine 18C6 (A) and 18C6 capped copper sulfide nanoparticles synthesized at 50 (A) and 95 °C (B) using SDEDTC as a sulfur source.

The spectrum of pristine L-Carn (Figure 4.10A) shows FT-IR absorption bands at positions 3237 cm^{-1} and 3049 cm^{-1} , 1705 cm^{-1} , 1570 cm^{-1} and 1404 cm^{-1} which correspond to N-H, C=O, C-C and COO^- stretching vibrations respectively. Similar absorption bands appear in the spectra of L-Carn capped Cu_xS_y nanoparticles synthesized at 50 (Figure 4.10B) and 95 °C (Figure 4.10C), except for the N-H vibration which has disappeared. This signifies that L-Carn interacts with Cu_xS_y nanoparticles *via* its amine group. Similar observations were made by Abdelkader *et al.* [34] when they synthesized L-carnosine-phospholipid complexes for ocular delivery of L-carnosine.

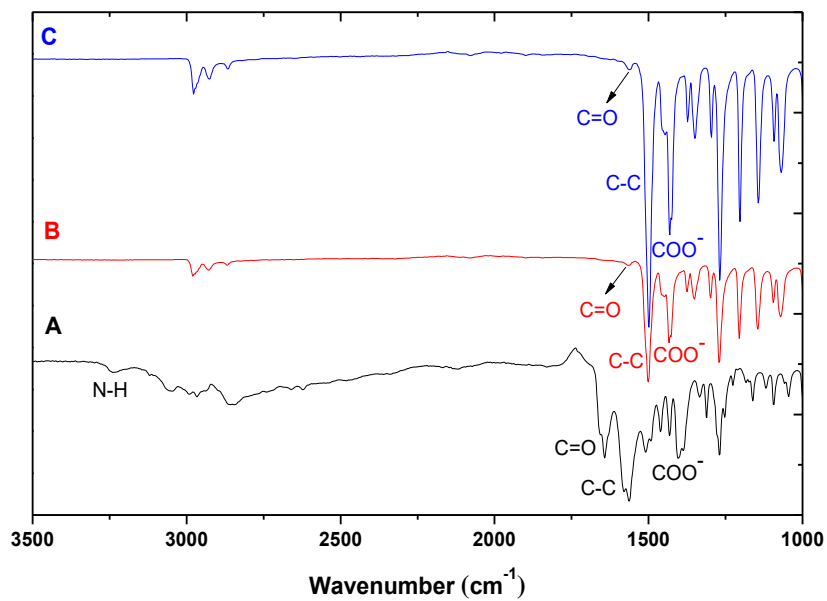


Figure 4.10: FT-IR spectra of pristine L-Carn (A) and L-Carn capped copper sulfide nanoparticles synthesized at 50 (B) and 95 °C (C) using SDEDTC as a sulfur source.

4.2.2 Characterization of copper sulfide nanoparticles synthesized using TAA as a sulfur source

4.2.2.1 Optical Properties

In this section copper sulfide nanoparticles were synthesized using thioacetamide as a sulfur source. All reaction parameters were kept constant and similar to those used in the previous section, 4.2.1. Figures 4.11A and 4.11B show the UV-vis absorption spectra of GSH, TGA, 18C6 and L-Carn capped Cu_xS_y nanoparticles produced at 50 and 95 °C respectively, dispersed in water, in the range of 250 to 1000 nm. The absorption spectra of Cu_xS_y nanoparticles synthesized at 50 °C show that the samples absorb in the region of 300 to 500 nm. The spectra further illustrate a rapid drop from 300 to 550 nm, with band edges appearing at 511 nm (2.43 eV), 509 nm (2.44 eV), 512 nm (2.42 eV) and 531 nm (2.34 eV) for nanoparticles capped with GSH, TGA, 18C6 and L-Carn respectively. These are blue shifted from the absorption spectra of bulk Cu_xS_y which is 1022 nm.

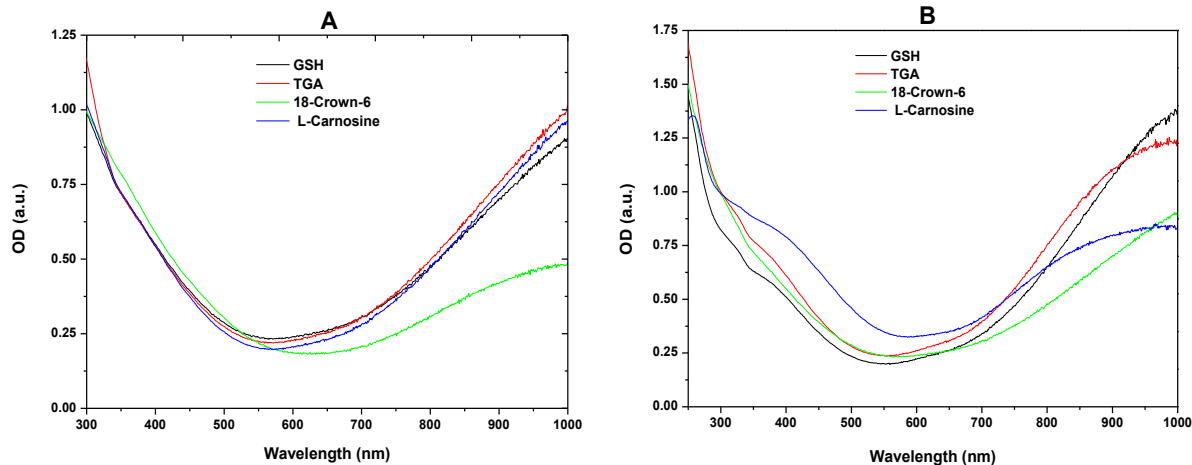


Figure 4.11: Absorption spectra of copper sulfide nanoparticles capped with GSH, TGA, 18-crown-6 and L-carnosine synthesized at 50 (A) and 95 °C (B) using TAA as a sulfur source.

A shift to higher wavelength was observed for all Cu_xS_y spectra after the temperature was increased to 95 °C, as seen in Figure 4.11B. All blue shifted absorption spectra depict nanoparticles that absorb strongly in the spectral region with band edges appearing at 542 (2.29 eV), 539 (2.30 eV), 531 nm (2.34 eV) and 571 (2.17 eV) for nanoparticles capped with GSH, TGA, 18C6 and L-Carn respectively. A broad shoulder in the 800 to 950 nm range that can be attributed to the d-d transition of Cu (II) state and is a general characteristic of the covellite phase was also observed for all the spectra.

The photoluminescence (PL) spectra of the as-synthesized Cu_xS_y nanoparticles are shown in Figure 4.12. For nanoparticles synthesized at 50 °C (Figure 4.12A), the maximum emission peaks appear at wavelength positioned at 620 nm, 605 nm, 588 nm and 598 nm for GSH, TGA, 18C6 and L-Carn capped Cu_xS_y nanoparticles respectively. Increasing the reaction temperature to 95 °C resulted in a minimal shift to higher wavelength of all the PL spectra as shown in Figure 4.12B. The maximum peaks have shifted from 620 to 623 nm, 605 to 622 nm, 588 to 591 nm and 598 to 605 nm for GSH, TGA, 18C6 and L-Carn capped Cu_xS_y nanoparticles respectively.

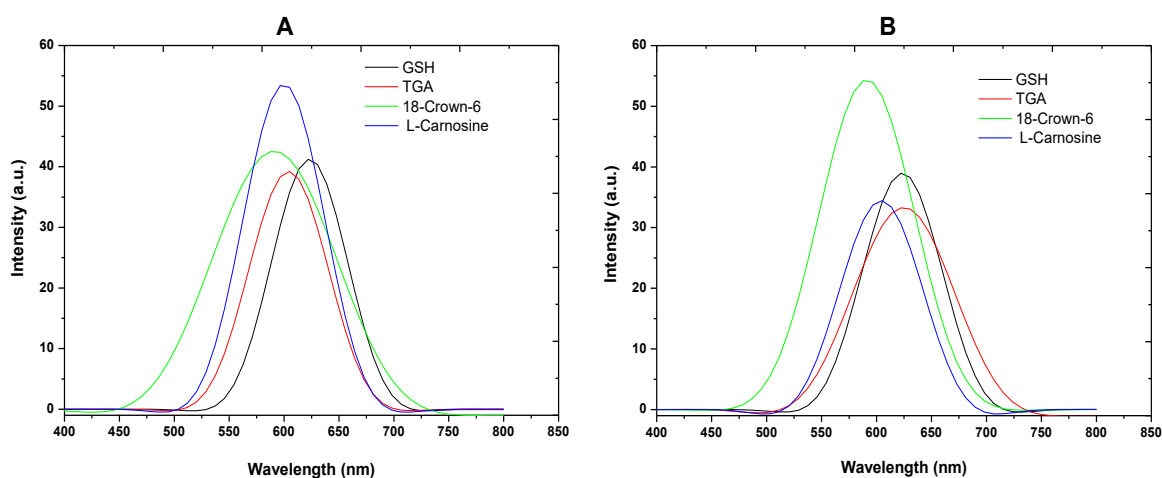


Figure 4.12: Emission spectra of copper sulfide nanoparticles capped with GSH, TGA, 18C6 and L-Carn synthesized at 50 (A) and 95 °C (B) using TAA as a sulfur source.

4.2.2.2 Structural Properties

TEM images of Cu_xS_y nanoparticles capped with GSH, TGA, 18C6 and L-Carn, synthesized at 50 °C are shown in Figure 4.13. Formation of nanoplates-like nanoparticles with an average diameter of 12.9 nm were observed when GSH (Figure 4.13A) was used as a capping agent. In the case of TGA capped Cu_xS_y nanoparticles (Figure 4.13B) spherical-like nanoparticles with an average diameter of 12.4 nm were observed. No aggregation of nanoparticles was observed when GSH and TGA were used at 50 °C. Employing 18C6 (Figure 4.13C) depicted spherical-like nanoparticles with an average diameter of 9.8 nm, while a mixture of rod-like and spherical-like nanoparticles were formed when L-Carn (Figure 4.13D) was used. However, signs of aggregation were observed in both images.

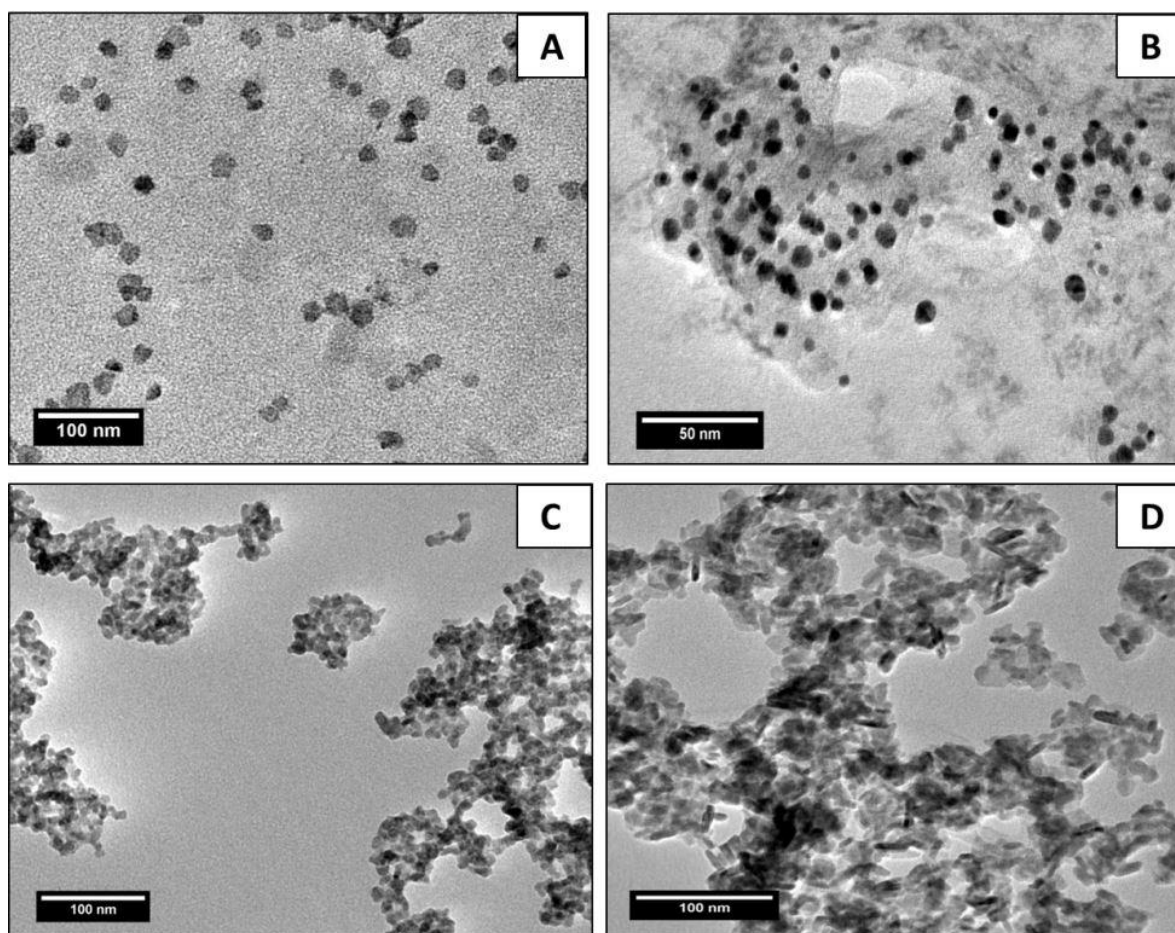


Figure 4.13: HR-TEM images of copper sulfide nanoparticles capped with GSH (A), TGA (B), 18C6 (C) and L-Carn (D) synthesized at 50 °C using TAA as a sulfur source.

A change in morphology was observed for some nanoparticles when the reaction temperature was increased to 95 °C. When GSH was used as a capping ligand, well-defined hexagonal-shaped nanoparticles with an average diameter of 14.5 nm were formed. The same is true for TGA capped nanoparticles, which have now formed well defined hexagonal plates with an average diameter of 25.6 nm. No change in terms of shape was observed in the TEM image of Cu_xS_y capped with 18C6. The particles still remained aggregated. A mixture of spherical and rod-like nanoparticles were still observed when L-Carn was used as a capping ligand. The increase in reaction temperature resulted in an increase in the size of nanoparticles as higher temperatures favour the fusion of smaller particles into bigger ones through the process of Ostwald ripening. This is in agreement with the red shift observed in the absorption spectra of nanoparticles from 50 to 95 °C. Temperature is one of the most important parameters in controlled synthesis of nanomaterials, and the formation of various shapes and sizes have been achieved previously by altering synthesis temperature.

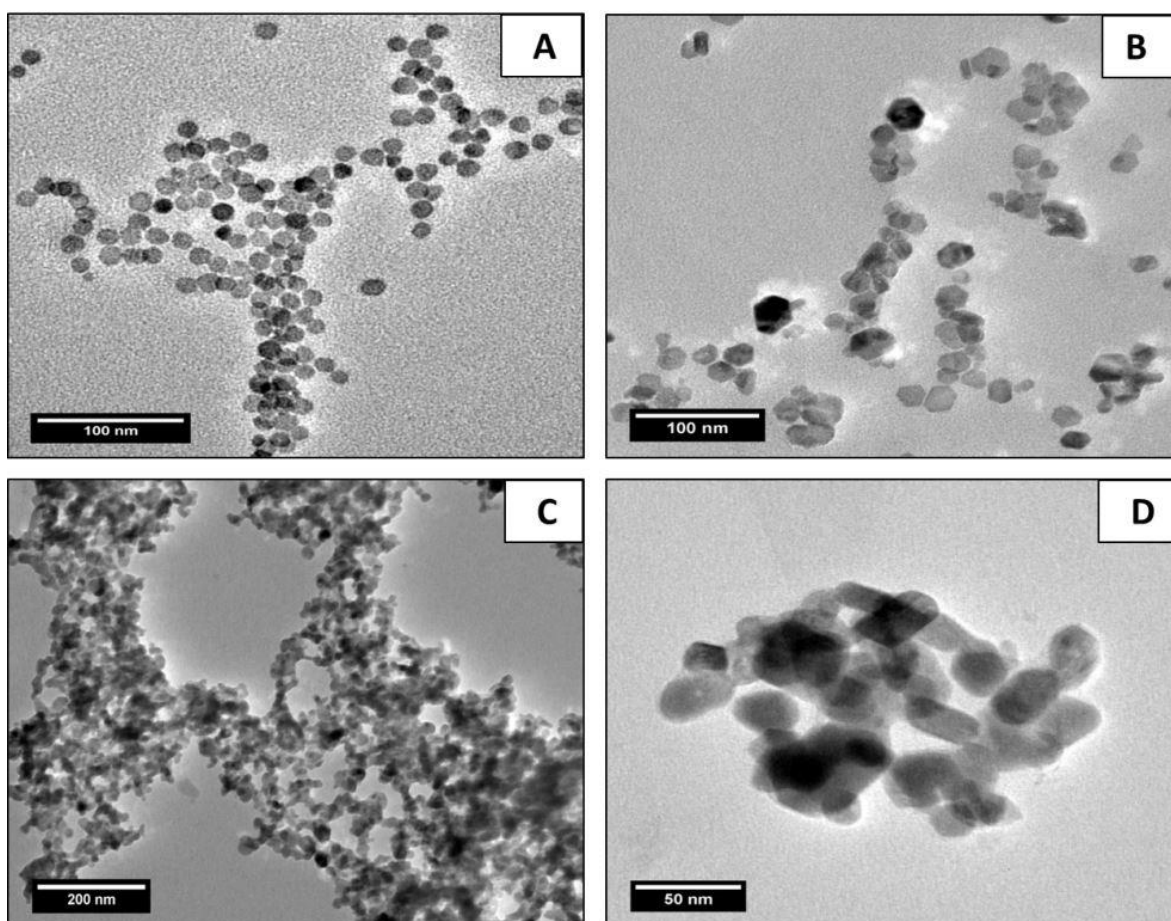


Figure 4.14: HR-TEM images of copper sulfide nanoparticles capped with GSH (A), TGA (B), 18C6 (C) and L-Carn (D) synthesized at 95 °C using TAA as a sulfur source.

Figure 4.15 presents the XRD patterns of CuS nanoparticles capped with GSH (Figure 4.15A), TGA (Figure 4.15B), 18C6 (Figure 4.15C) and L-Carn (Figure 4.15D) when the reaction temperature was set to 50 °C, with a reaction time of 1hr. The diffraction peaks appearing at 2θ positions of 31.71°, 34.12°, 37.05°, 40.91°, 45.93°, 56.47°, 62.06°, 67.26° and 70.14° correspond to miller indices (100), (102), (103), (104), (105), (110), (108), (202) and (116) of hexagonal covellite CuS (JCPDS, card number 4-784). No signs of impurities were observed, signifying the formation of pure CuS.

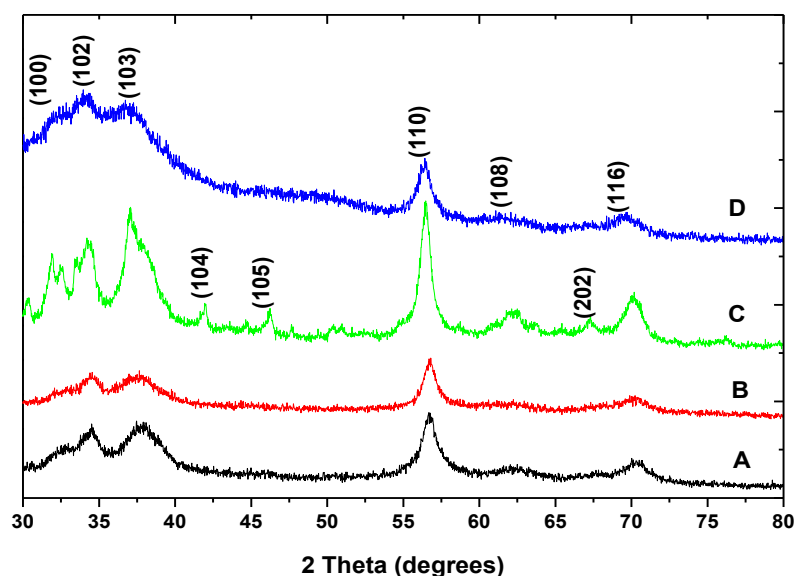


Figure 4.15: XRD spectra of copper sulfide nanoparticles capped with GSH (A), TGA (B), 18C6 (C) and L-Carn (D) synthesized at 50 °C using TAA as a sulfur source.

Similar XRD patterns were obtained when synthesis was conducted at 95 °C for all CuS nanoparticles capped with GSH, TGA, 18C6 and L-Carn. No signs of unreacted material peaks were observed. The peaks in the spectra of nanoparticles synthesized at 50 °C are broad which signifies the formation of smaller sized nanoparticles whereas peaks in the spectra of nanoparticles synthesized at 95 °C are narrow signifying the formation of bigger nanoparticles. This is in agreement with previously reported work which explains that highly crystalline nanoparticles are formed at higher temperatures [35].

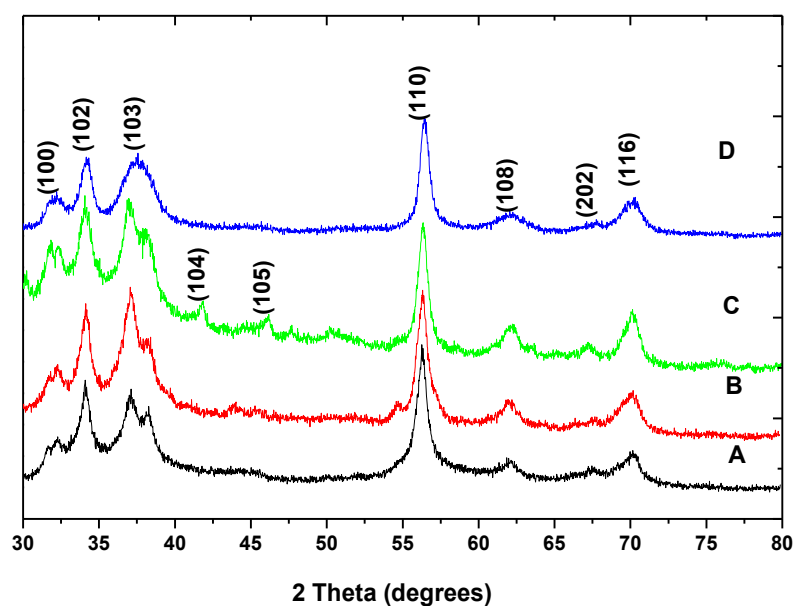


Figure 4.16: XRD spectra of copper sulfide nanoparticles capped with GSH (A), TGA (B), 18C6 (C) and L-Carn (D) synthesized at 95 °C using TAA as a sulfur source.

4.2.2.3 Infrared Spectra

Figure 4.17 shows the FT-IR spectra of pure GSH (A) and GSH-capped Cu_xS_y nanoparticles synthesized at 50 (B) and 95 °C (C) using TAA as a sulfur source. The spectrum of pure GSH shows FT-IR absorption bands appearing at positions 3331 cm^{-1} and 3395 cm^{-1} , 2510 cm^{-1} , 1705 cm^{-1} , 1392 cm^{-1} and 1275 cm^{-1} which represents the N-H, S-H, C=O, COO^- and O-H stretching bands respectively, which are characteristic to GSH. The spectra of GSH capped Cu_xS_y nanoparticles showed similar FT-IR absorption bands which have shifted to a lower wavenumber, but the N-H and S-H absorption bands have disappeared completely. This signifies that GSH binds to the surface of Cu_xS_y nanoparticles *via* N-H and S-H functional groups from its cysteine residue, as explained earlier in section 4.2.1.3.

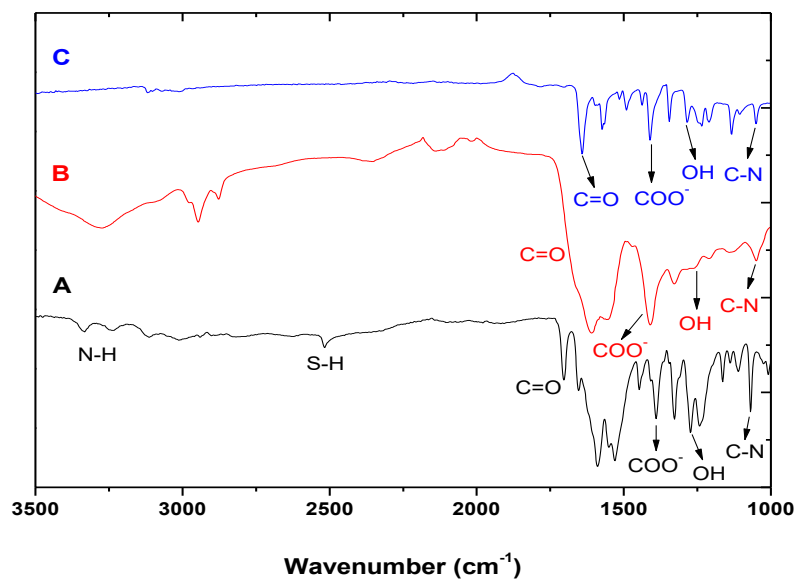


Figure 4.17: FT-IR spectra of pristine GSH (A) and GSH capped copper sulfide nanoparticles synthesized at 50 (B) and 95 °C (C) using TAA as a sulfur source.

The spectrum of pure TGA (Figure 4.18A) shows characteristic absorption bands at positions 2510 cm^{-1} , 1700 cm^{-1} and 1400 cm^{-1} which correspond to S-H, C=O and C-H stretching vibrations. FT-IR absorption bands corresponding to the C=O and C-H stretching vibrations were also observed in the spectra of TGA capped Cu_xS_y nanoparticles at 50 (Figure 4.18B) and 95 °C (Figure 4.18C), with the exception of the S-H peak. However, the C=O peak in the spectra of TGA capped nanoparticles has shifted to a lower wavenumber. The absence of the S-H peak in the spectra of TGA capped Cu_xS_y nanoparticles denotes that TGA interacts with Cu_xS_y nanoparticles *via* the S-H functional group.

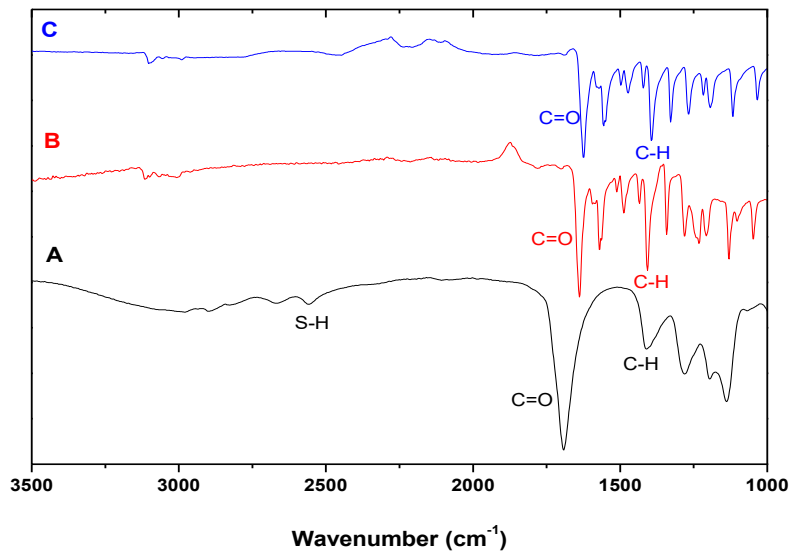


Figure 4.18: FT-IR spectra of pristine TGA (A) and TGA capped copper sulfide nanoparticles synthesized at 50 (B) and 95 °C (C) using TAA as a sulfur source.

Figure 4.19 shows the FT-IR spectra of pure 18C6 and 18C6 capped Cu_xS_y nanoparticles synthesized at 50 and 95 °C.

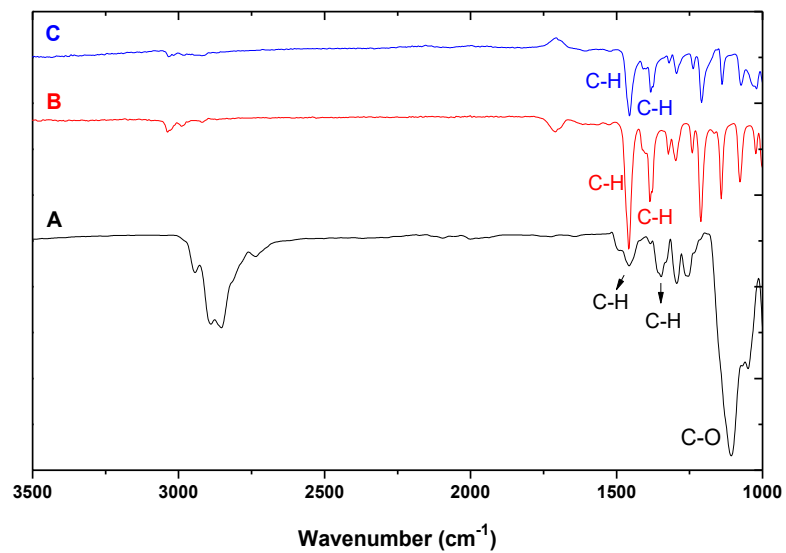


Figure 4.19: FT-IR spectra of pristine 18C6 (A) and 18C6 capped copper sulfide nanoparticles synthesized at 50 (B) and 95 °C (C) using TAA as a sulfur source.

From the spectra of pure 18C6, FT-IR absorption bands at positions 1467 cm^{-1} and 1353 cm^{-1} and 1140 cm^{-1} correspond to the C-H bending vibrations and the C-O stretching vibrations respectively, typical of 18C6. These absorption bands are also observed in the spectra of 18C6 capped Cu_xS_y nanoparticles with the exception of the C-O stretching vibration. This denotes that 18C6 binds to Cu_xS_y nanoparticles via the lone pairs of the C-O group.

Figure 4.20 shows the FT-IR spectra of pure L-Carn and L-Carn capped Cu_xS_y nanoparticles synthesized at 50 and 95 °C. The spectra of pure L-Carn depicts characteristic FT-IR absorption bands for N-H, C=O, C-C and COO^- stretching vibrations appearing at positions 3237 cm^{-1} , 1705 cm^{-1} , 1570 cm^{-1} and 1404 cm^{-1} respectively. The C=O and C-C absorption bands remain visible in the spectra of L-Carn capped Cu_xS_y nanoparticles but the N-H peak has disappeared which means that L-Carn binds to the nanoparticles via the amine group.

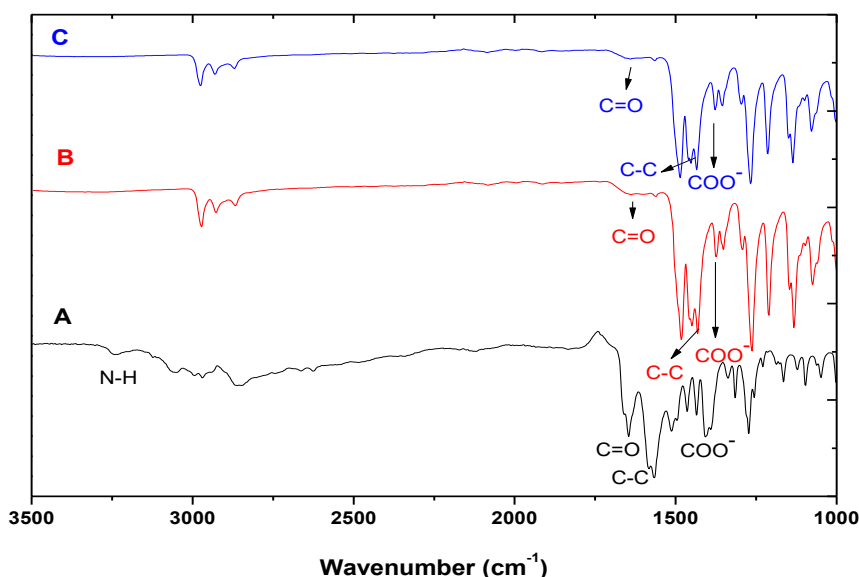


Figure 4.20: FT-IR spectra of pristine L-Carn (A) and L-Carn capped copper sulfide nanoparticles synthesized at 50 (B) and 95 °C (C) using TAA as a sulfur source.

4.3 Conclusions

Water soluble quantum dots were synthesized for use as fluorescent probes in disease imaging. Synthesis was conducted using copper chloride as a copper source and two different sulfur sources, namely sodium diethyldithiocarbamate and thioacetamide. Four different capping ligands were used, i.e. glutathione, thioglycolic acid, 18-crown-6 and L-carnosine. During synthesis, the effect of reaction temperature on the formation of nanoparticles was investigated. As such, reactions were performed at both lower (50 °C) and higher reaction temperatures (95 °C).

The UV-vis spectra depicted absorption peaks and band edges which are blue-shifted from bulk CuS. The PL spectra showed emission peaks which are red-shifted from their corresponding absorption spectra, due to quantization effects indicating the formation of nanoparticles. A red shift was observed in the UV spectra of CuS nanoparticles, from 50 to 95 °C, indicating an increase in nanoparticle size. The structural properties were confirmed by HR-TEM, with the size of nanoparticles increasing with an increase in reaction temperature, agreeing with findings from the UV spectra. Moreover, a change in the shape from spheres to hexagonal plates was observed at higher temperatures, when GSH was employed as a capping ligand.

The phase ID was investigated by XRD, and it was observed that a mixture of phases (covellite and chalcocite) were formed when SDEDTC is used as a sulfur source, at both temperatures, except for GSH capped Cu_xS_y which formed a single phase when the reaction temperature was increased to 95 °C. However, when TAA was used as a sulfur source, a pure phase (covellite) was formed at both reaction temperatures. TAA has proved a suitable sulfur source that yields good quality Cu_xS_y nanoparticles at 95 °C.

The use of various capping ligands and sulfur sources had some influence in nanoparticle formation, with GSH regarded as a ligand of choice and thioacetamide a more suitable sulfur source. However, the reaction temperature was seen to be the contributing factor that controls nanoparticle formation.

4.4 References

- [1]. Y. Xie, A. Riedinger, M. Prato, A. Casu, A. Genovese, P. Guardia, S. Sottini, C. Sangregorio, K. Miszta, S. Ghosh, T. Pellegrino, L. Manna. *J. Am. Chem. Soc.*, **2013**, 135, 17630 – 17637.
- [2]. H. Y. Wang, X. W. Hua, F. G. Wu, B. Li, P. Liu, N. Gu, Z. Wang and Z. Chen. *Appl Mater Interfaces.*, **2015**, 7, 7082 – 7092.
- [3]. M. Kruszynska, H. Borchert, A. Bachmatiuk, M. H. Rummeli, B. Buchner, J. Parisi and J. Kolny-Olesiak. *ACS Nano*, **2012**, 6, 5889 – 5896.
- [4]. Y. Zhu, J. Peng, L. Jiang and J. Zhu. *Analyst*, **2014**, 139, 649 – 655.
- [5]. Y. Wang, Y. Hu, Q. Zhang, J. Ge, Z. Lu, Y. Hou and Y. Yin. *Inorg. Chem.*, **2010**, 49, 6601 – 6608.
- [6]. G. Ma, Y. Zhou, X. Li, K. Sun, S. Liu, J. Hu and N. A. Kotov. *ACS Nano.*, **2013**, 7, 9010 – 9018.
- [7]. N. J. Freymeyer, P. D. Cunningham, E. C. Jones, B. J. Golden, A. M. Wiltrout and K. E. Plass. *Cryst. Growth Des.*, **2013**, 13, 4059 – 4065.
- [8]. F. Wang, Q. Li, L. Lin, H. Peng, Z. Liu and D. Xu. *J. Am. Chem. Soc.*, **2015**, 137, 12006 – 12012.
- [9]. Y. Huang, Y. Lai, S. Shi, S. Hao, J. Wei and X. Chen. *Chem. Asian J.*, **2015**, 10, 370 – 376.
- [10]. F. Chen, H. Hong, S. Goel, S. A. Graves, H. Orbay, E. B. Ehlerding, S. Shi, C. P. Theuer, R. J. Nickles and W. Cai. *ACS Nano.*, **2015**, 9, 3926 – 3934.
- [11]. S. Goel, F. Chen and W. Cai. *Small*, **2014**, 10, 4, 631 – 645.
- [12]. W. W. Yu, E. Chang, R. Drezek and V. L. Colvin. *Biochem. Biophys. Res. Commun.*, **2006**, 348, 781 – 786.
- [13]. F. O. Silva, M. S. Carvalho, R. Mendonca, W. A.A. Macedo, K. Balzuweit, P. Reiss and M. A. Schiavon. *Nanoscale Res. Lett.*, **2012**, 7, 1 – 10.

- [14]. Y. He. *InTech.*, **2012**. ISBN 978-953-51-0483-4
- [15]. N. T. K. Thanh and L. A. W. Green. *Nano Today.*, **2010**, 5, 213 – 230.
- [16]. A. Fontes, B. S. Santos, C. R. Chaves and R. C. B. Q. Figueiredo. *InTech*. ISBN: 978-953-51-0483-4.
- [17]. S. M. Farkhani and A. Valizadeh. *IET Nanobiotechnol.*, **2014**, 8, 59 – 76.
- [18]. M. Z. Hu, T. Zhu. *Nanoscale Res. Lett.*, **2015**, 10, 469.
- [19]. X. C. Jiang, W. M. Chen, C. Y. Chen, S. X. Xiong, A. B. Yu. *Nanoscale Res. Lett.*, **2011**, 6, 32.
- [20]. S. Yadav, P. K. Bajpai. *Nano-Structures & Nano-Objects.*, **2017**, 10, 151 – 158.
- [21]. M. Mousavi-Kamazani, Z. Zarghami and M. Salavati-Niasari. *J. Phys. Chem. C.*, **2016**, 120, 2096 – 2108.
- [22]. P. Priyadharshini, R. Rajagopal. *Int. J. Recent Sci. Res.*, **2015**, 6, 3328 – 3331.
- [23]. S. K. Maji, N. Mukherjee, A. K. Dutta, D. N. Srivastava, P. Paul, B. Karmakar, A. Mondal, B. Adhikary. *Mater. Chem. Phys.*, **2011**, 130, 392 – 397.
- [24]. Y. Du, Z. Yin, J. Zhu, X. Huang, X-J. Wu, Z. Zeng, Q. Yan, H. Zhang. *Nat. Commun.*, **2012**, 3, 1 – 7.
- [25]. Z. Cheng, S. Wang, Q. Wang, B. Geng. *Cryst.Eng. Comm.*, **2010**, 12, 144 – 149.
- [26]. K. Tang, D. Chen, Y. Liu, G. Shen, H. Zheng, Y. Qian. *Journal of Crystal Growth*, **2004**, 263, 232 – 236.
- [27]. L. Gao, E. Wang, S. Lian, Z. Kang, Y. Lan, D. Wu. *Solid State Communications*, **2004**, 130, 309 – 312.
- [28]. X. Wang, C. Xu, Z. Zhang. *Materials Letters*, **2006**, 60, 345 – 348.
- [29]. M. Saranya, C. Santhosh, S. P. Augustine, A. N. Grace. *J. Exp. Nanosci.*, **2014**, 9, 329 – 336.

- [30]. H. Li, Z. Cui, C. Han. *Sensors Actuat B-Chem.*, **2009**, 143, 87 - 89.
- [31]. S. K. Balavandy, K. Shameli, D. R. B. A. Biak, Z. Z. Abidin. *Chemistry Central Journal.*, **2014**, 8, 1 – 10.
- [32]. C. I. L. Santos, M. S. Carvalho, E. Raphael, C. Dantas, J. L. Ferrari, M. A. Schiavon. *Materials Research.*, **2016**, 19, 1407 – 1416.
- [33]. M. H. A. Al-Amery, B. I. Al-Abdaly, M. K. Albayaty. *Orient. J. Chem.*, **2016**, 32, 1025 – 1048.
- [34]. H. Abdelkader, M. R. Longman, R. G. Alany, B. Pierscioneck. *Int. J. Nanomedicine*, **2016**, 11, 2815 – 2827.
- [35]. F. F. Castellón-Barraza, M. H. Farías, J. H. Coronado-López, M. A. Encinas-Romero, M. Pérez-Tello, R. Herrera-Urbina, A. Posada-Amarillas. *Adv. Sci. Lett.*, **2011**, 4, 1 – 6.

Chapter 5: Results for Characterization of Cobalt Sulfide Nanoparticles

5.1 Introduction

Cobalt sulfide has been found to contain unique catalytic, electric, electrochemical, optical and magnetic properties. Consequently, cobalt sulfide has been used across a myriad of applications within the energy sector, and has recently gained interest within the biological research field. Cobalt sulfide consists of various stoichiometric ratios such as Co_4S_3 , Co_9S_8 , CoS , Co_{1-x}S , Co_3S_4 , Co_2S_3 and CoS_2 [1 - 4].

These diverse stoichiometric ratios pose a challenge on shape and phase-controlled synthesis. This due to the fact that the stoichiometric ratio of cobalt sulfide is much more complicated than that of cobalt oxide because of the coexistences of strong reducing cobalt ions and oxidizable sulfide ions. Moreover, cobalt ions have been reported to have very strong affinity towards oxygen, thus making it difficult to eliminate cobalt oxide or cobalt hydroxide impurities from the reaction products.

It has been reported that the properties of cobalt sulfide nanoparticles are strongly dependent upon their size, shape, distribution and surface. Moreover, properties, morphology and stoichiometric composition of cobalt sulfide are greatly influenced by the mechanism used during synthesis [5 - 8]. Cobalt sulfide nanoparticles with varying morphologies (nanotubes, nanowires and hollow spheres) have been synthesized successfully using different synthesis methods. Using a hydrothermal synthesis route, Emadi and colleagues successfully produced nanocrystalline Co_3S_4 nanoparticles. In their work, they reported the influence of reaction time, temperature and the concentration of reactants on the shape and size of cobalt sulfide nanoparticles [9, 10].

In this chapter, the characterization of cobalt sulfide nanoparticles for potential use as fluorescent probes for disease imaging is reported. The as-synthesized water soluble nanoparticles can be used directly in biological applications without the need to render them biocompatible.

5.2 Results and Discussion

Cobalt sulfide (Co_xS_y) nanoparticles were synthesized using cobaltous chloride as a metal source and sodium diethyldithiocarbamate (SDEDTC) or thioacetamide (TAA) as sulfur sources. Glutathione (GSH), thioglycolic acid (TGA), 18-crown-6 (18C6) and L-carnosine (L-Carn) were all used as capping ligands during the synthesis process. Reactions were conducted at different temperatures which are 50 and 95 °C, with water used as a solvent.

5.2.1 Characterization of cobalt sulfide nanoparticles synthesized using SDEDTC as a sulfur source

5.2.1.1 Optical properties

Controlled synthesis of Co_xS_y nanomaterials poses serious challenges since cobalt sulfide can exist in various phases. A variety of parameters including the concentration of reactants, capping agents, pH, as well as the reaction temperature, can influence the morphology, phase and size of as-synthesized nanoparticles [11]. The absorption spectra of Co_xS_y nanoparticles synthesized at 50 and 95 °C are shown in Figure 5.1. At 50 °C (Figure 5.1A), the spectra depicted numerous excitonic peaks or broad shoulders, with the first peak considered as the band-gap of the material [12]. These peaks or shoulders are observed in the wavelength range between 400 – 700 nm, and have band edges appearing at 584 nm, 599 nm, 592 nm and 597 nm for Co_xS_y nanoparticles capped with GSH, TGA, 18C6 and L-Carn respectively. The spectra are blue shifted with respect to their bulk Co_xS_y counterpart which appears at 1127.27 nm. The shifting of peaks to lower wavelength or higher energy is due to the quantization of energy states in nano-sized cobalt sulfide materials [13,14].

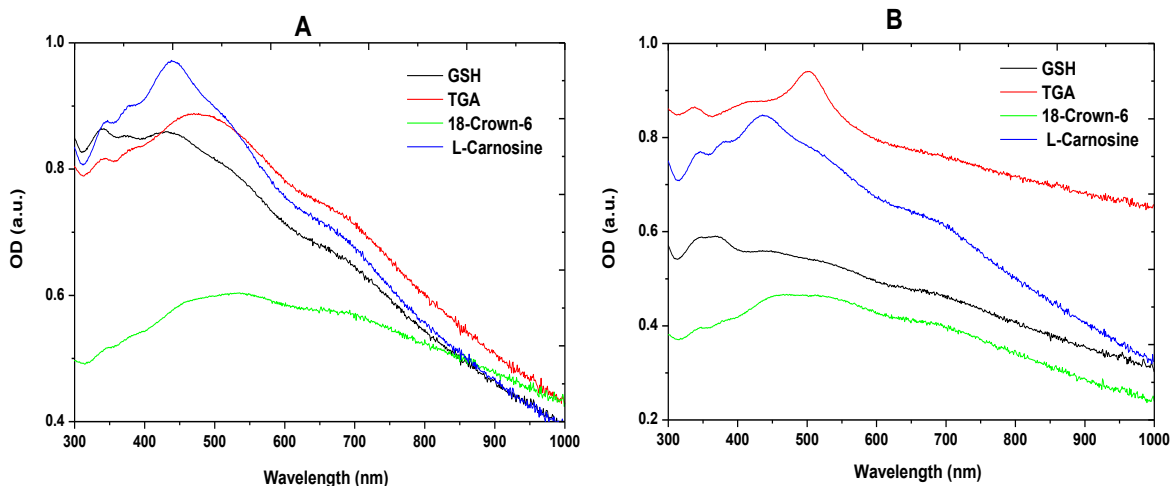


Figure 5.1: Absorption spectra of cobalt sulfide nanoparticles capped with GSH, TGA, 18C6 and L-Carn synthesized at 50 °C (A) and 95 °C (B) using SDEDTC as a sulfur source.

At 95 °C (Figure 5.1B), similar profiles are seen in the absorption spectra of as-synthesized Co_xS_y nanoparticles. However, the band edges at 95 °C have shifted slightly to higher wavelength positions i.e.; from 584 to 591 nm, 599 to 606 nm, 592 to 600 nm and 597 to 619 nm for Co_xS_y nanoparticles capped with GSH, TGA, 18C6 and L-Carn respectively. This is due to particle size increase.

The emission properties of as-synthesized Co_xS_y nanoparticles were investigated using photoluminescence spectroscopy. Figure 5.2 shows the emission spectra of GSH, TGA, 18C6 and L-Carn capped Co_xS_y nanoparticles synthesized at 50 (Figure 5.2A) and 95 °C (Figure 5.2B) for 1 hr. All spectra of Co_xS_y nanoparticles synthesized at 50 °C display single emission peaks appearing at wavelength positions of 711 nm, 700 nm, 704 nm and 697 nm for Co_xS_y nanoparticles capped with GSH, TGA, 18C6 and L-Carn respectively. The recorded emission spectra are red shifted from their corresponding absorption spectra, as shown in Figure 5.1 [15]. When the reaction temperature was increased to 95 °C (Figure 5.2B), a shift to higher wavelength was observed in all PL spectra. The maximum peaks have shifted from 711 to 735 nm, 700 to 757 nm, 704 to 744 nm and 697 to 748 nm for GSH, TGA, 18C6 and L-Carn capped Co_xS_y nanoparticles respectively.

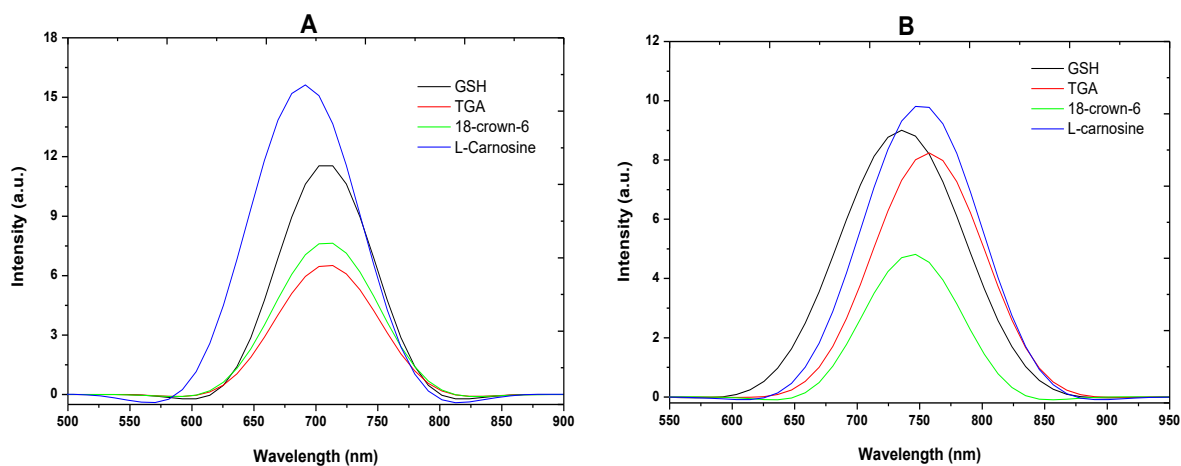


Figure 5.2: Emission spectra of cobalt sulfide nanoparticles capped with GSH, TGA, 18C6 and L-Carn synthesized at 50 °C (A) and 95 °C (B) using SDEDTC as a sulfur source.

5.2.1.2 Structural Properties

Figure 5.3 shows TEM micrographs of Co_xS_y nanoparticles synthesized at 50 °C, with a reaction time of 1 hr. Near-spherical particles with average diameters of 3.2, 18.6 and 33.5 nm were obtained when GSH (Figure 5.3A), TGA (Figure 5.3B) and L-Carn (Figure 5.3D) were used as capping ligands while 18C6 (Figure 5.3C) capped Co_xS_y yielded bigger particles that have aggregated together, with the measured ones depicting an average diameter of 395.8 nm.

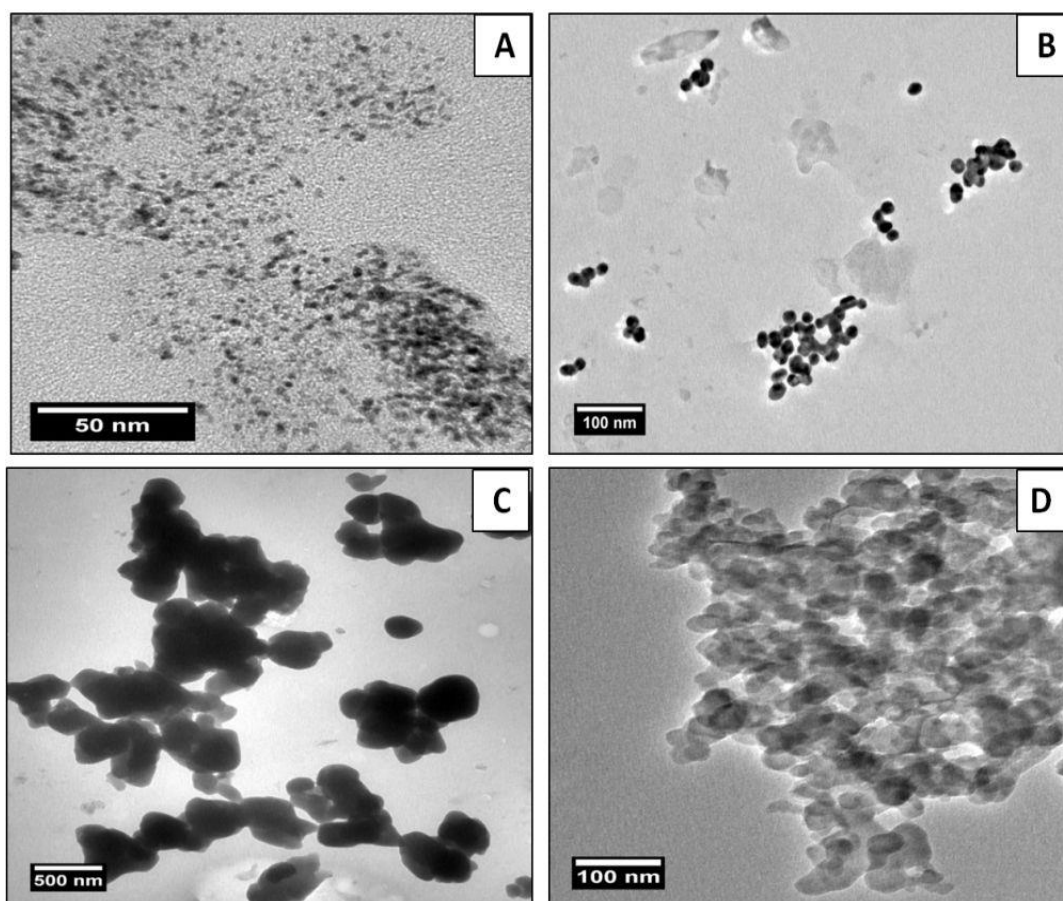


Figure 5.3: HR-TEM images of cobalt sulfide nanoparticles capped with GSH (A), TGA (B), 18C6 (C) and L-Carn (D) synthesized at 50 °C using SDEDTC as a sulfur source.

Upon reaction temperature increase to 95 °C (Figure 5.4), an increase in nanoparticle size was observed, with most particles maintaining a similar shape. The average diameters of Co_xS_y nanoparticles capped with GSH (Figure 5.4A), TGA (Figure 5.4B), 18C6 (Figure 5.4C) and L-Carn (Figure 5.4D) were measured to be 12.2, 45.4, 404.7 and 38.6 nm respectively. The increase in synthesis temperature resulted in an increase in nanoparticle size, a phenomenon that has been reported previously [16]. This is in agreement with the observation made earlier, where there was a slight red shift in the absorption spectra of nanoparticles from 50 to 95 °C.

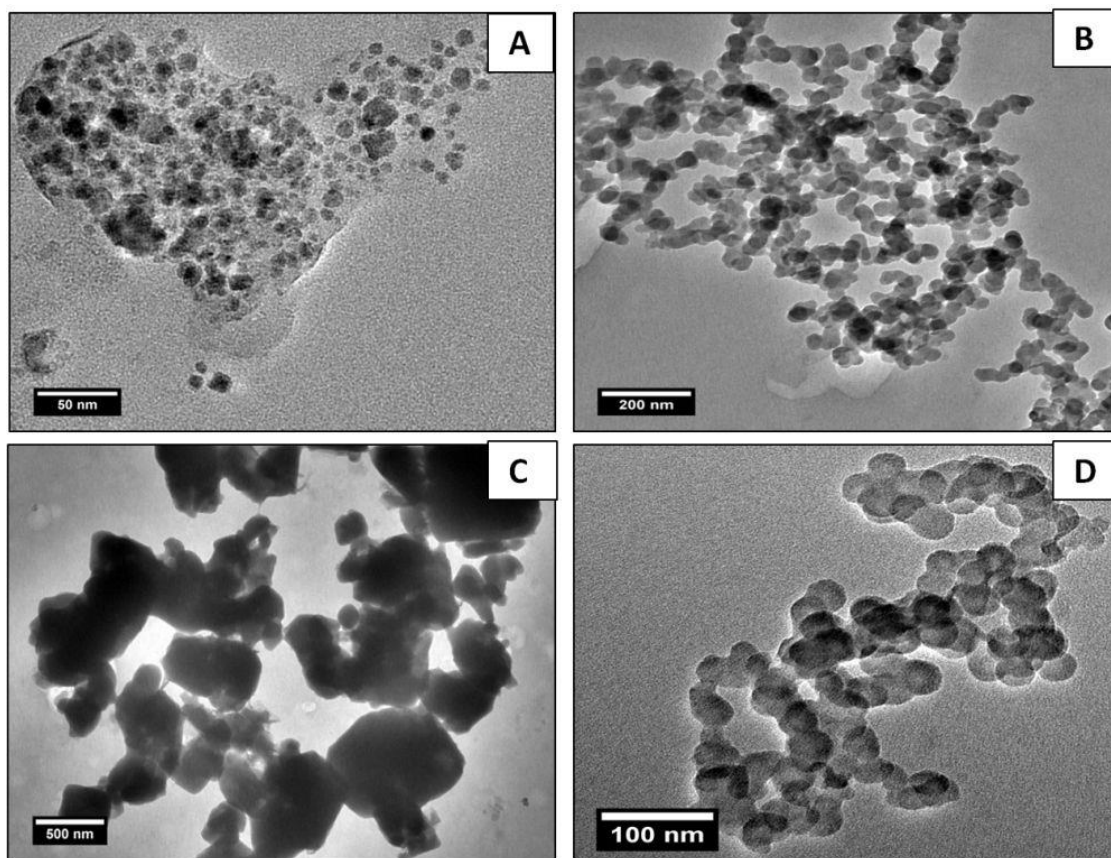


Figure 5.4: HR-TEM images of cobalt sulfide nanoparticles capped with GSH (A), TGA (B), 18C6 (C) and L-Carn (D) synthesized at 95 °C using SDEDTC as a sulfur source.

The XRD patterns of as-synthesized Co_xS_y nanoparticles capped with GSH, TGA, 18C6 and L-Carn, synthesized at 50 °C with a reaction time of 1hr are shown in Figure 5.5. The XRD patterns exhibited peaks at 2θ positions of 26.5°, 32.9° and 41.9° corresponding to (220), (222) and (311) of face-centred cubic Co_3S_4 (JCPDS, card number 4-784). In the same XRD patterns, the presence of peaks at 2θ positions of 27.8° and 32.2°, corresponding to (111) and (200) respectively of cubic CoS_2 , were also noticed. This is an evidence that two phases were formed, namely Co_3S_4 and CoS_2 . Signs of unmatched peaks were observed in the diffraction patterns of Co_xS_y nanoparticles synthesized at 50 °C, irrespective of the capping agent used, signifying the presence of impurities.

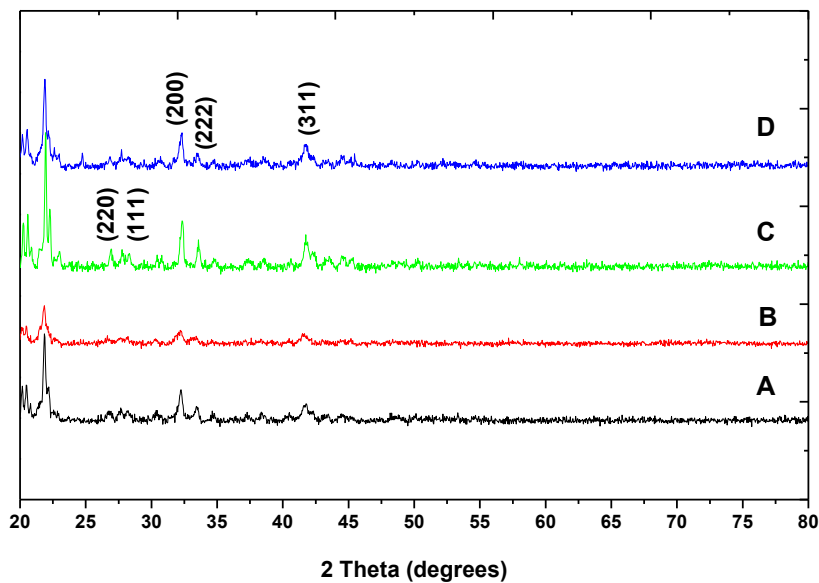


Figure 5.5: XRD spectra of cobalt sulfide nanoparticles capped with GSH (A), TGA (B), 18C6 (C) and L-Carn (D) synthesized at 50 °C using SDEDTC as a sulfur source.

Similar phases were formed when nanoparticles were synthesized at 95 °C, as seen in Figure 5.6 A to D. The formation of multiple phases of cobalt sulfide within a sample has been reported previously in literature, with authors reporting the difficulty of obtaining a pure phase of cobalt sulfide due to its complex stoichiometry [17].

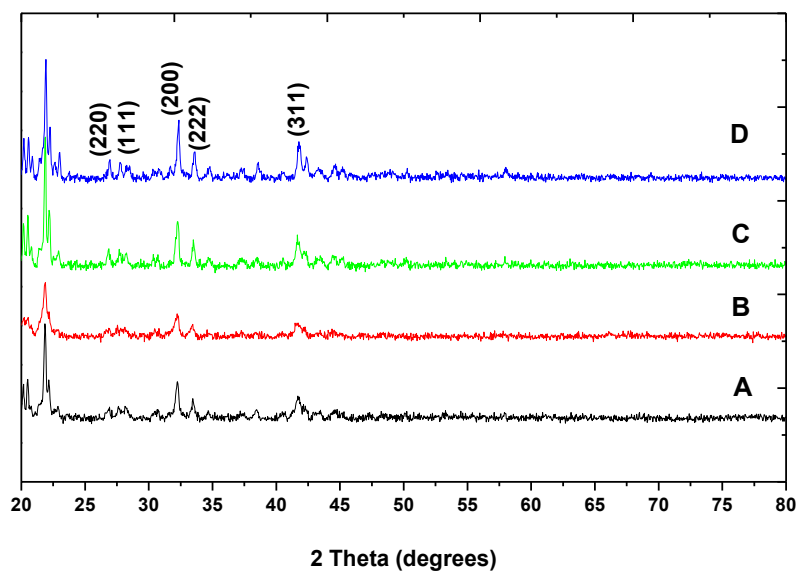


Figure 5.6: XRD spectra of cobalt sulfide nanoparticles capped with GSH (A), TGA (B), 18C6 (C) and L-Carn (D) synthesized at 95 °C using SDEDTC as a sulfur source.

5.2.1.3 Infrared Spectra

Figure 5.7 shows the FT-IR spectra of pristine GSH (A) and GSH capped Co_xS_y nanoparticles synthesized at 50 (B) and 95 °C (C). The characteristic spectrum of pristine GSH was reported in section 4.2.1.3. Table 5.1 summarizes the FT-IR spectra of pristine GSH and GSH capped Co_xS_y nanoparticles. The spectra of GSH capped Co_xS_y nanoparticles shows similar absorption bands as that of pristine GSH, with the exception of N-H and S-H stretches around 3331 cm^{-1} and 3234 cm^{-1} , and 2510 cm^{-1} that have disappeared. This indicates that GSH interacts with the surface of Co_xS_y nanoparticles via the N-H and S-H functional groups from its cysteine residue, as reported previously [18].

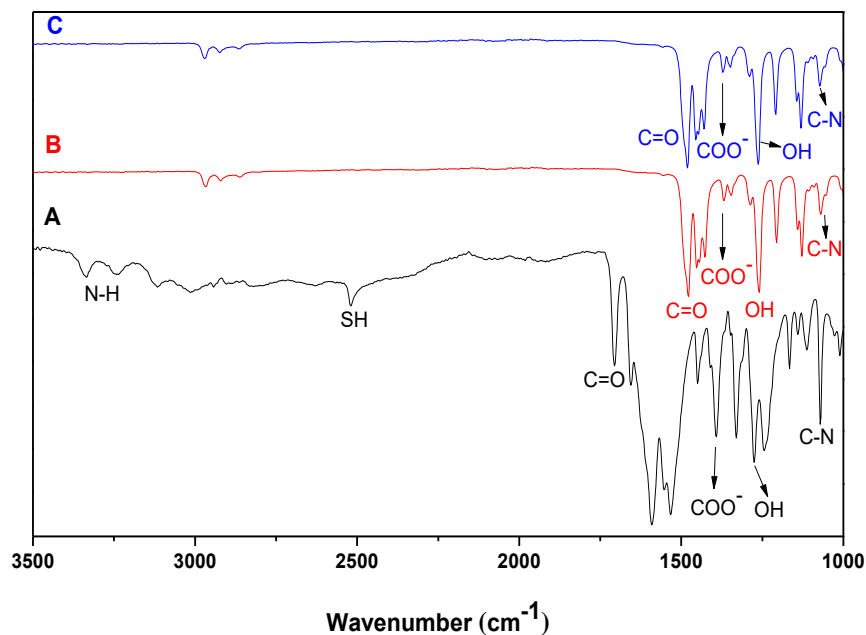


Figure 5.7: FT-IR spectra of pristine GSH (A) and GSH capped cobalt sulfide nanoparticles synthesized at 50 (B) and 95 °C (C) using SDEDTC as a sulfur source.

Table 5.1: FT-IR data of cobalt sulfide nanoparticles capped with GSH synthesized using SDEDTC as a sulfur source.

Compound	(N-H)	(S-H)	(C=O)	(COO ⁻)	(O-H)	(C-N)
GSH	3331; 3395 cm ⁻¹	2510 cm ⁻¹	1705 cm ⁻¹	1392 cm ⁻¹ 1	1392 cm ⁻¹	1072 cm ⁻¹ 1
Co_xS_y-GSH 50	—	—	1482 cm ⁻¹	1373 cm ⁻¹ 1	1273 cm ⁻¹	1069 cm ⁻¹ 1
Co_xS_y -GSH 95	—	—	1482 cm ⁻¹	1373 cm ⁻¹ 1	1274 cm ⁻¹	1068 cm ⁻¹ 1

Figure 5.8 shows the FT-IR spectra of pristine TGA (A) and TGA capped Co_xS_y nanoparticles synthesized at 50 (B) and 95 °C (C). Table 5.2 summarizes the FT-IR spectra of pristine TGA and as-synthesized TGA capped Co_xS_y nanoparticles. From this, it is clear that

TGA interacts with Co_xS_y nanoparticles via its thiol group, which forms a covalent bond with Co atoms on the surface of as-synthesized Co_xS_y nanoparticles. Similar results were obtained by Santos *et al.* [19] when they synthesized water soluble CdSe nanoparticles using TGA as a capping ligand. The same was reported by Vikraman *et al.* when they synthesized CdS nanoparticles capped with TGA for use as fluorescent probes for the detection of dopamine [20]. A shift to a lower wavenumber was observed in the peak corresponding to the C=O stretch when TGA is bound to nanoparticles.

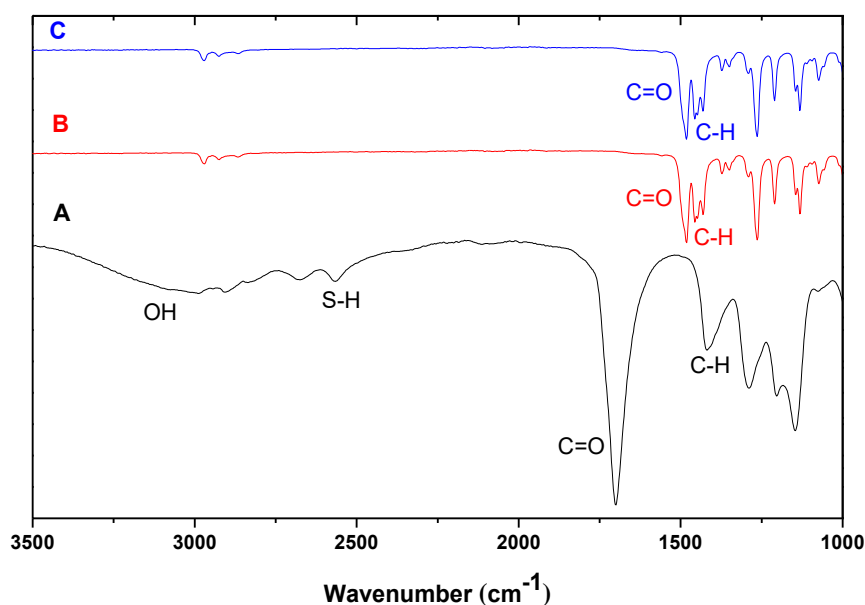


Figure 5.8: FT-IR spectra of pristine TGA (A) and TGA capped Co_xS_y nanoparticles synthesized at 50 (B) and 95 °C (C) using SDEDTC as a sulfur source.

Table 5.2: FT-IR data of cobalt sulfide nanoparticles capped with TGA synthesized using SDEDTC as a sulfur source.

Compound	(S-H)	(C=O)	(C-H)	(O-H)
TGA	2563 cm^{-1}	1700 cm^{-1}	1410 cm^{-1}	3300 - 2900 cm^{-1}
Co_xS_y -TGA 50	—	1485 cm^{-1}	1429 cm^{-1}	—
Co_xS_y -TGA 95	—	1479 cm^{-1}	1426 cm^{-1}	—

Figure 5.9 shows the FT-IR spectra of pristine 18C6 (A) and 18C6 capped Co_xS_y nanoparticles synthesized at 50 (B) and 95 °C (C). Table 5.3 summarizes the FT-IR spectra of pristine 18C6 and 18C6 capped Co_xS_y nanoparticles synthesized at 50 and 95 °C. 18C6 is bound to the surface of Co_xS_y nanoparticles via the lone pairs of its C-O group, as the peak for this functional group is absent in the spectra of 18C6 capped Co_xS_y nanoparticles.

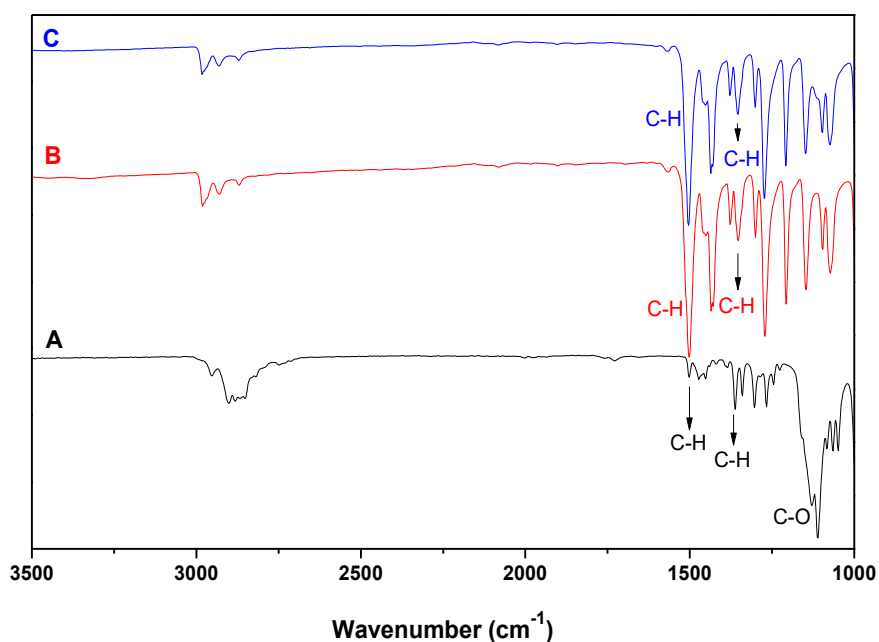


Figure 5.9: FT-IR spectra of pristine 18C6 (A) and 18C6 capped Co_xS_y nanoparticles synthesized at 50 (A) and 95 °C (B).

Table 5.3: FT-IR data of cobalt sulfide nanoparticles capped with 18C6 synthesized using SDEDTC as a sulfur source.

Compound	(C-H)	(C-H)	(C-O)
18C6	1502 cm^{-1}	1363 cm^{-1}	1135 cm^{-1}
Co_xS_y -18C6 50	1500 cm^{-1}	1352 cm^{-1}	—
Co_xS_y -18C6 95	1502 cm^{-1}	1354 cm^{-1}	—

Figure 5.10 shows the FT-IR spectra of pristine L-Carn (A) and L-Carn capped Co_xS_y nanoparticles synthesized at 50 (B) and 95 °C (C). Table 5.4 summarizes the FT-IR spectra of pristine L-Carn and L-Carn capped Co_xS_y nanoparticles synthesized at 50 and 95 °C. A shift to lower wavenumber was observed for C=O, C-C and COO^- absorption bands after introducing L-Carn to Co_xS_y nanoparticles at 50 and 95 °C. The absence of the N-H peak in the spectra of Co_xS_y capped with L-Carn synthesized either at 50 (Fig 5.11B) or 95 °C (Figure 5.10 C) signifies the interaction of L-Carn with the surface of Co_xS_y through the N-H group. The N-H group in pristine L-Carn was observed at 3237 cm^{-1} and 3049 cm^{-1} . Similar results were reported by Branham *et al.* [21] when they synthesized ruthenium (II) peptide complexes using L-carnosine.

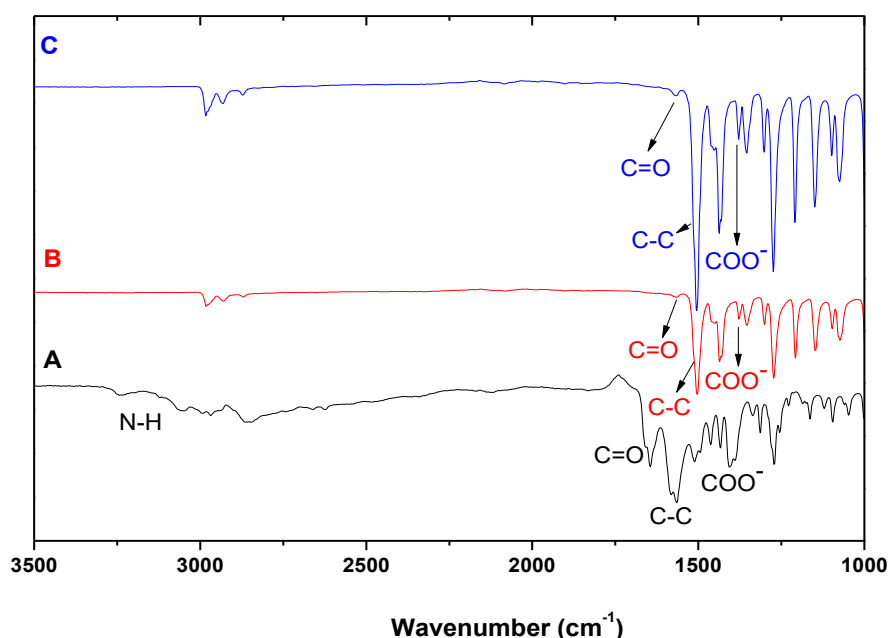


Figure 5.10: FT-IR spectra of pristine L-Carn (A) and L-Carn capped Co_xS_y nanoparticles synthesized at 50 (B) and 95 °C (C) using SDEDTC as a sulfur source.

Table 5.4: FT-IR data of cobalt sulfide nanoparticles capped with L-Carn synthesized using SDEDTC as a sulfur source.

Compound	(N-H)	(C=O)	(C-C)	(COO ⁻)
L-Carn	3237; 3049 cm ⁻¹	1705 cm ⁻¹	1570 cm ⁻¹	1404 cm ⁻¹
CoS-L-Carn 50	—	1569 cm ⁻¹	1507 cm ⁻¹	1382 cm ⁻¹
CoS- L-Carn 95	—	1564 cm ⁻¹	1503 cm ⁻¹	1373 cm ⁻¹

5.2.2 Characterization of cobalt sulfide nanoparticles synthesized using TAA as a sulfur source

In this section, Co_xS_y nanoparticles were synthesized using thioacetamide as a sulfur source. All other reaction parameters were kept constant and similar to those used in section 5.2.1.

5.2.2.1 Optical properties

All absorption spectra of Co_xS_y nanoparticles capped with GSH, TGA, 18C6 and L-Carn synthesized at 50 (Figure 5.11A) and 95 °C (Figure 5.11B) are blue shifted with respect to their bulk counterpart. The appearance of three peaks were observed when GSH and TGA were employed as capping agents, irrespective of the synthesis temperature, while only a single peak was observed in the case of Co_xS_y nanoparticles capped with 18C6 or L-Carn. However, the first peak appearing at higher energy was considered as the band gap as explained before in section 5.2.1.1. The band edge of Co_xS_y nanoparticles capped with GSH, TGA, 18C6 and L-Carn at 50 °C were estimated to be 283 nm (4.38 eV), 287 nm (4.32 eV), 263 nm (4.71 eV) and 295 nm (4.20 eV) respectively.

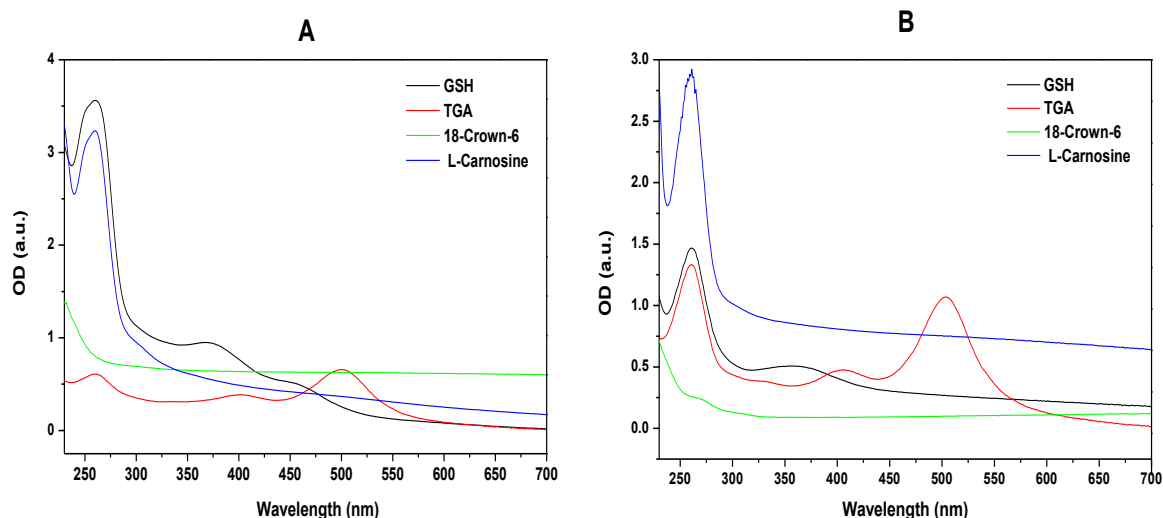


Figure 5.11: Absorption spectra of cobalt sulfide nanoparticles capped with GSH, TGA, 18C6 and L-Carn synthesized at 50 (A) and 95 °C (B) using TAA as a sulfur source.

When synthesis was conducted at 95 °C, an increase of the band edges to higher wavelength was observed with Co_xS_y nanoparticles capped by GSH, TGA, 18C6 and L-Carn moving to 298 nm (4.16 eV), 293 nm (4.23 eV), 289 nm (4.29 eV) and 299 nm (4.15 eV) respectively. This is still attributed to the temperature effect that influences the size of the nanoparticles as it is increased.

Figure 5.12 shows the photoluminescence spectra of Co_xS_y nanoparticles capped with GSH, TGA, 18C6 and L-Carn synthesized at 50 (Figure 5.12A) and 95 °C (Figure 5.12B) using TAA as a sulfur source. The spectra of Co_xS_y nanoparticles synthesized at 50 °C depict single emission peaks appearing at wavelength positions of 713 nm, 711 nm, 715 nm and 705 nm for GSH, TGA, 18C6 and L-Carn capped nanoparticles respectively. These peaks are red shifted to their respective absorption spectra (Figure 5.11A), a phenomenon attributable to the formation of nano-sized materials [22]. A shift to higher wavelength was observed in the emission spectra of Co_xS_y nanoparticles when synthesis is conducted at 95 °C. The maximum peaks have shifted from 713 to 757 nm, 711 to 748 nm, 715 to 760 nm and 705 to 740 nm for Co_xS_y nanoparticles capped with GSH, TGA, 18C6 and L-Carn respectively.

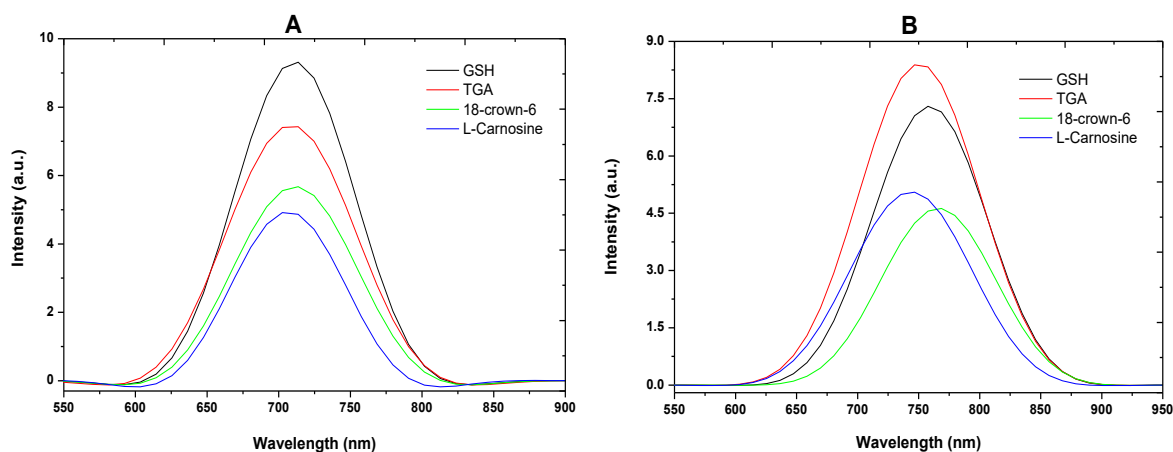


Figure 5.12: Photoluminescence spectra of cobalt sulfide nanoparticles capped with GSH, TGA, 18C6 and L-Carn synthesized at 50 (A) and 95 °C (B) using TAA as a sulfur source.

5.2.2.2 Structural Properties

Figure 5.13 shows TEM images of Co_xS_y nanoparticles capped with GSH, TGA, 18-crown-6 and L-carnosine synthesized at 50 °C with a reaction time of 1hr. Capping Co_xS_y nanoparticles with GSH (Figure 5.13A), TGA (Figure 5.13B) and 18-crown-6 (Figure 5.13C) yielded near-spherical nanoparticles with average diameters of 1.8, 8.8 and 24.7 nm respectively. However, signs of particles fusing together forming a chain-like morphology were clearly observed for TGA and 18-crown-6 capped nanoparticles. Employing L-Carn as a capping agent (Figure 5.13D) yielded the formation of nanoplates with an average diameter of 18.9 nm. Signs of aggregation were also observed as seen in the TEM image.

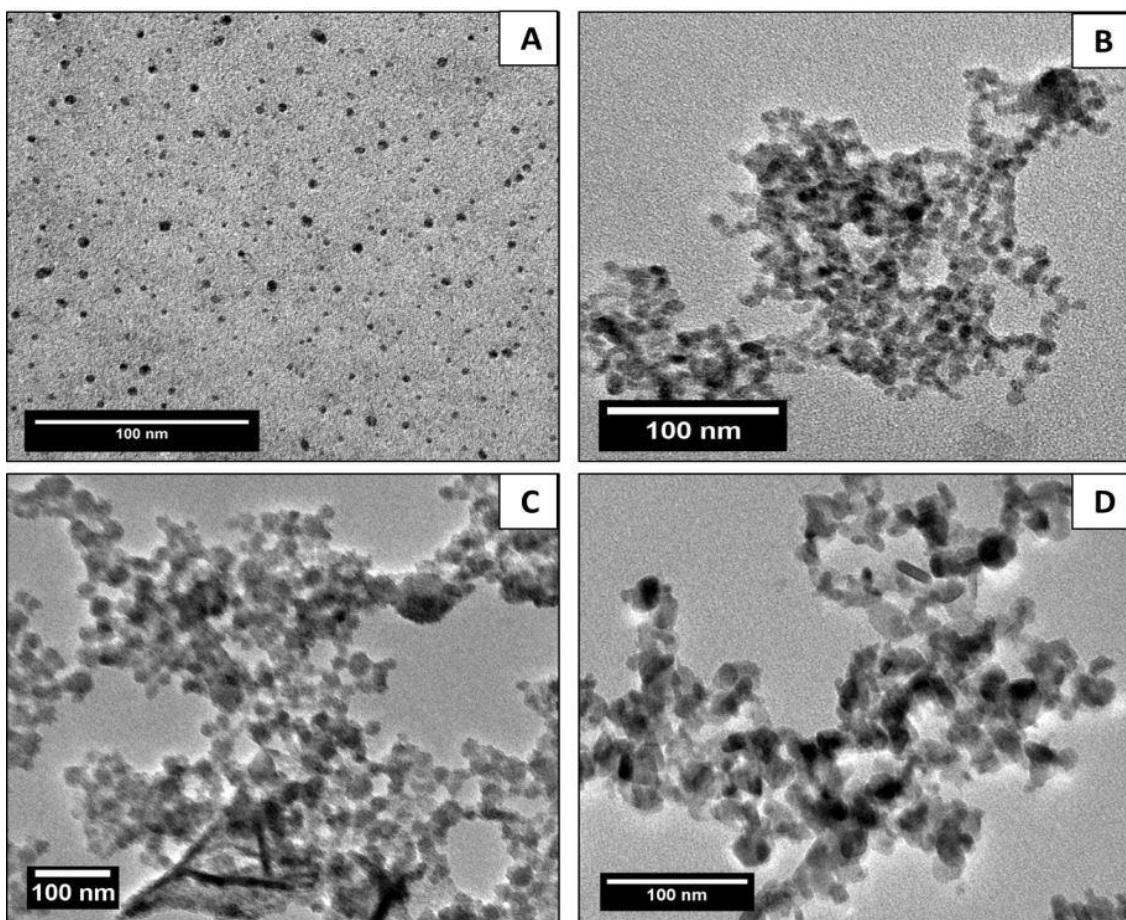


Figure 5.13: HR-TEM images of cobalt sulfide nanoparticles capped with GSH (A), TGA (B), 18C6 (C) and L-Carn (D) synthesized at 50 °C using TAA as a sulfur source.

Conducting reactions at 95 °C influenced the sizes of the particles, whereas the shape was maintained. Average diameters of 43.7 nm, 34.5 nm, 37.8 nm and 24.6 nm were measured when Co_xS_y nanoparticles are capped with GSH (Figure 5.14A), TGA (Figure 5.14B), 18C6 (Figure 5.14C) and L-Carn (Figure 5.14D) respectively. Increasing the reaction temperature resulted in the formation of bigger sized nanoparticles. Increasing the reaction temperature also affected the homogeneity of the nanoparticles sizes as was observed with GSH capped Co_xS_y nanoparticles in Figure 5.14A. Temperature has been reported as one of the parameters that contribute to nanoparticle growth; hence the nanoparticles grew bigger in size when the synthesis temperature was increased [23].

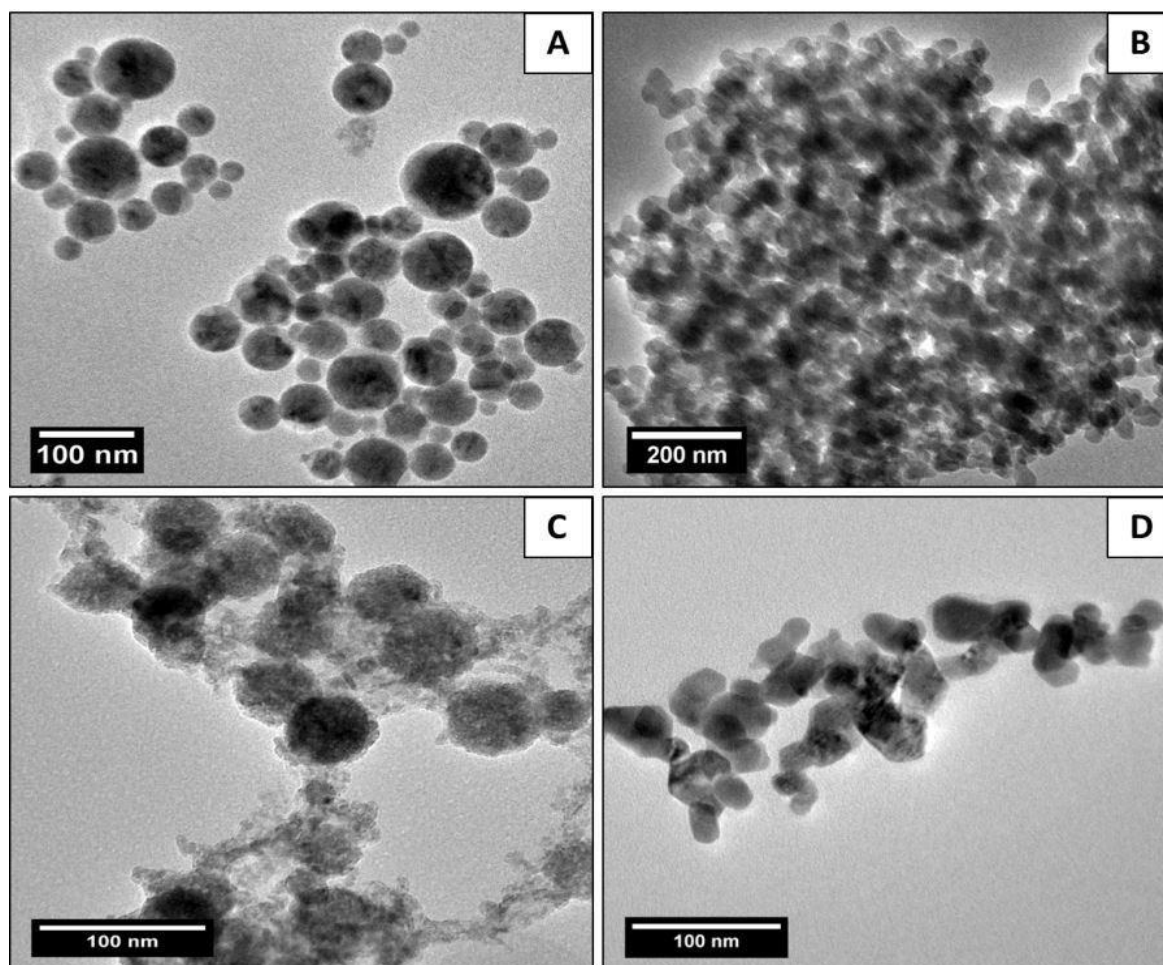


Figure 5.14: HR-TEM images of cobalt sulfide nanoparticles capped with GSH (A), TGA (B), 18C6 (C) and L-Carn (D) synthesized at 95 °C using TAA as a sulfur source.

Figures 5.15 and 5.16 show XRD patterns of Co_xS_y nanoparticles capped with GSH, TGA, 18C6 and L-Carn, synthesized at 50 and 95 °C respectively, with a reaction time of 1hr, using thioacetamide as a sulfur source. The XRD patterns obtained both at 50 and 95 °C did not show obvious peaks, signifying the synthesis of amorphous cobalt sulfide nanoparticles. Increasing the synthesis temperature to 95 °C did not improve or change the phase of as-synthesized Co_xS_y nanoparticles. Similar results were obtained by Tao *et al.* [22] when they synthesized cobalt sulfide nanoparticles using a chemical precipitation method, for use in electrochemical supercapacitors.

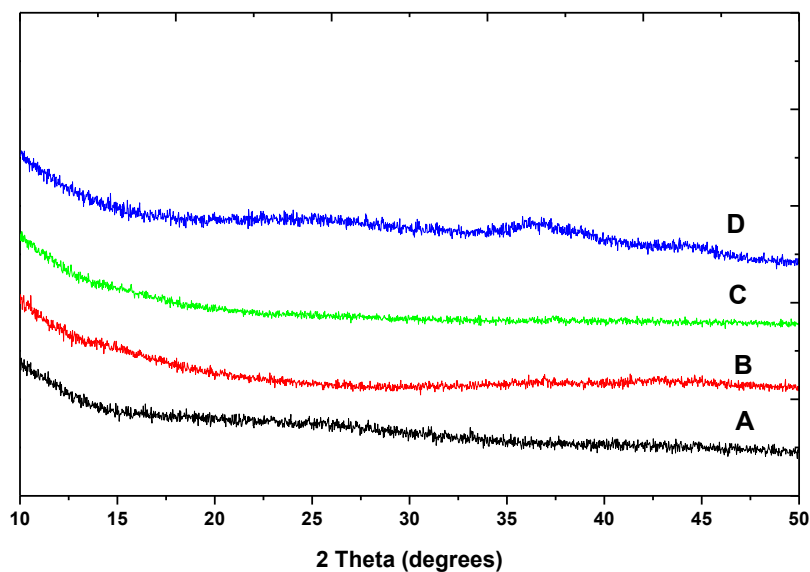


Figure 5.15: XRD spectra of cobalt sulfide nanoparticles capped with GSH (A), TGA (B), 18C6 (C) and L-Carn (D) synthesized at 50 °C using TAA as a sulfur source.

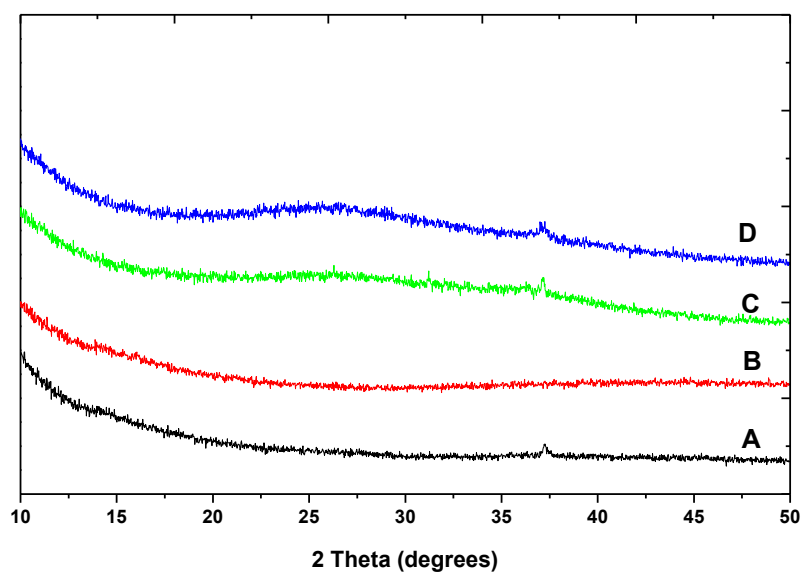


Figure 5.16: XRD spectra of cobalt sulfide nanoparticles capped with GSH (A), TGA (B), 18C6 (C) and L-Carn (D) synthesized at 95 °C using TAA as a sulfur source.

5.2.2.3 Infrared Spectra

Figure 5.17 shows the FT-IR spectra of pristine GSH (A) and GSH capped Co_xS_y nanoparticles synthesized at 50 (B) and 95 °C (C) using TAA as a sulfur source. The FT-IR spectrum of pristine GSH contains various infrared (IR) absorption bands that are characteristic to this ligand, as described in section 4.2.1.3. The FT-IR data is summarised in Table 5.5. When compared to the spectra of GSH capped Co_xS_y nanoparticles, the N-H and S-H stretches around 3331 cm^{-1} and 3234 cm^{-1} , and 2510 cm^{-1} have disappeared. This shows that GSH binds to Co_xS_y nanoparticles *via* its N-H and S-H functional groups.

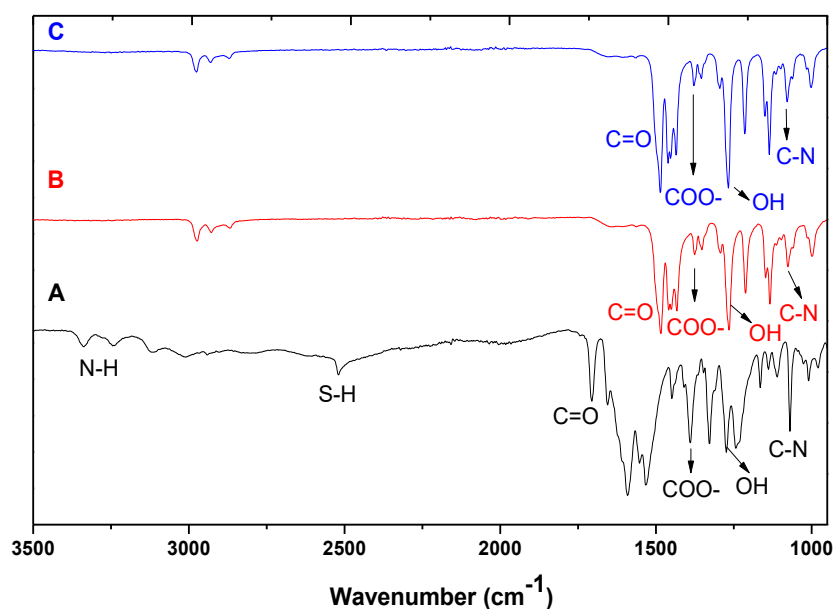


Figure 5.17: FT-IR spectra of pristine GSH (A) and GSH capped Co_xS_y nanoparticles synthesized at 50 (B) and 95 °C (C) using TAA as a sulfur source.

Table 5.5: FT-IR data of cobalt sulfide nanoparticles capped with GSH synthesized using TAA as a sulfur source.

Compound	(N-H)	(S-H)	(C=O)	(COO ⁻)	(O-H)	(C-N)
GSH	3336; 3244 cm ⁻¹	2524 cm ⁻¹	1705 cm ⁻¹	1391 cm ⁻¹	1271 cm ⁻¹	1072 cm ⁻¹
Co _x S _y -GSH 50	—	—	1485 cm ⁻¹	1386 cm ⁻¹	1265 cm ⁻¹	1076 cm ⁻¹
Co _x S _y -GSH 95	—	—	1490 cm ⁻¹	1374 cm ⁻¹	1265 cm ⁻¹	1080 cm ⁻¹

The FT-IR spectra of pristine TGA (A) and TGA capped Co_xS_y nanoparticles synthesized at 50 (B) and 95 °C (C) using TAA as a sulfur source are shown in Figure 5.18. Table 5.6 summarizes the FT-IR spectra of pristine TGA and TGA capped Co_xS_y nanoparticles synthesized at 50 and 95 °C. As shown in the table, all spectra have similar absorption bands with the exception of the S-H peak which disappeared when TGA is used as a capping ligand for Co_xS_y nanoparticles. The absence of the S-H peak is an indication that TGA is bound to the surface of Co_xS_y nanoparticles via its thiol group.

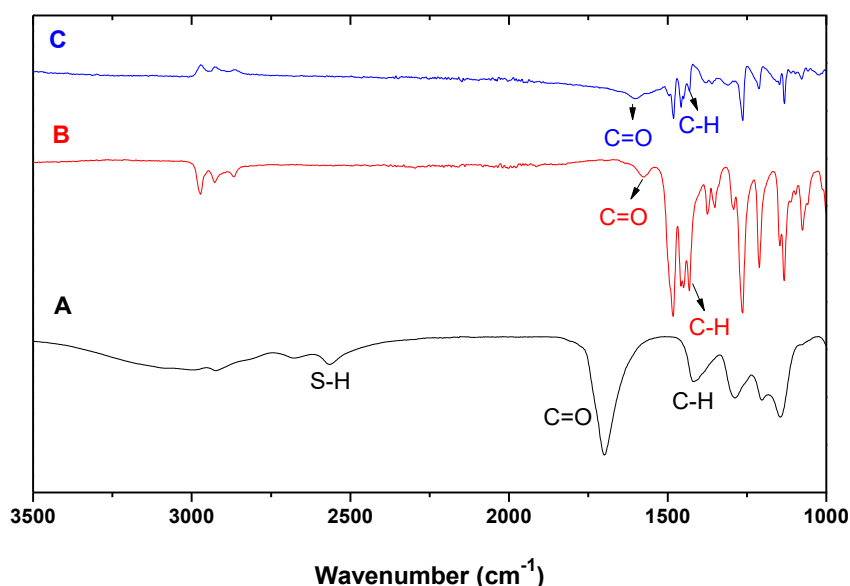


Figure 5.18: FT-IR spectra of pristine TGA (A) and TGA capped Co_xS_y nanoparticles synthesized at 50 (B) and 95 °C (C) using TAA as a sulfur source.

Table 5.6: FT-IR data of cobalt sulfide nanoparticles capped with TGA synthesized using TAA as a sulfur source.

Compound	(S-H)	(C=O)	(C-H)	(O-H)
TGA	2564 cm ⁻¹	1702 cm ⁻¹	1410 cm ⁻¹	3300 - 2900 cm ⁻¹
Co _x S _y -TGA 50	—	1589 cm ⁻¹	1453 cm ⁻¹	—
Co _x S _y -TGA 95	—	1603 cm ⁻¹	1436 cm ⁻¹	—

Figure 5.19 shows the FT-IR spectra of pristine 18-crown-6 (A) and 18-crown-6 capped Co_xS_y nanoparticles synthesized at 50 (B) and 95 °C (C) using TAA as a sulfur source. Table 5.7 summarizes the FT-IR spectra of pristine 18C6 and 18C6 capped Co_xS_y nanoparticles synthesized at 50 and 95 °C. From this data, the C-O peak disappears when 18C6 has been used to cap Co_xS_y nanoparticles. This indicates that 18C6 binds to the surface of Co_xS_y nanoparticles via the lone pairs of the C-O functional group.

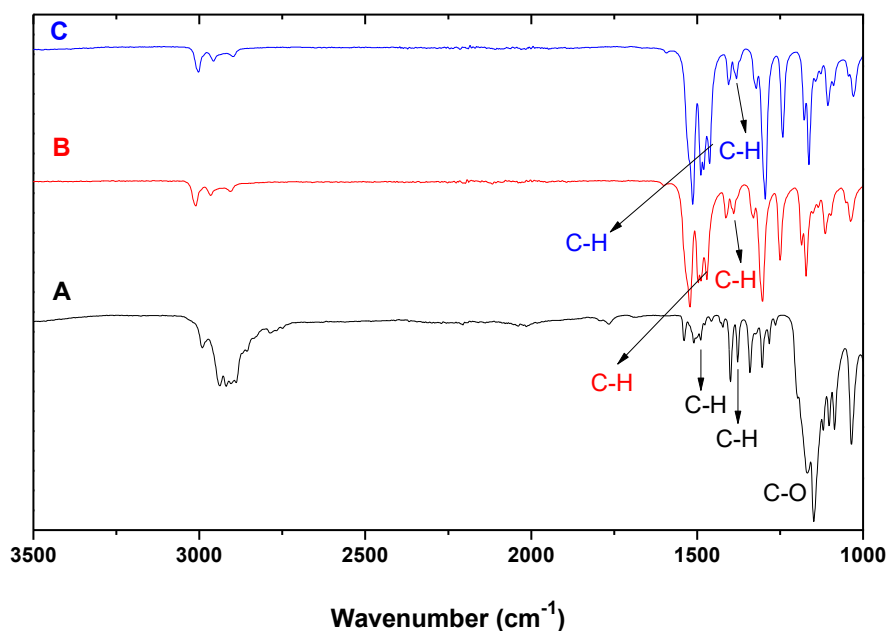


Figure 5.19: FT-IR spectra of pristine 18C6 (A) and 18C6 capped Co_xS_y nanoparticles synthesized at 50 (B) and 95 °C (C) using TAA as a sulfur source.

Table 5.7: FT-IR data of cobalt sulfide nanoparticles capped with 18C6 synthesized using TAA as a sulfur source.

Compound	(C-H)	(C-H)	(C-O)
18C6	1492 cm ⁻¹	1380 cm ⁻¹	1146 cm ⁻¹
Co_xS_y-18C6 50	1386 cm ⁻¹	1468 cm ⁻¹	—
Co_xS_y-18C6 95	1376 cm ⁻¹	1464 cm ⁻¹	—

Figure 5.20 shows the FT-IR spectra of pristine L-carnosine (A) and L-carnosine capped Co_xS_y nanoparticles synthesized at 50 (B) and 95 °C (C) using TAA as a sulfur source. Table 5.8 summarizes the FT-IR spectra of pristine L-Carn and as-synthesized L-Carn capped Co_xS_y nanoparticles. There is a change in the spectra of L-Carn when it is bound to Co_xS_y nanoparticles as indicated by the absence of the N-H peak. This signifies that L-Carn interacts with Co_xS_y nanoparticles via its amine groups.

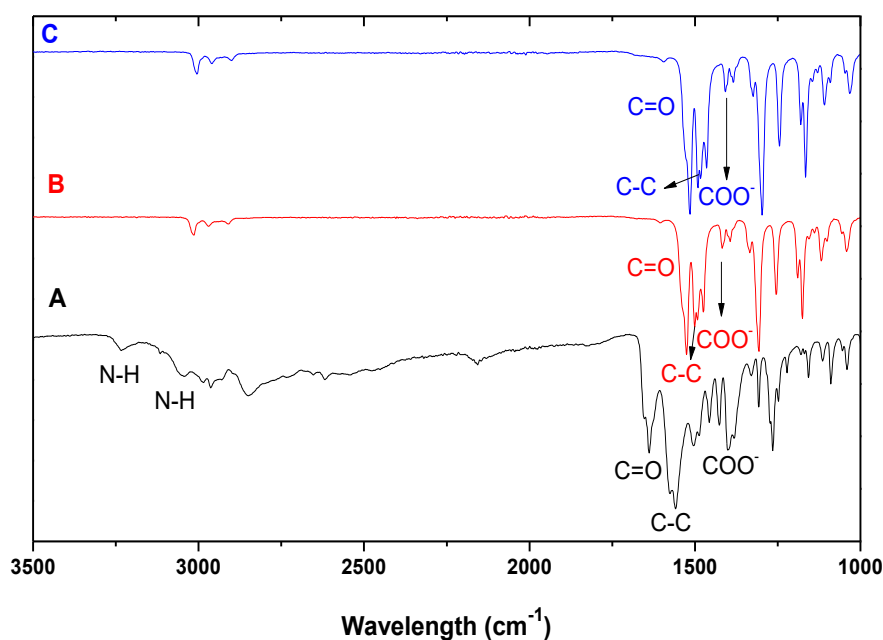


Figure 5.20: FT-IR spectra of pristine L-Carn (A) and L-Carn capped Co_xS_y nanoparticles synthesized at 50 (B) and 95 °C (C) using SDEDTC as a sulfur source.

Table 5.8: FT-IR data of cobalt sulfide nanoparticles capped with L-Carn synthesized using TAA as a sulfur source.

Compound	(N-H)	(C=O)	(C-C)	(COO ⁻)
L-Carn	3230; 3047 cm ⁻¹	1641 cm ⁻¹	1561 cm ⁻¹	1400 cm ⁻¹
Co _x S _y -L-Carn 50	—	1527 cm ⁻¹	1487 cm ⁻¹	1389 cm ⁻¹
Co _x S _y - L-Carn 95	—	1517 cm ⁻¹	1507 cm ⁻¹	1389 cm ⁻¹

5.3 Conclusions

Cobalt sulfide nanoparticles were successfully synthesized using cobaltous chloride as a copper source and two different sulfur sources, namely sodium diethyldithiocarbamate and thioacetamide. Four different capping ligands were employed, namely glutathione, thioglycolic acid, 18-crown-6 and L-carnosine. The effect of synthesis temperature on the formation of nanoparticles was investigated by conducting synthesis at two different temperatures, namely 50 and 95 °C.

The optical properties of as-synthesized nanoparticles were confirmed by UV-vis and PL. The absorption spectra displayed blue shifted excitonic peaks for all nanoparticles whereas the emission spectra showed emission peaks that red shifted to their respective absorption peaks. This is due to quantization effects which indicate the formation of Co_xS_y nanoparticles. The structural properties of as-synthesized nanoparticles were investigated using TEM and XRD. TEM revealed the formation of near-spherical and spherical shaped nanoparticles with varying diameters. Smaller sized nanoparticles were formed when synthesis was conducted at 50, and an increase in nanoparticle size was observed when the synthesis temperature was raised to 95 °C. Two phases were formed, as confirmed by XRD, when SDEDTC was used as a sulfur source. Both synthesis temperatures, 50 and 95 °C, resulted in the presence of mixed phases, *viz* face-centred cubic Co₃S₄ and cubic CoS₂. However, amorphous Co_xS_y nanoparticles were formed when TAA was used as a sulfur source.

The synthesis temperature was the contributing factor which influenced nanoparticle growth through the Ostwald ripening process, but did not influence the shape of nanoparticles. This was also evident in the absorption and emission spectra of as-synthesized nanoparticles which showed a shift to a higher wavelength (red shift) when the synthesis temperature was increased from 50 to 95 °C. The formation of different phases within one sample, as confirmed by XRD, limits the use of these nanoparticles in future applications.

5.4 References

- [1]. H. Pang, C. Wei, X. Li, G. Li, Y. Ma, S. Li, J. Chen, J. Zhang. *Sci Rep.*, **2014**, 4, 3577 – 3585.
- [2]. C. H. Lai, M. Y. Lu, L. J. Chen. *J. Mater. Chem.*, **2012**, 22, 19 – 30.
- [3]. M. R. Gao, Y. F. Xu, J. Jiang, S. H. Yu. *Chem. Soc. Rev.*, **2013**, 42, 2986 – 3017.
- [4]. F. Chen, H. Hong, S. Goel, S. A. Graves, H. Orbay, E. B. Ehlerding, S. Shi, C. P. Theuer, R. J. Nickles and W. Cai. *ACS Nano.*, **2015**, 9, 3926 – 3934.
- [5]. K. Krishnamoorthy, G. K. Veerasubramani, S. J. Kim. *Mater. Sci. Semicond. Process.*, **2015**, 40, 781 – 786.
- [6]. K. Ramasamy, W. Maneerprakorn, M. A. Malik, P. O'brien. *Phil. Trans. R. Soc. A*, **2010**, 368, 4249 – 4260.
- [7]. S. J. Bao, Y. Li, C. Ming Li, Q. Bao, Q. Lu, J. Guo. *Crystal Growth & Design.*, **2008**, 8, 3745 – 3749.
- [8]. N. Moloto, M. J. Moloto, N. J. Coville, S.S. Coville. *Journal of Nanoscience & Nanotechnology*, **2008**, 8, 6031 – 6037.
- [9]. H. Emadi, M. S. Niasari, F. Davar. *Polyhedron.*, **2012**, 31, 438 – 442.
- [10]. M. B. Muradov, O. O. Balayeva, A. A. Azizov, A. M. Maharramov, L. R. Qahramanli, G. M. Eyvazova, Z. A. Aghamaliyev. *Infrared Physics & Technology*, **2018**, 89, 255 – 262.
- [11]. M. Okajima, T. T. Ohda. *J. Cryst. Growth.*, **1992**, 117, 810.
- [12]. N. Moloto, “Synthesis, Properties and Applications of Mn, Co, Ni and Cu Chalcogenide Nanoparticles”, PhD Thesis, **2010**, Wits University, viewed on 12 June 2017.
- [13]. I. Chakraborty, S. P. Moulik. *J. Surface Sci. Technol.*, **2005**, 21, 195 – 204.

- [14]. C. Wu, S. H. Yu, S. Chen, G. Liu, B. Liu. *J. Mater. Chem.*, **2006**, 16, 3326.
- [15]. H. Zho, Y. Z. Zhang, Z. B. Yuan, *Analyst*, **2001**, 126, 358 – 360.
- [16]. I. L. Soroka, N. V. Tarakina, P. A. Korzhavyi, V. Stepanenko, M. Jonsson. *Cryst. Eng. Comm.*, **2013**, 15, 8450 – 8460.
- [17]. G. Huang, T. Chen, Z. Wang, K. Chang, W. Chen. *Journal of Power Sources*.**2013**, 235, 122 – 128.
- [18]. S. K. Balavandy, K. Shameli, D. R. B. A. Biak, Z. Z. Abidin. *Chemistry Central Journal.*, **2014**, 8, 1 – 10.
- [19]. C. I. L. Santos, M. S. Carvalho, E. Raphael, C. Dantas, J. L. Ferrari, M. A. Schiavon. *Materials Research*.**2016**, 19, 1407 – 1416.
- [20]. A. E. Vikraman, A. R. Jose, M. Jacob, K. G. Kumar. *Anal.Methods.*, 2015, 1 – 9.
- [21]. M. L. Branham, P. Singh, K. Bisetty, M. Sabela, T. Govender. *Molecules*.**2011**, 16, 10269 – 10291.
- [22]. M. Xia, C. Liu, Z. Zhao, J. Wang, C. Lin, Y. Xu, J. Heo, S. Dai, J. Han, X. Zhao. *Sci. Rep 7.*, **2017**, 1 – 9.
- [23]. S. B. Sibokoza, M. J. Moloto, N. Moloto, P. N. Sibiya. *Chalcogenide Lett.*, **2017**, 14, 69 – 78.
- [24]. F. Tao, Y. Q. Zhao, G. Q. Zhang, H. L. Li. *Electrochem. Commun.*, **2007**, 9, 1282 – 1287.

Chapter 6: Toxicity Assessment of as-synthesized Copper and Cobalt Sulfide Nanoparticles

6.1 Introduction

Nanomaterials have been shown to possess unique properties that are useful in unlocking important biological insights and thereby improve key processes in clinical diagnostics and therapeutic applications. However, the use of nanomaterials in such areas has been restricted by their potential toxic effects which have become a major concern recently [1]. Nanomaterials need to be biocompatible before they can be used in biological applications. Biocompatibility of nanomaterials determines their suitability for use in such biological assays, as they can be detrimental to biological form [2].

This involves both the solubility of these nanomaterials in aqueous or biological media and their toxicity at cellular level (cytotoxicity). Since the emergence of nanomaterials as highly efficient tools for biological analysis, nanoparticle toxicity has been a topic of interest sparked with numerous debates that have led to the establishment of a new platform termed “Nanotoxicology” [3, 4].

Nanoparticle toxicity is entirely dependent on the physicochemical properties of these nanomaterials together with environmental factors, and as individual types of nanoparticles contain their own unique properties, biocompatibility or toxicity is expected to vary amongst different types of nanomaterials [5]. These properties include the size, charge, concentration, outer coating bioactivity, and oxidative, photolytic, and mechanical stability [6 - 10].

Nanoparticle toxicity has been investigated in numerous *in vitro* and *in vivo* assays which monitor cell growth, cell viability and DNA damage in response to treatment with nanoparticles. It has been reported that nanomaterials induce cytotoxicity by compromising the integrity of the plasma membrane, mitochondrion and nucleus. This therefore initiates the process of apoptosis which further results in cell death [11 - 13]. Nanoparticles become toxic by releasing free ions into surrounding media when the layer of the capping ligand is fragmented. For example, in the case of cadmium based nanomaterials, cytotoxicity is correlated with the release of free Cd^{2+} ions due to the weakening of the quantum dot lattice

or upon degradation, due to photosensitization [14]. This results in the disturbance of the oxidative balance of the cell, which further leads to the production of reactive oxygen species (ROS) such as superoxide (O_2^-), hydroxyl radicals (HO^\cdot), peroxide radicals (ROO^\cdot) and hydrogen peroxide (H_2O_2). [15 – 17]. Therefore, it has been reported that toxicity can be circumvented through the use of an appropriate capping ligand, which will bind strongly to the surface of nanoparticles for an extended period of time and will not disintegrate. The capping ligand will thus form a protective layer around the nanoparticles which will limit the access of light and oxygen to the core surface and hence prevent oxidation [18].

In this chapter the cytotoxicity profiles of various copper sulfide and cobalt sulfide nanoparticles synthesized in Chapters 4 and 5 are reported. The cytotoxicity of as-synthesized nanoparticles was tested *in vitro* using MT-4 cells cultured in DMEM media, using protocol outlined in Chapter 3.

6.2 Results and Discussion

6.2.1 Toxicity studies of Copper sulfide nanoparticles

6.2.1.1 Cytotoxicity of Cu_xS_y nanoparticles synthesized using SDEDTC as a sulfur source

Cytotoxicity and biocompatibility of nanomaterials is of utmost importance, especially if nanomaterials are to be used in biological applications. Although these nanomaterials have shown great potential for use in biological applications, their cytotoxicity may restrict their use. The MTS assay was used to evaluate the cytotoxicity of as synthesized Cu_xS_y nanoparticles *in vitro* using MT-4 mammalian cells. Toxicity was evaluated by determining the viability of MT-4 cells treated with various concentrations of Cu_xS_y nanoparticles. Figures 6.1 and 6.2 show the cytotoxicity profiles of Cu_xS_y nanoparticles synthesized at 50 and 95 °C respectively, using SDEDTC as a sulfur source.

As shown in Figure 6.1, Cu_xS_y nanoparticles synthesized at 50 °C inhibit cell proliferation in a dose dependant manner. At lower nanoparticle concentrations (below 3 μ g/ml), Cu_xS_y nanoparticles did not show signs of toxicity as the cell viability remained comparable to that

of control cells (0 $\mu\text{g/ml}$). However, when the concentration of nanoparticles was increased (beyond 3 $\mu\text{g/ml}$), a significant drop in cell viability was observed signifying an increase in cell death due to the presence of nanoparticles. However, cells continued to grow when treated with GSH capped nanoparticles. A similar trend was reported by Ding *et al.* [19] where they tested the cytotoxicity of PEGylated Cu_xS_y nanoparticles for use in imaging of tumour cells. They observed that Cu_xS_y nanoparticles were not toxic at concentrations below 3 $\mu\text{g/ml}$ and only induced cell death when the concentration of nanoparticles was increased to 5 mg/l and higher, but cell viability was still maintained above 40%.

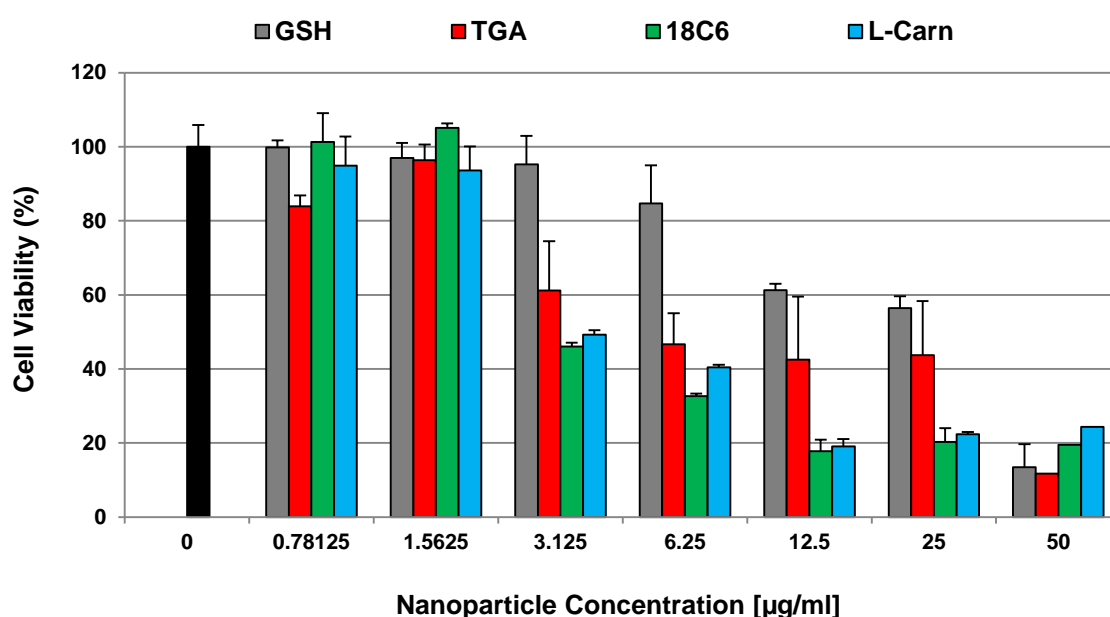


Figure 6.1: The cytotoxicity profiles of copper sulfide nanoparticles capped with GSH, TGA, 18C6 and L-Carn synthesized at 50 $^{\circ}\text{C}$ using SDEDTC as a sulfur source. The values are represented as the mean \pm standard deviation, $n = 3$. Error bars indicate the standard deviation.

Similar results were obtained with Cu_xS_y nanoparticles synthesized at 95 $^{\circ}\text{C}$, as shown in Figure 6.2. A decrease in cell viability was observed in a concentration dependant manner. Cell viability was maintained above 85% at low nanoparticle concentrations, and decline in cell viability was observed when nanoparticle concentration exceeded 6 $\mu\text{g/ml}$. However, this was not the case with GSH capped Cu_xS_y nanoparticles which maintained high cell viability even at high nanoparticle concentrations.

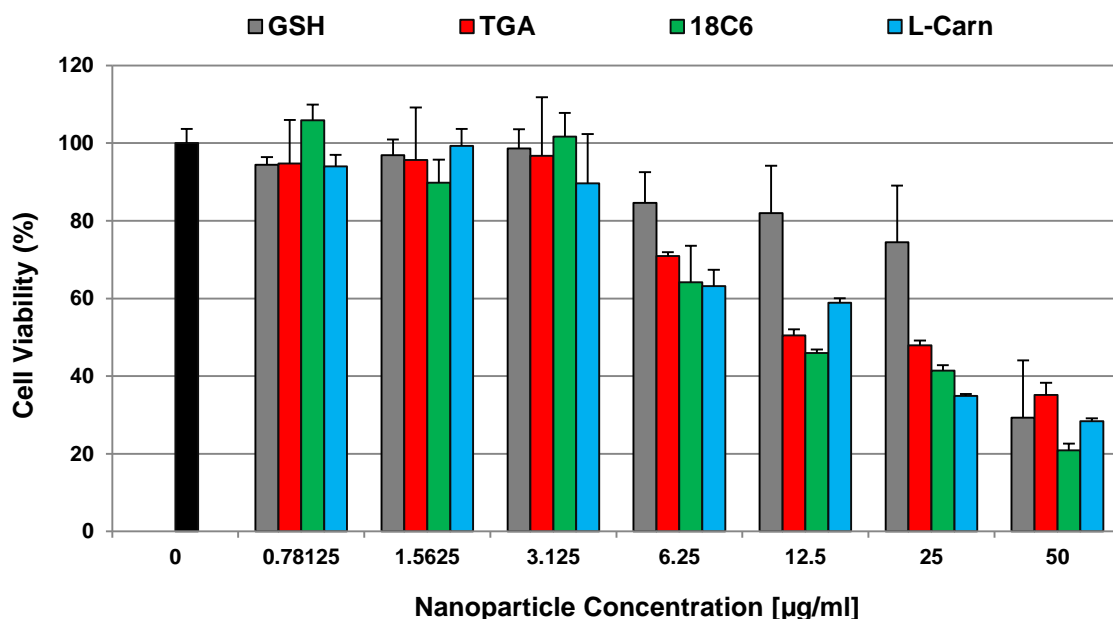


Figure 6.2: The cytotoxicity profiles of copper sulfide nanoparticles capped with GSH, TGA, 18C6 and L-Carn synthesized at 95 °C using SDEDTC as a sulfur source. The values are represented as the mean \pm standard deviation, $n = 3$. Error bars indicate the standard deviation.

6.2.1.2 Cytotoxicity of Cu_xS_y nanoparticles synthesized using TAA as a sulfur source

The toxicity of Cu_xS_y nanoparticles synthesized using TAA as a sulfur source was investigated. Figures 6.3 and 6.4 show the cytotoxicity studies of Cu_xS_y nanoparticles synthesized at 50 and 95 °C respectively, using TAA as a sulfur source.

Cu_xS_y nanoparticles synthesized at both 50 and 95 °C show moderate toxicity and have maintained high cell viabilities even at high nanoparticle concentrations. GSH and TGA capped Cu_xS_y nanoparticles showed very little signs of toxicity at 50 °C whereas 18C6 and L-Carn capped Cu_xS_y nanoparticles were able to reduce cell viability to below 40 % at concentrations exceeding 12.5 µg/ml. This decline might be due to the presence of small spherical and rod-like nanoparticles in 18C6 and L-Carn capped Cu_xS_y , which are known to induce cell death. However, for nanoparticles synthesized at 95 °C GSH and TGA capped Cu_xS_y nanoparticles showed a higher decline in cell viability.

Cu_xS_y nanoparticles synthesized using TAA as a sulfur source were less toxic when compared to Cu_xS_y nanoparticles synthesized using SDEDTC. This might be due to the size difference in the nanoparticles, as seen in chapter 4. Nanoparticles synthesized using SDEDTC are smaller in size compared to those synthesized using TAA, and are thus much more toxic since they are able to cross the nuclear membrane and cause damage to the nuclear material of the cells. This is in agreement with the findings made by Sahu *et al.* who reported that nano-sized ZnO materials exhibited a higher toxicity profile compared to micron sized ZnO materials when tested on THP-1 cells [20].

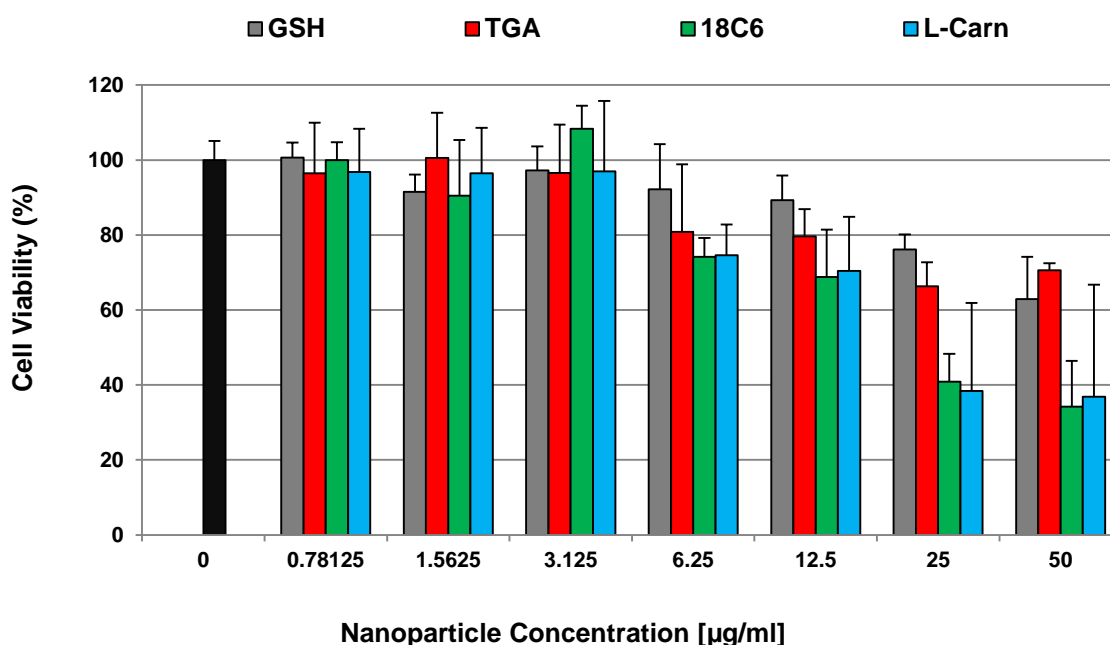


Figure 6.3: The cytotoxicity profiles of copper sulfide nanoparticles capped with GSH, TGA, 18C6 and L-Carn synthesized at 50 °C using TAA as a sulfur source. The values are represented as the mean ± standard deviation, n = 3. Error bars indicate the standard deviation.

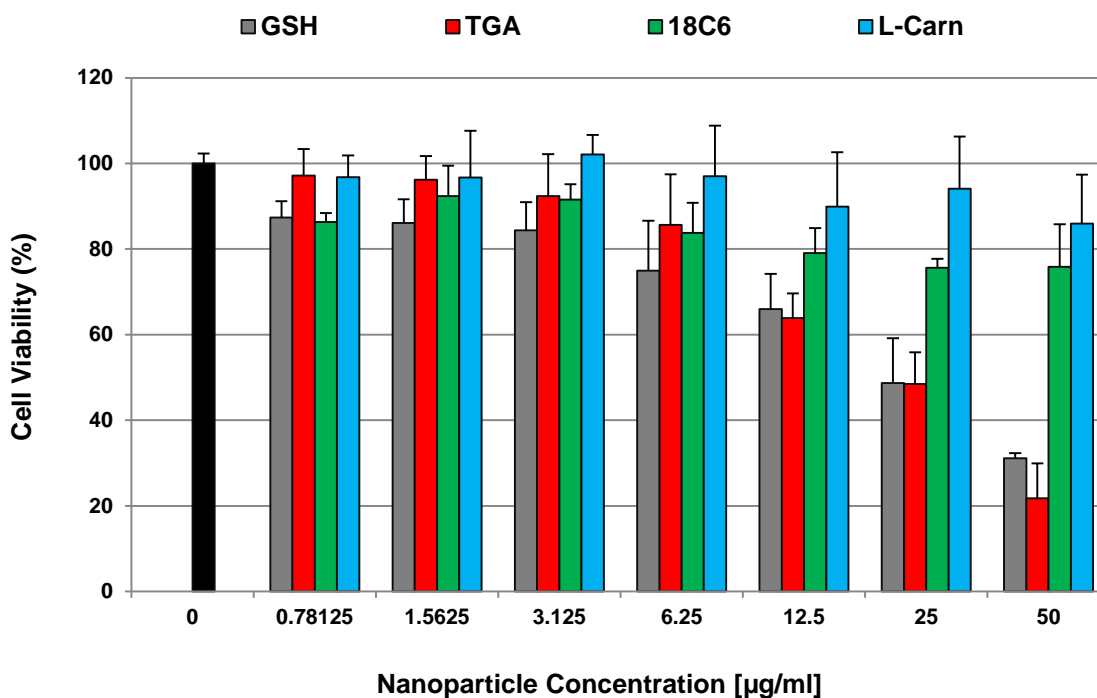


Figure 6.4: The cytotoxicity profiles of copper sulfide nanoparticles capped with GSH, TGA, 18C6 and L-Carn synthesized at 95 °C using TAA as a sulfur source. The values are represented as the mean \pm standard deviation, $n = 3$. Error bars indicate the standard deviation.

6.2.2 Toxicity Studies of Cobalt Sulfide Nanoparticles

6.2.2.1 Cytotoxicity of Co_xS_y nanoparticles synthesized using SDEDTC as a sulfur source

The toxicity of as-synthesized cobalt sulfide nanoparticles was investigated using the MTS assay as explained in chapter 3. Figures 6.5 and 6.6 show the cytotoxicity of Co_xS_y nanoparticles synthesized at 50 and 95 °C respectively tested using MT-4 cells. Co_xS_y nanoparticles synthesized at both 50 and 95 °C show very little signs of toxicity as the cell viability of treated MT-4 cells remained high and almost equivalent to that of untreated cells. A negligible drop in cell viability was observed as the concentration of Co_xS_y nanoparticles is increased, but cell viability is still maintained above 75% even at the highest concentration, which is 50 µg/ml. Cobalt and cobalt containing nanomaterials such as cobalt nanoparticles

or cobalt oxide nanoparticles are known to be toxic, but this can be circumvented by the use of biocompatible capping ligands that encapsulate cobalt containing nanomaterials and prevent the exposure of cobalt to surrounding media thereby improving their toxicity [21].

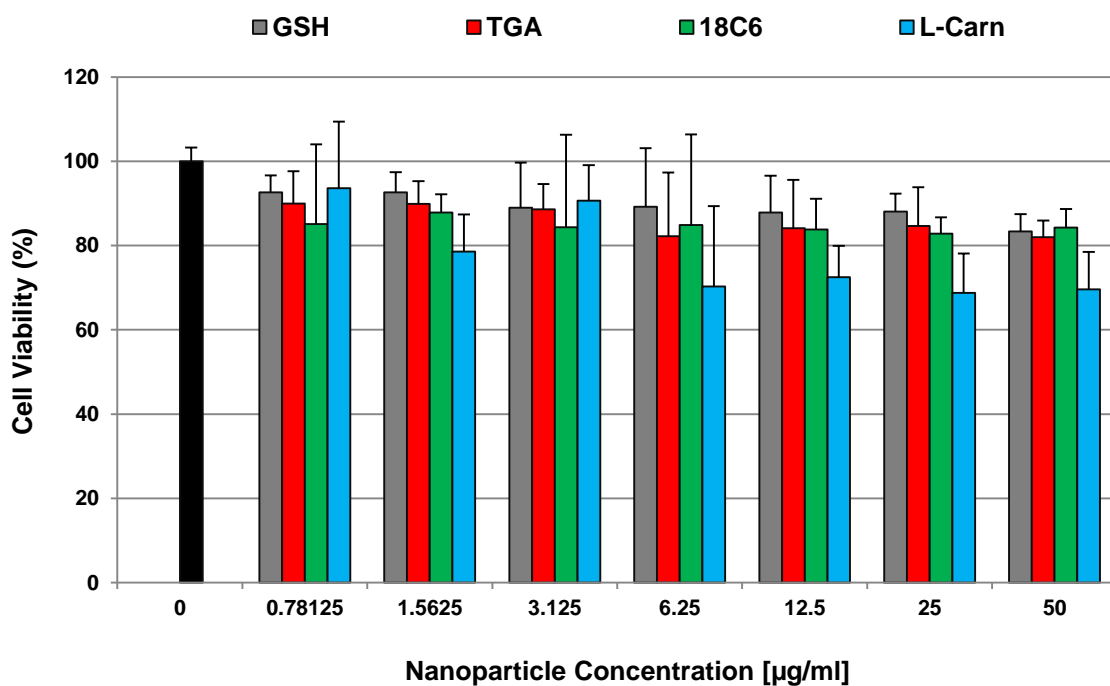


Figure 6.5: The cytotoxicity profiles of cobalt sulfide nanoparticles capped with GSH, TGA, 18C6 and L-Carn synthesized at 50 °C using SDEDTC as a sulfur source. The values are represented as the mean \pm standard deviation, $n = 3$. Error bars indicate the standard deviation.

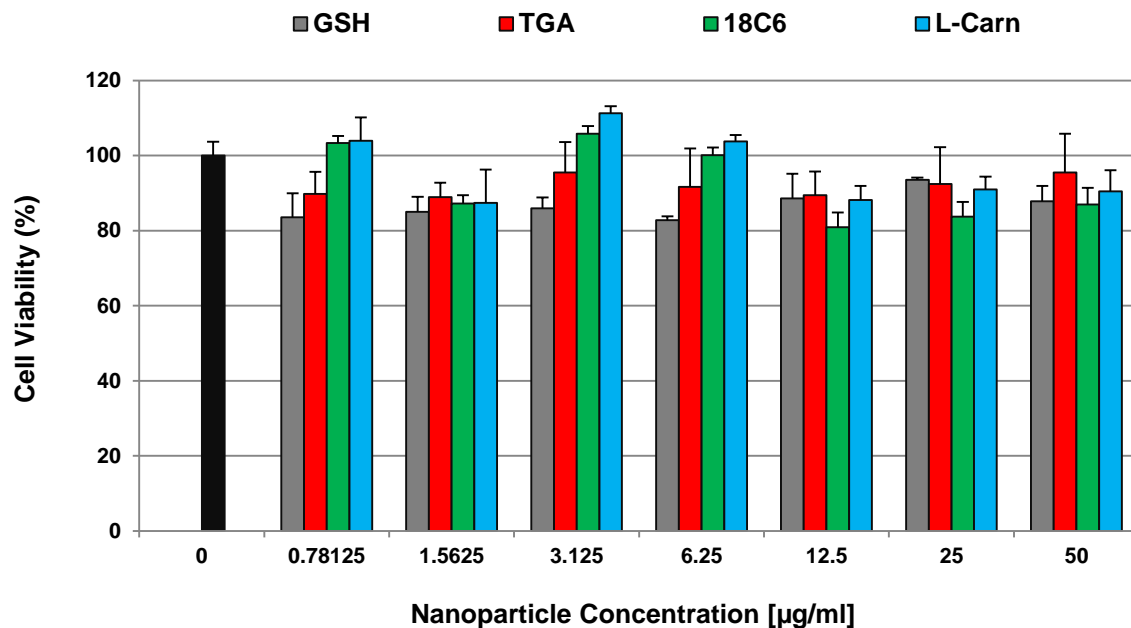


Figure 6.6: The cytotoxicity profiles of cobalt sulfide nanoparticles capped with GSH, TGA, 18C6 and L-Carn synthesized at 95 °C using SDEDTC as a sulfur source. The values are represented as the mean \pm standard deviation, $n = 3$. Error bars indicate the standard deviation.

6.2.2.2 Cytotoxicity of Co_xS_y nanoparticles synthesized using TAA as a sulfur source

The cytotoxic effects of Co_xS_y nanoparticles synthesized using TAA as a sulfur source were also investigated. Figures 6.7 and 6.8 show cytotoxic profiles of Co_xS_y nanoparticles synthesized at 50 and 95 °C respectively, using TAA as a sulfur source. Nanoparticles synthesized at 50 °C (Figure 6.7) display little signs of toxicity across the entire concentration range, with cell viability maintained above 80% even at the highest concentration. However, 18C6 capped Co_xS_y nanoparticles showed increased cytotoxicity at 50 µg/ml, and reduced cell viability to below 20%.

The same was observed with nanoparticles synthesized at 95 °C (Figure 6.8). These nanoparticles show no signs of toxicity towards MT-4 cells, as the viability of cells treated with nanoparticles is comparable to that of untreated cells (0 µg/ml). The viability of treated cells decreases slightly in a dose dependant manner, but still remains above 70% even at the

highest concentration. However, TGA, 18C6 and L-Carn capped Co_xS_y nanoparticles were toxic at 50 $\mu\text{g/ml}$, and the viability of MT-4 cells dropped to below 25%.

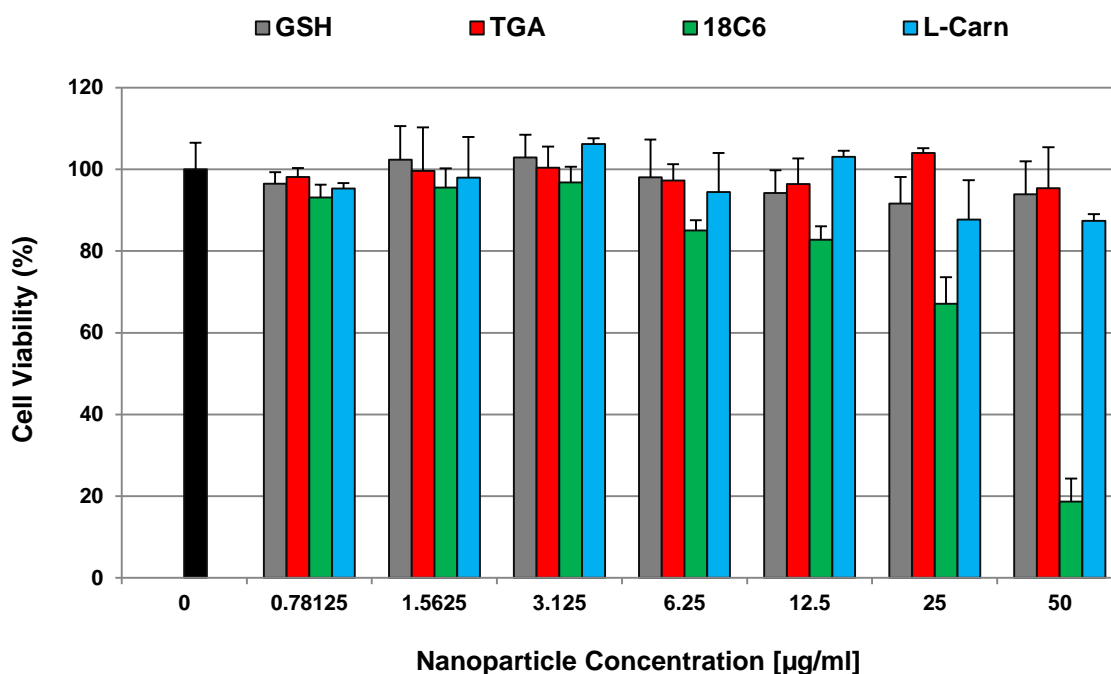


Figure 6.7: The cytotoxicity profiles of cobalt sulfide nanoparticles capped with GSH, TGA, 18C6 and L-Carn synthesized at 50 °C using TAA as a sulfur source. The values are represented as the mean \pm standard deviation, $n = 3$. Error bars indicate the standard deviation.

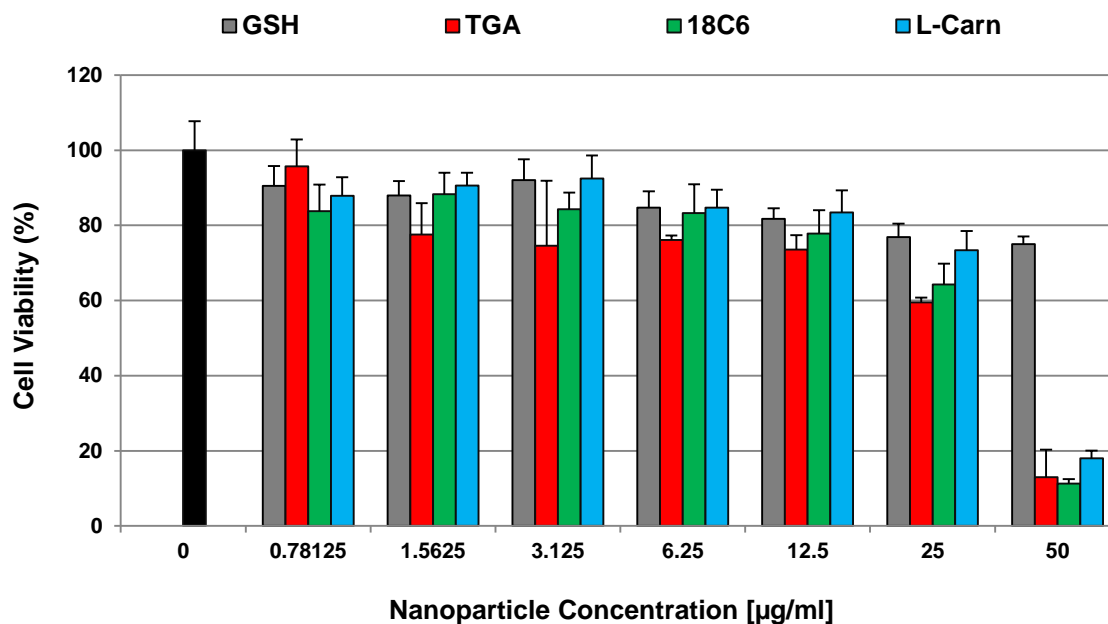


Figure 6.8: The cytotoxicity profiles of cobalt sulfide nanoparticles capped with GSH, TGA, 18C6 and L-Carn synthesized at 95 °C using TAA as a sulfur source. The values are represented as the mean \pm standard deviation, $n = 3$. Error bars indicate the standard deviation.

6.3 Conclusion

The cytotoxic profiles of as-synthesized nanoparticles were investigated in order to screen nanoparticles better suited for use as fluorophores to synthesize fluorescent probes for imaging of cellular material *in vitro*. Cu_xS_y nanoparticles exhibited a moderate, concentration dependant toxicity, which increased with an increase in nanoparticle concentration. For nanoparticles synthesized using SDEDTC as a sulfur source, a significant decline in cell viability was seen when nanoparticle concentration exceeded 3.125 $\mu\text{g/ml}$, except for GSH capped Cu_xS_y nanoparticles which did not show signs of toxicity. Cu_xS_y nanoparticles synthesized using TAA as a sulfur source showed a similar trend. However, these were seen to be less toxic compared to nanoparticles synthesized using SDEDTC, due to size differences.

Co_xS_y nanoparticles also showed a dose dependant toxicity profile, with cell viability decreasing slightly with an increase in nanoparticle concentration. Almost all Co_xS_y nanoparticles tested showed very little signs of toxicity. This could be attributed to the capping ligands completely encapsulating the nanoparticles and also to their bigger sizes. The use of biocompatible capping ligands protects the nanoparticles and prevents cobalt ions from leaching out. Nanoparticle toxicity is usually due to improper passivation of the nanoparticles by the capping ligands which results in the leaching of the core material from the nanoparticles into the cells. The accumulation of cobalt or copper ions disrupts the oxidative balance of the cells, which further leads to the production of reactive oxygen species such as superoxides (O_2^-) and hydroxyl radicals (HO^\cdot) [22]. Nanoparticles that are bigger in size have a low uptake efficiency as the cells struggle to internalise materials that exceed 25 nm in size.

Overall, as-synthesized Cu_xS_y and Co_xS_y nanoparticles are suitable for use in biological applications *in vitro*, however Cu_xS_y nanoparticles synthesized using SDEDTC should be used at moderate concentrations. The use of biocompatible capping ligands played a major role in reducing nanoparticle toxicity. Further studies are required to investigate the interaction of nanoparticles with cellular material to learn the mechanism of toxicity. For example, a method that tracks the uptake of nanomaterials into cells during toxicity testing should be followed to ensure that nanomaterials are not declared as non-toxic whereas they were not internalised by the cells due to aggregation.

6.4 References

- [1]. N. Chen, Y. He, Y. Su, X. Li, Q. Huang, H. Wang, X. Zhang, R. Tai, C. Fan. *Biomaterials*, **2012**, 33, 1238 – 1244.
- [2]. M. Bottrill, M. Green. *Chem. Commun.*, **2011**, 47, 7039 – 7050.
- [3]. O. Gladkovskaya, P. Greaney, Y. K. Gun'ko, G. M. O'Connor, M. Meere, Y. Rochev. *Toxicol. Res.*, **2015**, 4, 1409 – 1415.
- [4]. P. C. Ray, H. Yu, P. P. Fu. *J. Environ. Sci. Health C. Environ. Carcinog. Ecotoxicol. Rev.*, **2009**, 27, 1 – 35.
- [5]. R. Hardman. *Environ. Health Perspect.*, **2006**, 114, 165 – 172.
- [6]. K. M. Tsoi, Q. Dai, B. A. Alman, W. C. W. Chan. *Acc. Chem. Res.*, **2013**, 46, 672 – 680.
- [7]. F. Ahmad, A. K. Pandey, A. B. Herzog, J. B. Rose, C. P. Gerba, S. A. Hashsham. *J Nanopart Res.*, **2012**, 14, 1038 – 1063.
- [8]. Y. Wang, R. Hu, G. Lin, I. Roy, K-T. Yong. *ACS Appl. Mater. Interfaces.*, **2013**, 5, 2786 – 2799.
- [9]. J. Lovric, H. S. Bazzi, Y. Cuie, G. R. Fortin, F. M. Winnik, D. Maysinger. *J Mol Med (Berl.)*, **2005**, 83, 377 - 385.
- [10]. V. V. Breus, A. Pietuch, M. Tarantola, T. Basché, A. Janshoff. *Beilstein J. Nanotechnol.*, **2015**, 6, 281 – 292.
- [11]. E. Fröhlich. *Int J Nanomedicine*, **2012**, 7, 5577 – 5591.
- [12]. G. Lin, Q. Ouyang, R. Hu, Z. Ding, J. Tian, F. Yin, G. Xu, Q. Chen, X. Wang, K-T. Yong. *Nanomed. Nanotech. Biol. Med.*, **2015**, 11, 341 – 350.

- [13]. K-T. Yong, W-C.Law, R. Hu, L. Ye, L. Liu, M. T. Swihart, P. N. Prasad. *Chem. Soc. Rev.*, **2013**, 42, 1236 – 1250.
- [14]. K. G. Li, J. T. Chen, S. S. Bai, X. Wen, S. Y. Song, Q. Yu, J. Li, Y. Q. Wang. *Toxicol. In Vitro.*, **2009**, 23, 1007 – 1013.
- [15]. Y. Xing, J. Rao. *Cancer Biomark.*, **2008**, 4, 307 – 319.
- [16]. A. M. Derfus, W. C. W. Chan, S. N. Bhatia. *Nano Lett.*, **2004**, 4, 11 – 18.
- [17]. B. O. Dabbousi, J. Rodriguezviejo, F. V. Mikulec, J. R. Heine, H. Mattoussi, R. Ober, K. F. Jensen, M. G. Bawendi. *J. Phys. Chem.B.*, **1997**, 101, 9463 – 9475.
- [18]. S. W. Kim, J. P. Zimmer, S. Ohnishi, J. B. Tracy, J. V. Frangioni, M. G. Bawendi. *J. Am. Chem. Soc.*, **2005**, 127, 10526 – 10532.
- [19]. K. Ding, J. Zeng, L. Jing, R. Qiao, C. Liu, M. Jiao, Z. Li, M. Gao. *Nanoscale.*, **2015**, 7, 11075 – 11081.
- [20]. D. Sahu, G. M. Kannan, M. Tailang, R. Vijayaraghavan. *Journal of Nanoscience*, **2016**, 2016, 1 – 9.
- [21]. P. K. Bajpai, S. Yadav, A. Tiwari, H.S. Virk. *Solid State Phenomena.*, **2015**, 222, 187 – 233.
- [21]. M. Ates, V. Demir, Z. Arslan, M. Camas, F. Celik. *Water Air Soil Pollut.*, **2016**, 227, 1 – 8.
- [22]. A. M. Derfus, W. C. W. Chan, S. N. Bhatia. *Nano Lett.*, **2004**, 4, 11 – 18.

Chapter 7: *In vitro* Imaging of cellular material using Copper Sulfide Nanoparticles

7.1 Introduction

Biological imaging has advanced significantly in the past years and has given researchers a detailed understanding of biological processes that occur at both molecular and cellular level. Nanomaterials have been the major player in this field, due to their small size and their ability to bind to specific targets when functionalised with biomolecules [1]. Quantum dots (particularly metal sulfides) are amongst the most popular nanoparticle systems to be used in such assays to enhance the performance of conventional imaging techniques. In bio-imaging applications, metal sulfides have been used as fluorophores (replacing organic dyes) in the development of fluorescent probes for imaging various cellular processes, *in vitro* [2, 3].

The use of nanomaterials as fluorophores over organic dyes was motivated by several limitations found in these dyes, which impact negatively on the sensitivity of biological assays in which they are used. Apart from suffering from fast photobleaching, organic dyes have a narrow excitation spectrum which can only be excited by a light of a specific wavelength, and this differs between different organic dyes. Also, organic dyes have broad emission spectra which in-turn limits the number of fluorescent probes that can be used to target different molecules as the spectra of different dyes might overlap [4]

The use of metal sulfides as fluorophores has grown immensely in recent years, owing to their inherent optical properties which make them suitable candidates over conventional organic dyes and other conventional fluorophores. The properties of metal sulfides include the quantum confinement motivated emission colour tunability by size, high photostability and brightness, wide absorption spectra which allows for excitation at a wide range of wavelengths, narrow emission spectra, and increased fluorescence lifetimes [5]. The narrow emission band caters for the excitation of multiple probes with a single light source [6].

The use of nanomaterials as fluorescent probes was first demonstrated by Chan and Nie [7]. They developed an immunoassay that utilised a quantum dot-IgG probe to target a polyclonal anti-IgG antibody, which was then visualised using fluorescence microscopy. Since this discovery, there has been a rise in the development of immunoassays that employ quantum dots as fluorescent reporters or probes for disease detection and imaging. Li *et al* [8] reported the use of cadmium sulfide nanoparticles as fluorescent probes in the development of an assay for the detection of ciprofloxacin, which improved the detection limit and achieved sensitivities in the microgram level. Cui and co-workers [9] used CdTe quantum dots as a fluorescent and electrochemical label in an immunosensor that detected target proteins at sensitivities as low as 0.005ng/ml. Following that, Xo and co-workers [10] demonstrated an in-vitro assay for dual imaging of two cancer biomarkers simultaneously in cancer cell lines using a peptide and an aptamer conjugated separately to quantum dots.

In this chapter we report on the use of copper sulfide nanoparticles as fluorophores in the design of fluorescent probes, for subsequent use in the imaging of mammalian cells *in vitro*. Copper sulfide nanoparticles synthesized in chapter 4 were functionalized with antibodies that bind to certain proteins in mammalian cells. Monoclonal antibodies that bind the hypoxia inducible factor (HIF-1 α) and phospho-histone (Phospho-Histone H2A.X) proteins were chosen, as these proteins are produced in abundance when cells undergo apoptosis, a process by which cells undergo programmed cell death. Cobalt sulfides were excluded from this assay since pure phases were not successfully synthesized in chapter 5. The as-synthesized cobalt sulfides were bigger in size and contained mixed phases, which might pose challenges in biological imaging.

7.2 Results and Discussion

Glutathione capped copper sulfide nanoparticles, synthesized at 50°C using SDEDTC as a sulfur source, were used to demonstrate “proof of concept” of the bio-imaging abilities of as-synthesized nanoparticles. These nanoparticles were chosen because of their small size, spherical shape and low toxicity. Spherical nanoparticles, with smaller sizes, are known to penetrate cells more efficiently than other nanoparticles with different shapes [11]. Bigger nanoparticles cannot be internalised by cells efficiently, as they are unable to pass through membranes unaided. Antibodies against the hypoxia inducible factor (HIF-1 α) and phospho-

histone (Phospho-Histone H2A.X) proteins were conjugated to as-synthesized CuS nanoparticles and used to image Hek-293 and HeLa cells expressing the aforementioned proteins.

7.2.1 Development of Fluorescent Probes

Glutathione binds to the surface of CuS nanoparticles via its thiol group and therefore leaves the carboxylic group available for conjugation with biomolecules. EDC and sulfo-NHS were employed to activate this carboxylic end, making it ready for binding of the monoclonal antibodies through the formation of an amide bond. EDC and sulfo-NHS act as cross-linkers that attach the carboxyl end of GSH to the amine group of the antibodies. The conjugation reaction was confirmed using UV-vis spectroscopy. Figure 7.1 shows the absorption spectra of bare and conjugated CuS nanoparticles. A shift to a higher wavelength was observed in the spectra of conjugated CuS nanoparticles (CuS-Mab 1 and CuS-Mab 2), signifying the attachment of antibodies to the surface of the nanoparticles. A similar shift was observed by Nghiem and colleagues [12] when they conjugated BSA to gold nanoparticles. They explained that the shift was due to changes in the dielectric properties on the surface of gold nanoparticles owing to the presence of BSA.

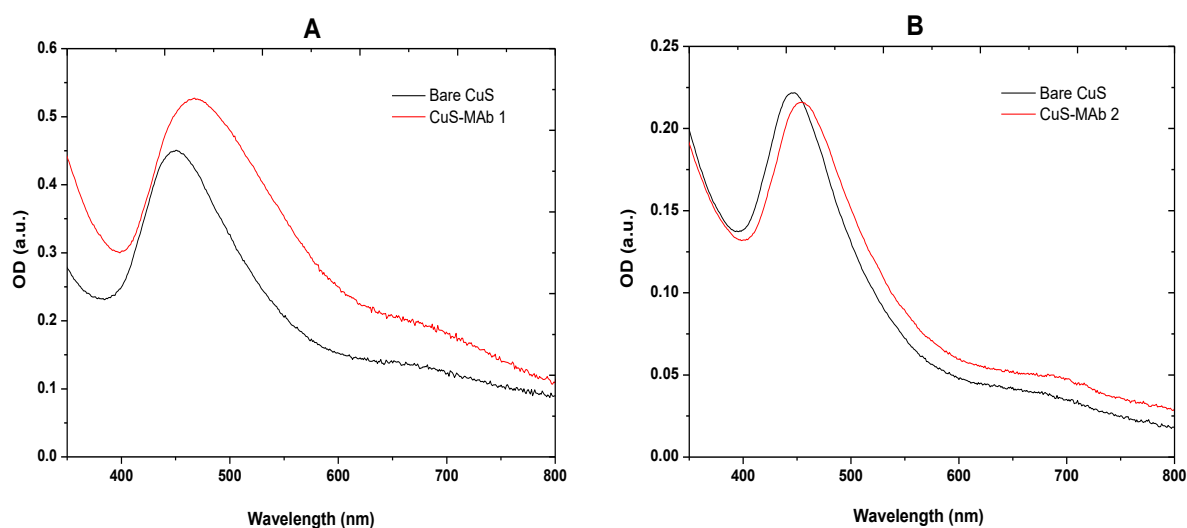


Figure 7.1: Absorption spectra of bare (A) and antibody conjugated (B) copper sulfide nanoparticles.

7.2.2 Treatment of Cells to Induce Apoptosis

Mammalian cells (Hek-293 and HeLa) were treated separately with solutions of doxorubicin and CoCl_2 for 3 and 24 hrs respectively, to stimulate apoptosis. Apoptosis is the process by which cells undergo programmed cell death, and is preceded by various biochemical and morphological changes within the cells [14]. CoCl_2 induces apoptosis by simulating hypoxia, which results in the expression of hypoxia inducible factor (HIF-1 α). Doxorubicin induces apoptosis via phosphorylation of histone transcriptional factor known as Phospho-Histone H2A.X within the cells [15].

Figures 7.2 and 7.3 show the morphology of Hek-293 and HeLa cells before and after treatment with CoCl_2 and doxorubicin. Untreated cultures (Figure 7.2A and Figure 7.3A) show healthy cells with typical Hek-293 and HeLa cell morphology, while cells from cultures treated with CoCl_2 (Figure 7.2B and 7.3B) and doxorubicin (Figure 7.2C and 7.3C) display various changes in morphology. The cells appear round and the nuclei have grown bigger. These features are typical of cells undergoing apoptosis, which is often triggered by exposure of cells to a stressful condition [16]. The treatment of cells with CoCl_2 and doxorubicin has successfully activated the apoptotic pathway resulting in the expression of HIF-1 α and the phosphorylation of H2A.X [17 - 19].

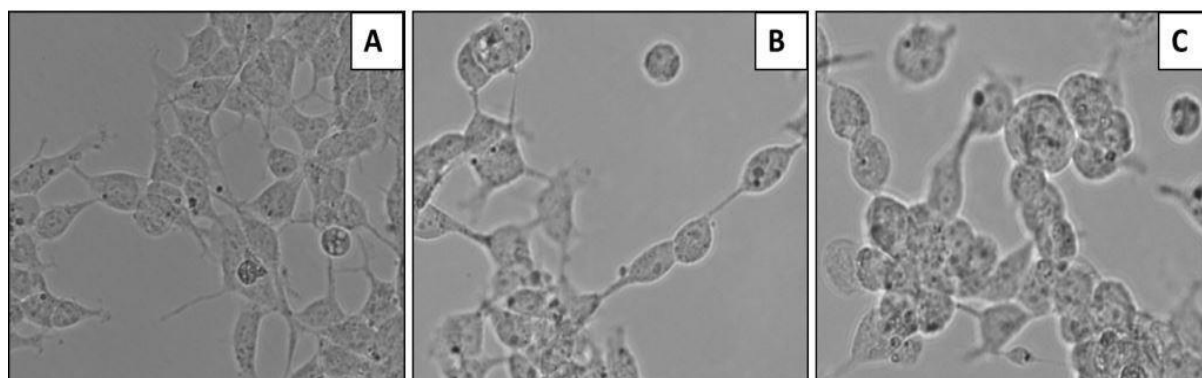


Figure 7.2: Morphology of Hek-293 cells before (A) and after treatment with CoCl_2 (B) and Doxorubicin (C) to induce hypoxia.

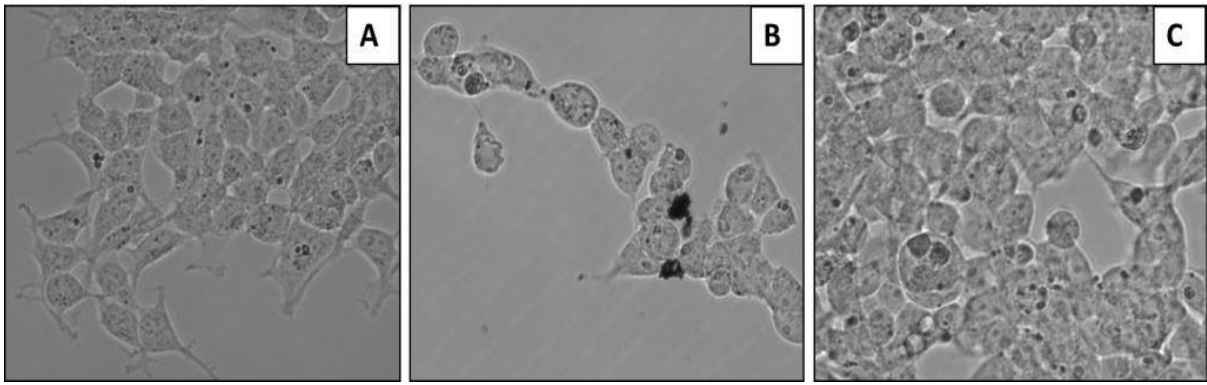


Figure 7.3: Morphology of HeLa cells before (A) and after treatment with CoCl_2 (B) and Doxorubicin (C) to induce hypoxia.

7.2.3 Imaging of Hek-293 and HeLa cells using Fluorescent Probes

After treatment, Hek-293 and HeLa cells were stained with the fluorescent probes (CuS nanoparticles conjugated with HIF-1 α and H2A.X MAbs) for imaging purposes. PBS and non-conjugated CuS nanoparticles were used as controls. Figures 7.4 and 7.5 show Hek-293 cells treated with CoCl_2 and doxorubicin respectively, after staining with PBS buffer (A, B), bare nanoparticles (C, D) and fluorescent probes (E, F). The cells were viewed under white and green light in a Fluid cell imaging station (Invitrogen). In both figures, Hek-293 cells stained with PBS only (A, B) are not visible when viewed using green light signifying their lack of fluorescence due to the absence of nanoparticles, and can only be viewed under white light. When the cells were stained with bare CuS nanoparticles (C, D), fluorescence was observed under green light. CuS nanoparticles were successfully internalised and distributed inside the cells and have allowed fluorescence imaging of these cells. However, when cells were stained with fluorescent probes (E, F), little signs of fluorescence were observed. The fluorescence intensity decreased drastically when compared to that of bare CuS nanoparticles (C, D). Also, the site at which the probes localize cannot be deduced due to the low fluorescence signal. The probes were expected to localize in the nucleus as the targeted proteins (HIF-1 α and phospho-histone) are known to accumulate in the nucleus during apoptosis [20 - 23].

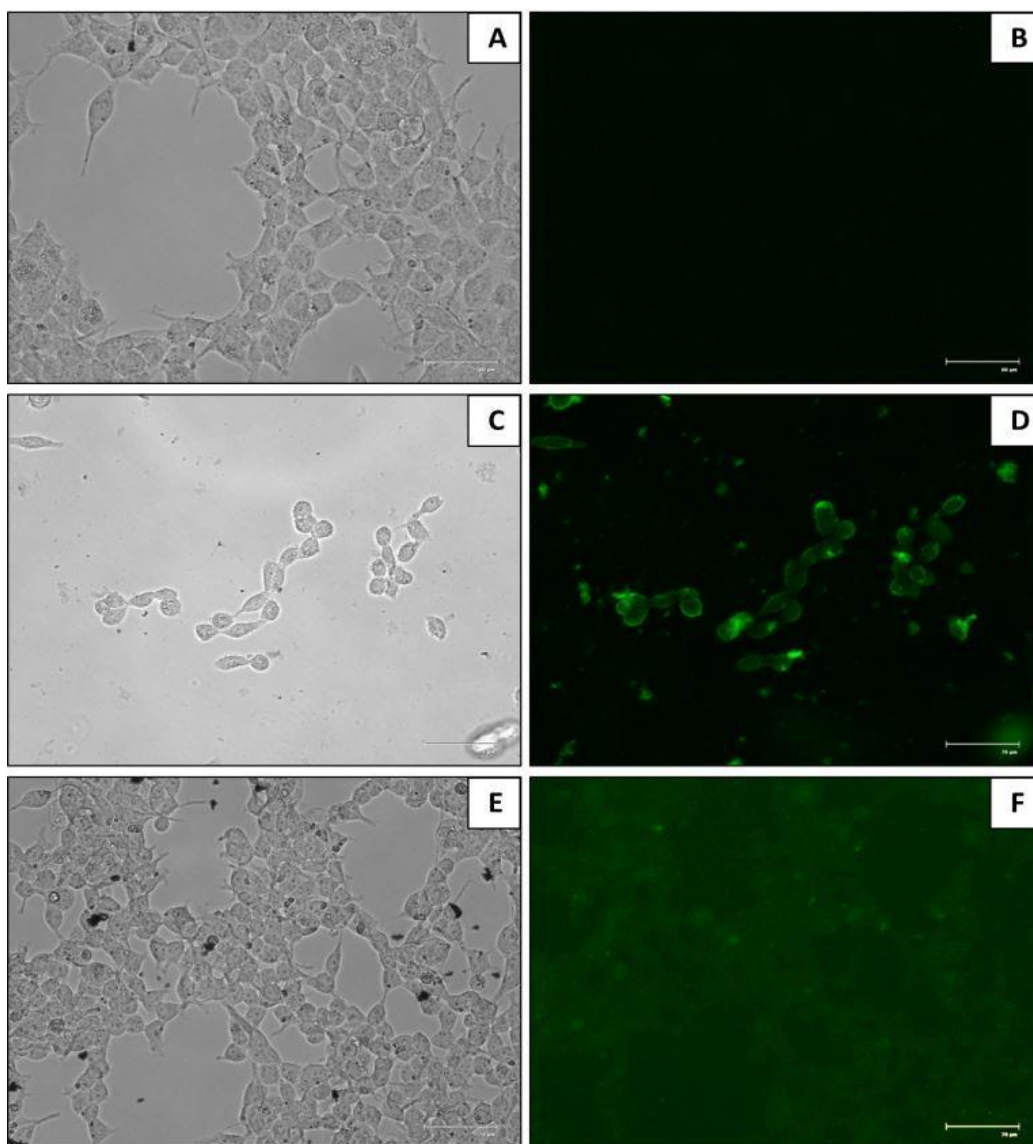


Figure 7.4: Fluorescence imaging of CoCl_2 treated Hek-293 cells stained with the CuS-HIF- 1α probe. Images A and B shows control cells (without probe) viewed under white and green light respectively. Images C and D shows cells stained with bare nanoparticles viewed under white and green light respectively. E and F shows cells stained with the fluorescent probe viewed under white and green light respectively.

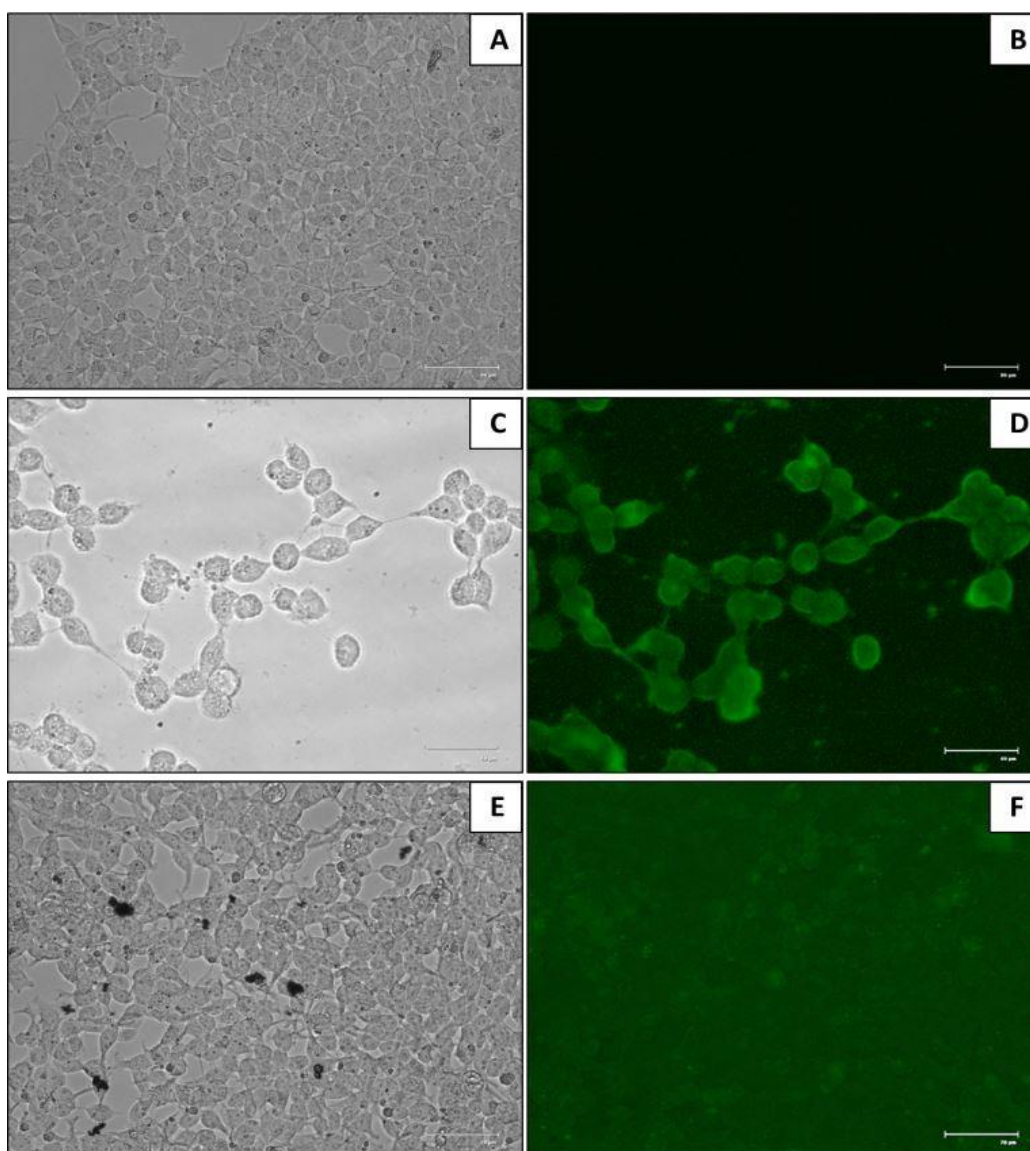


Figure 7.5: Fluorescence imaging of doxorubicin treated Hek-293 cells stained with the CuS-H2A.X probe. Images A and B shows control cells (without probe) viewed under white and green light respectively. Images C and D shows cells stained with bare nanoparticles viewed under white and green light respectively. E and F shows cells stained with the fluorescent probe viewed under white and green light respectively.

A different cell line, HeLa cells, was used to further test the fluorescent probes. Figures 7.6 and 7.7 show HeLa cells stained with PBS buffer (A, B), bare nanoparticles (C, D) and fluorescent probes (E, F). Before staining, cells were treated with CoCl_2 and doxorubicin respectively. As seen previously, no fluorescence signal was observed when cells were stained with PBS (A, B) due to the absence of a fluorophore. As such, these cells could only be viewed using white light. When bare CuS nanoparticles (C, D) were used to stain the cells, there was an increase in the fluorescence signal and cells were visible under green light. Bare CuS nanoparticles were not limited or localized to a specific area within the cells, since they are not attached to a targeting biomolecule. When the cells were stained with fluorescent probes, the fluorescence signal was reduced drastically, as observed previously with Hek-293 cells.

The low fluorescence intensity can be attributed to loss of fluorescence ability or quenching of the nanoparticles during the conjugation process. Foubert *et al.* reported that when the EDC/NHS coupling mechanism is used to attach biomolecules to nanoparticles, the quantum yield of the resulting bioconjugate is compromised due to the low pH used during this reaction [25]. Banerjee *et al.* also reported that this coupling method suffers from low conjugation efficiencies to the hydrolysis of NHS esters [26]. Alternatively, the weak fluorescence signal could be due to a low uptake of the probes by the cells. This is a result of nanoparticle aggregation after the probe has been introduced into the growth media, which results in the formation of bigger nanostructures which are not internalised by cells due to their bigger size as a result of aggregation.

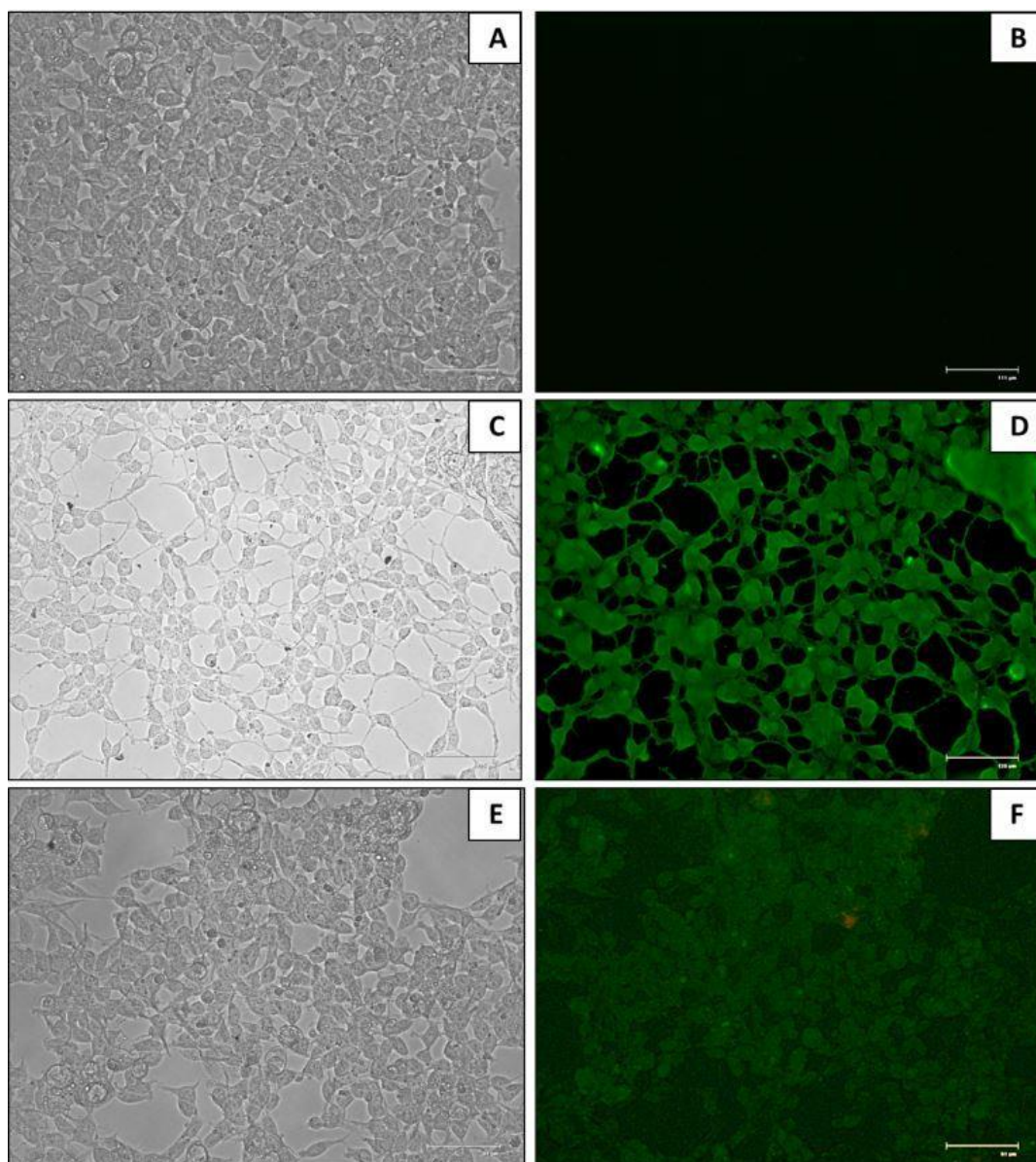


Figure 7.6: Fluorescence imaging of CoCl_2 treated HeLa cells stained with the $\text{CuS-HIF-1}\alpha$ probe. Images A and B shows control cells (without probe) viewed under white and green light respectively. Images C and D shows cells stained with bare nanoparticles viewed under white and green light respectively. E and F shows cells stained with the fluorescent probe viewed under white and green light respectively.

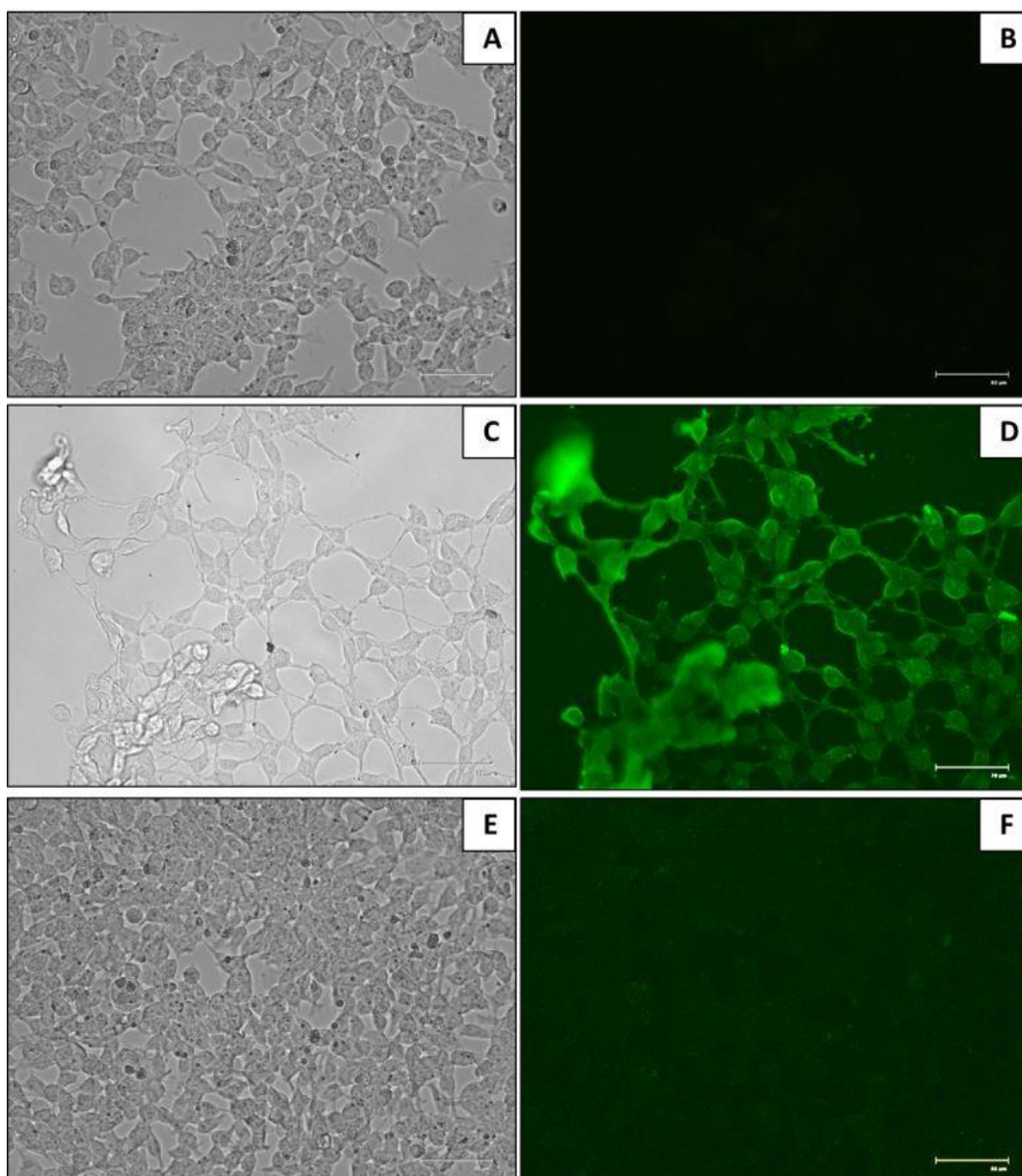


Figure 7.7: Fluorescence imaging of doxorubicin treated HeLa cells stained with the CuS-H2A.X probe. Images A and B shows control cells (without probe) viewed under white and green light respectively. Images C and D shows cells stained with bare nanoparticles viewed under white and green light respectively. E and F shows cells stained with the fluorescent probe viewed under white and green light respectively.

7.3 Conclusion

Organic dyes and other organic fluorophores have been used to image cellular processes *in vivo and in vitro*. Due to several limitations encountered with the use of these aforementioned compounds, the search for alternative fluorophores continues. Organic fluorophores have been reported to have broad emission spectra and are susceptible to photobleaching. Fluorescent semiconducting nanomaterials, due to their excellent optical properties, have been seen as suitable replacements for these fluorophores [27].

In this study, fluorescent probes were successfully synthesized by conjugating monoclonal antibodies to copper sulfide nanoparticles using the EDC/NHS coupling mechanism. These monoclonal antibodies target the HIF-1 α and phosphohistone H2A.X proteins which are produced by cells when they undergo apoptosis. Hek-293 and HeLa cells were treated with CoCl₂ and doxorubicin to induce apoptosis. The as-synthesized CuS nanoparticles proved their ability to act as fluorophores to develop fluorescent probes for imaging as these were able to fluoresce within cells, but could not accumulate at a specific site as they were not functionalised with a targeting biomolecule. However, the probes showed little efficiency as the fluorescent signal decreased when CuS nanoparticles were conjugated to monoclonal antibodies. An alternative mechanism for attaching biomolecules to as-synthesized nanoparticles needs to be explored, that will not compromise the quantum yield of the resulting fluorescent probe.

Lastly, copper and cobalt sulfide nanoparticles have been reported to have magnetic properties. Therefore, the magnetic properties of copper and cobalt sulfide nanoparticles synthesized in this study can be investigated and perhaps these nanoparticles can be used in magnetic resonance imaging.

7.4 References

- [1]. S. B. Rizvi, S. Ghaderi, M. Keshtgar, A. M. Seifalian. *Nano Reviews*, **2010**, 1, 1 – 15.
- [2]. J. Li, D. Wu, Z. Miao, Y. Zhang. *Current Pharmaceutical Biotechnology*. **2010**, 11, 662 – 671.
- [3]. T. Jamieson, R. Bakhshi, D. Petrova, R. Pocock, M. Imani, A. M. Seifalian. *Biomaterials*, **2007**, 28, 4717 – 4732.
- [4]. S. Mazumder, R. Dey, M. K. Mitra, S. Mukherjee, G. C. Das. *J. Nanomater.*, **2009**, 2009, 1 – 17.
- [5]. R. Bilan, F. Fluery, I. Nabiev, A. Sukhanova. *Bioconjugate Chem.*, **2015**, 26, 609 – 624.
- [6]. M. Hassan, B. A. Klaunberg. *Comp Med.*, **2004**, 54, 635 – 644,
- [7]. W. C. Chan, S. Nie. *Science*, **1998**, 281, 2016 – 2018.
- [8]. D. Li, Z. Y. Yan, W. Q. Cheng. *Spectrochim. Acta A.*, **2008**, 71, 1204 – 1211.
- [9]. R. Cui, H. C. Pan, J. J. Zhu, H. Y. Chen. *Anal. Chem.*, **2007**, 79, 8494 – 8501.
- [10]. M. H. Ko, S. Kim, W. J. Kang, J. H. Lee, H. Kang, S. H. Moon, D. H. Hwang, H. Y. Ko, D. S. Lee. *Small.*, **2009**, 5, 1207 – 1212.
- [11]. L. Shang, K. Nienhaus, X. Jiang, L. Yang, K. Landfester, V. Mailänder, T. Simmet, G. U. Nienhaus. *Beilstein J. Nanotechnol.*, **2014**, 5, 2388 – 2397.
- [12]. T. H. L. Nghiem, T. H. La, X. H. Vu, V. H. Chu, T. H. Nguyen, Q. H. Le, E. Fort, Q. H. Do, H. N. Tran. *Adv. Nat. Sci.: Nanosci. Nanotechnol.*, **2010**, 1, 1 – 5.
- [13]. C. W. Liu, W. J. Lin. *Int. J Nanomedicine.*, **2012**, 7, 4749 – 4767.

- [14]. G. Kroemer, L. Galluzzi, P. Vandenabeele, J. Abrams, E. S. Alnemri, E. H. Baehrecke, M. V. Blagosklonny, W. S. El-Deiry, P. Golstein, D. R. Green, M. Hengartner, R. A. Knight, S. Kumar, S. A. Lipton, W. Malorni, G. Nuñez, M. E. Peter, J. Tschopp, J. Yuan, M. Piacentini, B. Zivotovsky, G. Melino. *Cell Death Differ.*, **2009**, 16, 3 – 11.
- [15]. E. U. Kurz, P. Douglas, S. P. Lees-Miller. *THE JOURNAL OF BIOLOGICAL CHEMISTRY*, **2004**, 279, 53272– 53281.
- [16]. S. Elmore. *Toxicologic Pathology.*, **2007**, 35, 495 – 516.
- [17]. L. M. Lopez-Sanchez, C. Jimenez, A. Valverde, V. Hernandez, J. Penarando, A. Martinez, C. Lopez-Pedraza, J. R. Munoz-Castaneda, J. R. De la Haba-Rodriguez, E. Aranda, A. Rodriguez-Ariza. *PLoS ONE*. **2014**, 9, 1 – 10.
- [18]. Y. K. Bae, N. Trisnadi, S. Kadam, A. Stathopoulos. *Cell Adh Migr.*, **2012**, 6, 397 – 403.
- [19]. A. Vengellur, J. J. LaPres. *Toxicol Sci.*, **2004**, 82, 638 – 646.
- [20]. H. Z. Wang, H. Y. Wang, R. Q. Liang, K. C. Ruan. *Acta Biochim Biophys Sin.*, **2004**, 36, 681 – 686.
- [21]. D. Chilov, G. Camenisch, I. Kvietikova, U. Ziegler, M. Gassmann, R. H. Wenger. *J. Cell Sci.*, **1999**, 112, 1203 - 1212.
- [22]. G. Chachami, E. Paraskeva, J. M. Mingot, G. G. Braliou, D. Görlich, G. Simos. *Biochem. Biophys. Res. Commun.*, **2009**, 390, 235 – 240.
- [23]. S. Wang, E. A. Konorev, S. Kotamraju, J. Joseph, S. Kalivendi, B. Kalyanaraman. *J. Biol. Chem.*, **2004**, 279, 25535 – 25543.
- [24]. E. U. Kurz, P. Douglas, S. P. Lees-Miller. *J. Biol. Chem.*, **2004**, 279, 53272 – 53281.
- [25]. A. Foubert, N. V. Beloglazova, A. Rajkovic, B. Sas, A. Madder, I. Y. Goryacheva, S. De Saeger. *Trends In Analytical Chemistry*, **2016**, 83, 31 – 48.

[26]. A. Banerjee, C. Gazon, B. Nadal, T. Pons, Y. Krishnan, B. Dubertret. *Bioconjugate Chem.*, **2015**, 26, 1582 – 1589.

[27]. S. Jin, Y. Hu, Z. Gu, L. Liu, H. C. Wu. *J. Nanomater.*, **2011**, 2011, 1 – 13.

Chapter 8: General Conclusions and Recommendations

8.1 Conclusions

Semiconductor metal chalcogenides have been used across a number of disciplines due to their inherent properties. Typically, these nanomaterials are used in energy based applications, and it is until recently that they have attracted interest from biological applications. Generally, semiconductor nanomaterials are synthesized using an organometallic route which produces high quality nanostructures that are highly cytotoxic and insoluble in biological media. This limits the use of these nanomaterials in biological applications. Additional processing is therefore required to make these nanomaterials biocompatible. Unfortunately, some of the most important properties of these nanoparticles are negatively affected during this process [18,19]. This then prompted the synthesis of QDs in polar solvents which produce stable, hydrophilic, and biocompatible QDs that can be used directly in biological assays without the need for ligand exchange [20-22].

This work was based on the synthesis of water soluble nanoparticles (Cu_xS_y and Co_xS_y) that can be used directly in biological applications, for imaging purposes. Nanoparticles were successfully synthesized using copper and cobalt chloride as metal sources with sodium diethyldithiocarbamate and thioacetamide employed as sulfur sources. These were capped with four different ligands such as glutathione, thioglycolic acid, 18-crown-6 and L-carnosine, with water used as a solvent. Synthesis was conducted at two different temperatures, namely 50 and 95 °C.

In chapter 4, Cu_xS_y nanoparticles were successfully synthesized using an aqueous synthesis route. From optical studies, large blue shifts in the band gap of nanoparticles were observed compared to the bulk form, due to quantum confinement effects. Moreover, the PLs were red shifted from their corresponding absorption spectra a phenomenon that has been reported previously. Morphological studies revealed the formation of small spherical nanoparticles at lower synthesis temperatures, whereas bigger nanoparticles were formed when the synthesis temperature was increased to 95 °C, a phenomenon attributable to Ostwald ripening. Of particular interest was the synthesis of GSH capped Cu_xS_y , which resulted in the formation of small spherical nanoparticles (± 3 nm) at lower temperatures which, when synthesis was conducted at higher temperatures, evolved into hexagonal plates (± 15 nm). Structural

characterization revealed that Cu_xS_y formed multiple crystal phases, namely covellite and chalcosite phases, when SDEDTC is used at both reaction temperatures. However, when TAA was used as a sulfur source, a single phase (covellite) was formed at both low and high reaction temperatures.

In chapter 5, as-synthesized Co_xS_y nanoparticles exhibited absorption peaks and band edges that are blue shifted from their bulk form and PL peaks which are red shifted from their respective absorption spectra due to quantization effects. Small spherical nanoparticles were formed at lower temperatures, and big irregular particles were formed at higher temperatures. Multiple stoichiometries were formed at both low and high temperatures, proving the difficulty of forming a single phase of Co_xS_y nanoparticles.

During nanoparticle synthesis, temperature was seen to be the contributing factor which influenced the properties of as-synthesized nanoparticles, compared to the use of various capping ligands and sulfur sources. However, temperature is known to influence the size of nanoparticles, but not the phase or morphology, since temperature influences the growth stage rather than the nucleation stage, and therefore has no effect on initial characteristics.

From the cytotoxicity studies, Cu_xS_y revealed a concentration dependant decrease in the viability of MT-4 cells. All Cu_xS_y nanoparticles were toxic at high concentrations. However, Cu_xS_y nanoparticles were non-toxic at concentrations below 3 $\mu\text{g}/\text{ml}$, with GSH capped Cu_xS_y nanoparticles showing little signs of toxicity even at the highest concentration (50 $\mu\text{g}/\text{ml}$), hence these were chosen as nanoparticles of choice for imaging applications. Co_xS_y nanoparticles showed little signs of toxicity, with cell viability maintained above 75% even at the highest concentration tested. However, given the bigger size of as-synthesized Co_xS_y nanoparticles and also their clumping arrangement, it might be difficult for cells to internalise these nanoparticles. This can result in a small amount of nanoparticles entering the cells; hence cell viability was not adversely affected.

In chapter 7, Cu_xS_y nanoparticles were functionalised via conjugation with monoclonal antibodies against the hypoxia inducible factor and phospho-histone proteins. These proteins are produced by cells when they undergo apoptosis in response to stressful conditions. GSH capped Cu_xS_y nanoparticles were chosen as fluorophores because of their small size and spherical shape, which makes it easier for these nanoparticles to be internalized as they can

penetrate the cell membrane with ease. The success of the conjugation reaction was confirmed using Uv-vis spectroscopy which showed a red shift in the absorption spectra of nanoparticles after conjugation.

The probes were used to image apoptotic Hek-293 and HeLa cells. The fluorescence intensity of the probes was low when compared to that of bare nanoparticles. Bare nanoparticles were clearly visible within the cells when illuminated with green light. This proved the ability of nanoparticles in acting as fluorophores in the design of fluorescent probes. However, alternative methods of conjugating biomolecules to the nanoparticles for probe development should be explored.

In conclusion, water soluble copper and cobalt sulfide nanoparticles were successfully synthesized using an aqueous synthesis route, with water used as a solvent. These nanoparticles were found to be stable in biological media and not toxic *in vitro* when used within moderate concentrations. Copper sulfide nanoparticles synthesized at 50 °C using SDEDTC as a sulfur source were seen to have great potential for imaging applications.

8.2 Recommendations and Future Work

Recommendations for future work involves the formulation of a nanoparticle synthesis method that can tailor the synthesis of water soluble CuS and CoS nanoparticles with specified shapes, narrow size distributions and defined stoichiometry. This is important for nanoparticles that are intended for use in biological applications. This can be achieved by exploring the use of various capping ligands and also altering reaction parameters such as pH, temperature and concentration of reactants. A lot is yet to be achieved with respect to cytotoxicity testing of nanomaterials. A cytotoxicity testing method that can track or trace the localization of nanoparticles within cells should be formulated as the mechanism by which these nanoparticles induce damage to cells is not clearly defined. Moreover, most nanoparticles are classified as non-toxic, whereas these nanomaterials are not internalised by cells due to clumping and aggregation which produces big lumps of nanoparticles that cannot be taken up by cells, resulting in incorrect results. Further optimisation of the imaging applications will be undertaken. Parameters such as the method of conjugation, PL spectra of fluorescent probe following conjugation, the concentration of the fluorescent probe used to

stain the cells and also the duration of the staining step will be optimised further to improve assay sensitivity.